Journal of Electromagnetic Analysis and Applications

ISSN: 1942-0730 (Print), 1942-0749 (Online)

Volume 2, Number 4, April 2010

www.scirp.org/journal/jemaa

Scientific Research

JOURNAL EDITORIAL BOARD

ISSN: 1942-0730 (Print) 1942-0749 (Online)

http://www.scirp.org/journal/jemaa

Editors-in-Chief

Prof. James L. Drewniak	University of Missouri-Rolla, USA
Prof. Yuanzhang Sun	Wuhan University, China

Editorial Board

Dr. Michail B. Belonenko	Volgograd Institute of Business, Russia
Dr. Boguslaw Butrylo	Bialystok Technical University, Poland
Prof. Qingquan Chen	University of Hong Kong, China
Dr. Yuchun Guo	Xidian University, China
Dr. Xijiang Han	Harbin Institute of Technology, China
Dr. Eisuke Hanada	Shimane University Hospital, Japan
Dr. Isabel Jesus	Institute of Engineering of Porto, Portugal
Prof. Ruomei Li	Chinese Society for Electrical Engineering, China
Prof. Junyong Liu	Sichuan University, China
Prof. Kaipei Liu	Wuhan University, China
Dr. Abbas A. L. Neyestanak	Iranian Research Institute for Electrical Engineering, Iran
Dr. Ozlem Ozgun	Middle East Technical University, Turkey
Prof. M. Ramamoorty	University of British Columbia, Canada
Dr. Jiangjun Ruan	Wuhan University, China
Dr. Mazen A. E. Salam	Assiut University, Egypt
Dr. Yinbiao Shu	State Grid Corporation, China
Prof. Yonghua Song	Tsinghua University, China
Prof. Francisco Torrens	Universitat of Valencia, Spain
Prof. Felix Wu	University of Hong Kong, China
Prof. Ryuichi Yokoyama	Waseda University, Japan
Dr. Ben Young	University of Hong Kong, China
Dr. Wenhua Yu	Pennsylvania State University, USA
Dr. Jun Zou	Zhejiang University, China

Editorial Assistants

Zhenhua Sun	Jemaa@scirp. org
Dao-Chun Huang	Wuhan University, China

J. Electromagnetic Analysis & Applications, **2010, 2, 195-281**
Published Online April 2010 in SciRes (http://www.SciRP.org/journal/jemaa/).

TABLE OF CONTENTS

Volume 2 Number 4 April 2010

Copyright © 2010 SciRes.

Journal of Electromagnetic Analysis and Applications (JEMAA)

Journal Information

SUBSCRIPTIONS

The *Journal of Electromagnetic Analysis and Applications* (Online at Scientific Research Publishing, www.SciRP.org) is published monthly by Scientific Research Publishing, Inc., USA.

Subscription rates:

Print: $50 per issue.
To subscribe, please contact Journals Subscriptions Department, E-mail: sub@scirp.org

SERVICES

Advertisements
Advertisement Sales Department, E-mail: service@scirp.org

Reprints (minimum quantity 100 copies)
Reprints Co-ordinator, Scientific Research Publishing, Inc., USA.
E-mail: sub@scirp.org

COPYRIGHT

Copyright©2010 Scientific Research Publishing, Inc.

All Rights Reserved. No part of this publication may be reproduced, stored in a retrieval system, or transmitted, in any form or by any means, electronic, mechanical, photocopying, recording, scanning or otherwise, except as described below, without the permission in writing of the Publisher.

Copying of articles is not permitted except for personal and internal use, to the extent permitted by national copyright law, or under the terms of a license issued by the national Reproduction Rights Organization.

Requests for permission for other kinds of copying, such as copying for general distribution, for advertising or promotional purposes, for creating new collective works or for resale, and other enquiries should be addressed to the Publisher.

Statements and opinions expressed in the articles and communications are those of the individual contributors and not the statements and opinion of Scientific Research Publishing, Inc. We assumes no responsibility or liability for any damage or injury to persons or property arising out of the use of any materials, instructions, methods or ideas contained herein. We expressly disclaim any implied warranties of merchantability or fitness for a particular purpose. If expert assistance is required, the services of a competent professional person should be sought.

PRODUCTION INFORMATION

For manuscripts that have been accepted for publication, please contact:
E-mail: jemaa@scirp.org

J. Electromagnetic Analysis & Applications, 2010, 2: 195-204
doi:10.4236/jemaa.2010.24028 Published Online April 2010 (http://www.SciRP.org/journal/jemaa)

Scientific Research

Radiation Characteristics of Antennas on the Reactive Impedance Surface of a Circular Cylinder Providing Reduced Coupling

Jean-François D. Essiben[1], Eric R. Hedin[2], Yong S. Joe[2]

[1]Department of Electrical Engineering, University of Douala (Ecole Normale Supérieure d`Enseignement Technique) Douala, Cameroon; [2]Center for Computational Nanosciences, Department of Physics and Astronomy, Ball State University, Muncie, USA.
Email: jessibencm@yahoo.fr, erhedin@bsu.edu, ysjoe@bsu.edu

Received December 16th, 2009; revised January 18th, 2010; accepted January 22nd, 2010.

ABSTRACT

The radiation characteristics of waveguide antennas located on the surface of a circular cylinder are investigated theoretically and numerically. A reactive impedance structure is used to provide reduced coupling between two antennas on the surface of a cylinder. Using the moment method, a solution to the problem of the radiation of a single and two parallel-plate waveguides located on the surface of a reactive impedance cylinder is derived. The influence of the reactive impedance structure on the coefficient of standing waves, the radiation patterns, and the decoupling between antennas is studied.

Keywords: *Decoupling, Radiation, Reactive Impedance Structure*

1. Introduction

In radio engineering, a group of near-omnidirectional antenna radiators having a common flange, such as an open end of the waveguide (or aperture), are widely used. In practice it is often required to limit the coupling between the receiving and transmitting antennas located on the same surface at a small distance from each other.

The known methods of decreasing interaction between antennas utilize the alteration of amplitude and phase distribution on some surfaces. Among accepted measures to decrease coupling between antennas are mutual shielding of antennas and deposition of additional screens (or shields) across the line of connection. In the case with near-omnidirectional antennas, two groups of additional measures are applied: radio-absorbing materials and surface decoupling devices.

As the review of a number of articles [1-8] shows, the most widespread and successful way of solving the problem of coupling antenna devices is the use of reactive impedance structures, specifically corrugated structures. The most widespread type of decoupling structure is a metallic structure with a rectangular cut of corrugations. It has been shown that the value of decoupling generally depends on electrical and geometrical parameters of the reactive impedance structures [9-12]. However, solving the problem of optimum placement of the decoupling device using this approach is impossible [9]. In [9,11], the authors used corrugated structures with different depths of corrugations. The waveguide antennas discussed in [9] are on the surface of a cylinder, and in [11] they are located on a plane. For each case, it has been shown that the coupling coefficient was reduced in the presence of a corrugated structure. The planar structure, however, more seriously influences the radiation pattern of the antenna which is near to the structure. [10] reviews different structures for reducing the coupling between antennas. Through the method of integral equations it is shown that the decoupling properties of the structure are determined only by the structure's length and in fact do not depend on the periodicity of the structure. In addition, it is shown that the weakening of coupling between antennas in a wide range of frequencies can be obtained to a larger extent on convex surfaces than on flat ones [10]. The change of the coupling value is sufficiently influenced by areas located near the antennas and by the degree of the decoupling, which is defined by the maximum rate of change of surface reactive impedance [11]. The authors of [12] consider engineering techniques of evaluating reduced coupling between near-omnidirectional slot antennas located on the surface

Copyright © 2010 SciRes.

of a model object, which consists of a circular cylinder and a rectangular plate. The calculations showed an effective means of obtaining the required reduction in spatial coupling is the correct choice of mutual placement and orientation of the antennas, which should be taken into account when designing the system.

This paper explores in detail the problem of mutual coupling between two antennas located on the surface of a circular cylinder separated by a corrugated structure with constant depth of corrugation. We will present a strict solution to the problem of the analysis of the radiation characteristics of a single antenna in the shape of the open end of a parallel-plate waveguide. Unique to our work is that we solve the problem in the presence of a second waveguide antenna. First, we study the radiation pattern and the dependence of the coefficients of standing waves on the value of the constant reactive impedance of a single waveguide located on the surface of a circular cylinder. We also present the decoupling coefficient in the presence and in the absence of the reactive surface impedance. These are novel contributions of this study. Second, we consider reduced coupling between two waveguide antennas where the presence of two antennas leads to distortion of their radiation patterns. In this system, we show that the presence of capacitive impedance almost completely eliminates distortions in their radiation patterns made by the receiving antenna. Hence, the radiation pattern of both antennas coincides with that of a single antenna with a reactive impedance flange. The presentation of radiation patterns for single and double antennas with and without impedance flanges for the cylindrical configuration with a corrugated decoupling structure is original to our work. We show that the presence of capacitive impedance nearly eliminates distortions caused by the proximity of the receiving antenna. While independent verification of the validity of our specific numerical results is not available, as this is original work, references cited earlier show similar results for similar waveguide systems which support our conclusions.

The paper is organized as follows: In Section 2, a solution to the problem of the radiation of a parallel-plate waveguide located on the surface of a reactive impedance cylinder is derived. Next, Section 3 considers a solution to the problem of the reduction in coupling between two waveguide antennas located on the surface of a reactive impedance cylinder and presents the formula of some key parameters of antennas. In Section 4, the numerical results for the decoupling coefficients and radiation patterns for both single and double waveguide antennas on the surface of a circular cylinder are presented. Finally, Section 5 is devoted to conclusions.

2. Radiation of a Cylindrical Waveguide

2.1 Statement of the Problem

First of all, we try to find a solution to the two- dimensional problem of electromagnetic field (EMF) radiation from the open end of a parallel-plate waveguide located on the surface of a reactive impedance cylinder ($r=R$) shown in **Figure 1**. The waveguide has width, a, and spans between angles φ_1 and φ_2 on the curved surface of the conductor. We will calculate the EMF as a function of radius, r, and azimuthal angle, φ. To solve for the EMF in the waveguide, its aperture, and in the free space outside of the cylindrical surface, we assume a certain excitation wave within the waveguide, and impedance boundary conditions on the surface of the cylinder between the openings of the transmitting and receiving waveguides. Then we make use of the Lorentz lemma and assume subsidiary field sources in each space. We then obtain integral correlations for the fields in each space. A system of integral equations results, which can be transformed into a system of linear algebraic equations that are solved for the field components by advanced numerical techniques, as explained in detail below.

Let the parallel-plate waveguide be excited by a wave characterized by $\vec{\mathbf{E}}^{\mathbf{i}}$ and $\vec{\mathbf{H}}^{\mathbf{i}}$:

$$H_z^i = H_0 e^{-ikr} \text{ and } E_\varphi^i = W H_0 e^{-ikr} \quad (r \le R) \qquad (1)$$

where $W = 120\pi\ \Omega$ is the characteristic resistance of free space, H_o is the amplitude of the incident wave,

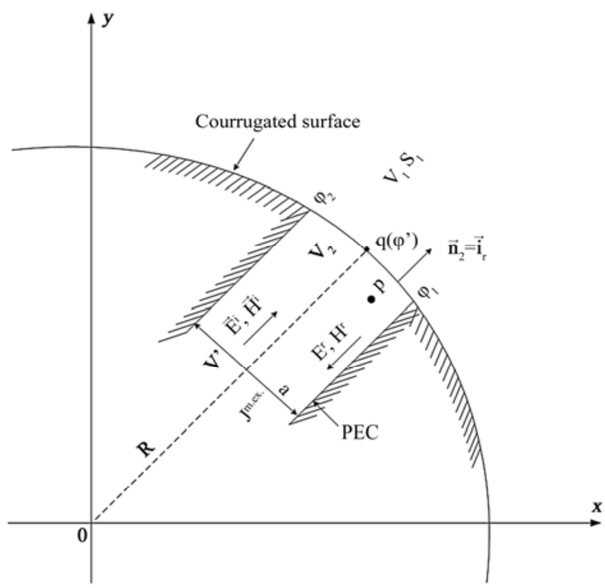

Figure 1. The open end of a single waveguide antenna located on the surface of a circular cylinder

and R is the radius of the cylinder. On the surface S_1 $\left(\varphi \in [0,\varphi_1]\,\&\,[\varphi_2, 2\pi]\right)$ the following reactive impedance boundary conditions are fulfilled:

$$\vec{\mathbf{n}} \times \vec{\mathbf{E}} = -Z\,\vec{\mathbf{n}} \times (\vec{\mathbf{n}} \times \vec{\mathbf{H}}) \text{ and } E_\varphi = -ZH_z \qquad (2)$$

where $\vec{\mathbf{n}} = \vec{\mathbf{i}}_r$ is the unit normal to the surface of the cylinder ($r = R$), Z is the surface reactive impedance, and $\vec{\mathbf{E}}$ and $\vec{\mathbf{H}}$ are the electric and magnetic fields, respectively.

Next, we determine the EMF in the regions both outside of the cylinder (space V_1) and inside the radiating waveguide (space V_2). Then, we calculate the coefficient of standing waves (CSW) of the transmitting antenna and the radiation pattern of such an antenna (see Section 3).

2.2 Solution of the Problem

In order to solve for the EMF's, it is necessary to use the Lorentz lemma in integral form [13], where constant pre-factors are omitted:

$$\begin{aligned}&\int_S \left\{(\vec{\mathbf{E}} \times \vec{\mathbf{H}}^s) - (\vec{\mathbf{E}}^s \times \vec{\mathbf{H}})\right\} \bullet \vec{\mathbf{n}}\,dS \\ &= \int_V \left(\vec{\mathbf{J}}^{m.s.} \vec{\mathbf{H}} - \vec{\mathbf{J}}^{e.s.} \vec{\mathbf{E}}\right) dV + \int_{V'} \left(\vec{\mathbf{J}}^{e.ex.} \vec{\mathbf{E}}^s - \vec{\mathbf{J}}^{m.ex.} \vec{\mathbf{H}}^s\right) dV,\end{aligned} \qquad (3)$$

where $\mathbf{E}^s$ and $\mathbf{H}^s$ are vectors of the intensity of the electric and magnetic fields of subsidiary sources in volumes; $\vec{\mathbf{J}}^{e.s.}$ and $\vec{\mathbf{J}}^{m.s.}$ are complex amplitudes of current densities of the subsidiary electric and magnetic sources in volumes; $\vec{\mathbf{J}}^{m.ex.}$ and $\vec{\mathbf{J}}^{e.ex.}$ are amplitudes of linear current densities of adjacent source threads. In accordance with the stated polarization of the radiated field, Equation (2), as subsidiary sources in spaces V_1 and V_2, we choose a current thread in phase with the magnetic current parallel to the z-axis:

$$\vec{\mathbf{j}}^{\text{e.ex.}} = 0 \text{ and } \vec{\mathbf{j}}^{\text{m.ex.}} = \vec{\mathbf{i}}_{\mathbf{z}} I_0^{\text{m}} \delta(p,q) \qquad (4)$$

where $\delta(p,q)$ is a two-dimensional delta-function, p is the point of observation, q is the point of integration, and I_0^m is the current amplitude. To simplify the solution of the problem in the integral correlation, we impose boundary conditions on the subsidiary fields which arise from the subsidiary sources:

$$E_\varphi^m(p,q)_{r=R} = 0 \qquad (5)$$

This standard boundary condition states that the tangential component of the subsidiary electric field on the curved cylindrical surface is zero.

2.3 Integral Correlations for Space V_1

We now consider integral correlations for each of the spaces shown in **Figure 1**. By placing a subsidiary source at the point $p(r \ge R,\ \varphi)$ and taking into account boundary conditions in the Lorentz lemma of Equation (3), we obtain

$$H_{z1}(\varphi) = -\int_0^{2\pi} E_{\varphi 1}(\varphi') H_{z1}^m(\varphi,\varphi')\,R\,d\varphi' \qquad (6)$$

where $H_{z1}^m(\varphi,\varphi') = \dfrac{i}{2\pi RW} \sum_{n=-\infty}^{\infty} \dfrac{H_n^{(2)}(kR)}{H_n^{(2)'}(kR)} e^{in(\varphi-\varphi')}$ is the subsidiary magnetic field on the surface of an ideal conducting cylinder. Here, i is the imaginary operator, $H_n^{(2)}$ is the n^{th}-order Hankel function of the second kind, and $H_n^{(2)'}$ is its derivative. In Equation (6), there are two unknown values: $E_{\varphi 1}$ and H_{z1} are the fields of the threads of the electric and magnetic currents in free space, respectively. In order to eventually solve for them, two more equations are required. These come from the Lorentz lemma in the space V_2 and the subsequent coupling between the waveguides (Section 3).

2.4 Lorentz Lemma for Space V_2

The subsidiary magnetic field in the space V_2 that is produced on an aperture of a cylindrical waveguide is obtained from the Lorentz lemma of Equation (3). By imposing boundary conditions on the tangential component of the subsidiary electric field vector at the walls of the parallel-plate waveguide and on its aperture $\left(\vec{\mathbf{n}} \times \vec{\mathbf{E}}_2^m = 0\right)$, we obtain an integral correlation for the EMF inside the waveguide V_2:

$$\begin{aligned}H_{z2}(\varphi) = 2H_z^i(\varphi) &+ \int_{A_1} E_{\varphi 2}(\varphi') H_{z2}^{\text{m}}(\varphi,\varphi') R d\varphi' \\ &+ \int_{A_1} E_{\varphi 2}^{\text{i}}(\varphi') H_{z2}^{\text{m}}(\varphi,\varphi') R d\varphi'.\end{aligned} \qquad (7)$$

The field in the aperture of the waveguide is then written as the following correlation:

$$H_{z2}(\varphi) = 2H_0 + \int_{\varphi 1}^{\varphi 2} E_{\varphi 2}(\varphi') H_{z2}^{\text{m}}(\varphi,\varphi') R d\varphi' \qquad (8)$$

where the field of the subsidiary source can be written as

$$H_{z2}^m(\varphi,\varphi') = \frac{i}{2\pi RW} \sum_{n=-\infty}^{\infty} \frac{H_n^{(2)}(kR)}{H_n^{(2)'}(kR)} e^{in(\varphi-\varphi')} \qquad (9)$$

3. Reduced Coupling of Two Cylindrical Waveguides

Let us now consider the problem of reducing the coupling between two parallel-plate waveguide antennas

Copyright © 2010 SciRes.

located on the surface of the reactive impedance cylinder. In **Figure 2**, we show two aperture antennas with opening sizes of a and b which are located on the surface of a reactive impedance cylinder ($r = R$). These two antennas (transmitting and receiving ones), which have the shape of the open end of parallel-plate waveguides, are separated by distance L from each other $\left(L = R(\varphi_3 - \varphi_2)\right)$. The boundary conditions, stated in Equation (2), exist on the surface S_1 ($\varphi \in [\varphi_2, \varphi_3]$ and $[\varphi_4, \varphi_1]$) which separates two antennas. Because another waveguide with an opening of size b is added, one more equation (relative to the field in the opening of the receiving waveguide) is included in the system of integral equations. In addition, we need to determine the field in the receiving waveguide (space V_3), the radiation patterns, and the decoupling coefficient.

3.1 Integral Correlations for Space V_3

To solve this problem, we use the same integral form of the Lorentz lemma. In this space, V_3, the lemma is different from Equation (8) only in the absence of additional sources and by the size of the opening of V_3:

$$H_{z3}(\varphi) = \int_{a+L}^{a+L+b} E_{\varphi 3}(\varphi') H_{z3}^{m}(\varphi, \varphi') R d\varphi' \qquad (10)$$

where $H_{z3}^{m}(\varphi, \varphi')$ is the subsidiary magnetic field in the space V_3.

3.2 System of Integral Equations

By taking into account the boundary conditions of Equation

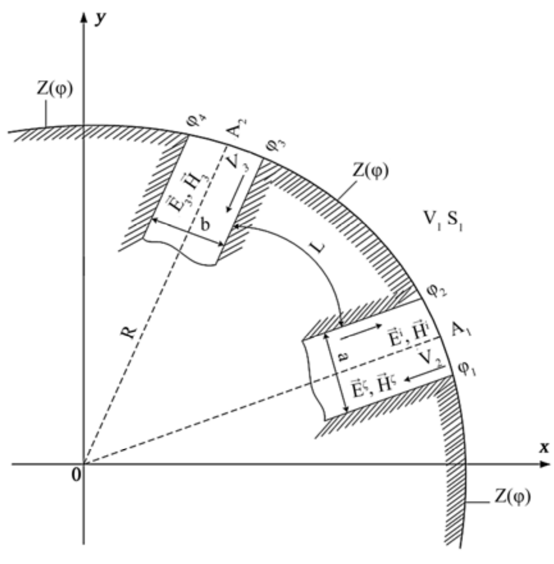

Figure 2. Geometry of the structure with two parallel-plate waveguide antennas located on the surface of the reactive impedance cylinder

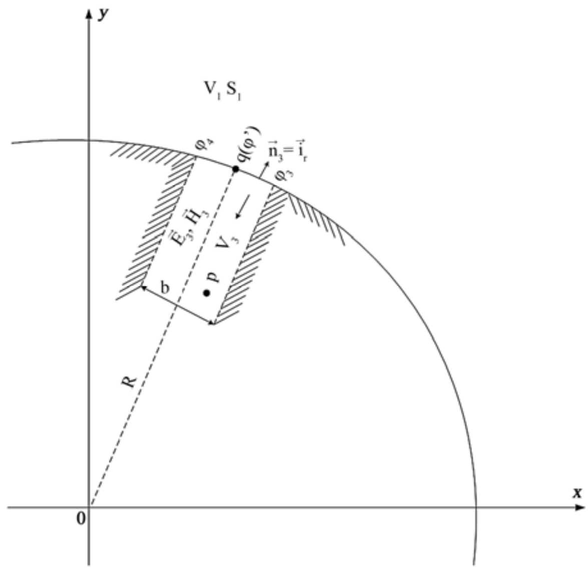

Figure 3. The open end of a waveguide located on the surface of a circular cylinder for space V_3

(2) on the surface of the reactive impedance flange and the equality of the tangential components of the EMF in the openings of the waveguides ($H_{z1} = H_{z2}$, $E_{\varphi 1} = E_{\varphi 2}$ when $p \in [\varphi_1, \varphi_2]$ and $H_{z1} = H_{z3}$, $E_{\varphi 1} = E_{\varphi 3}$ when $p \in [\varphi_3, \varphi_4]$), we obtain a system of integral equations relative to the unknown tangential component of the electric field $E_{\varphi}(\varphi)$ on the surface of the cylinder $(r = R)$ (see **Figure 3**):

$$\begin{cases} \int_{\varphi_1}^{\varphi_2} E_{\varphi}(\varphi')[H_{z1}^{m}(\varphi,\varphi') + H_{z2}^{m}(\varphi,\varphi')]Rd\varphi' \\ + \int_{\varphi_2}^{\varphi_1+2\pi} E_{\varphi}(\varphi') H_{z1}^{m}(\varphi,\varphi') R d\varphi' = -2H_0 \qquad \varphi \in [\varphi_1, \varphi_2] \\ E_{\varphi}(\varphi) - Z(\varphi)\int_{0}^{2\pi} E_{\varphi}(\varphi') H_{z1}^{m}(\varphi,\varphi') R d\varphi' = 0 \\ \varphi \in [\varphi_2, \varphi_3] \,\&\, [\varphi_4, \varphi_1 + 2\pi] \\ \int_{\varphi_3}^{\varphi_4} E_{\varphi}(\varphi')[H_{z1}^{m}(\varphi,\varphi') + H_{z2}^{m}(\varphi,\varphi')]Rd\varphi' \\ + \int_{\varphi_4}^{\varphi_3+2\pi} E_{\varphi}(\varphi') H_{z1}^{m}(\varphi,\varphi') R d\varphi' = 0 \qquad \varphi \in [\varphi_3, \varphi_4], \end{cases} \qquad (11)$$

where the subsidiary magnetic fields $H_{z1}^{m}(\varphi,\varphi')$, $H_{z2}^{m}(\varphi,\varphi')$ and $H_{z3}^{m}(\varphi,\varphi')$ are solutions to the non-uniform Helmholtz equations for the complex amplitudes of the field vectors for regions V_1, V_2, and V_3, respectively.

In calculating the subsidiary fields in the spaces V_2 and V_3, it is assumed that they have a rectangular shape, short-circuited in the openings of the ideally flat conducting wall. The apertures of the antennas coincide with

Copyright © 2010 SciRes.

these walls. In this case, the subsidiary fields in Equation (11) are defined by the following correlations:

$$H_{z2}^{\mathrm{m}}(\varphi,\varphi') = -\frac{k}{Wa}\sum_{n=0}^{\infty}\frac{\varepsilon_n}{k2_n}\cos\gamma_n(\varphi_1-\varphi)\cos\gamma_n(\varphi'-\varphi_1)$$

$$H_{z3}^{\mathrm{m}}(\varphi,\varphi') = -\frac{k}{Wb}\sum_{n=0}^{\infty}\frac{\varepsilon_n}{k3_n}\cos\zeta_n(\varphi_3-\varphi)\cos\zeta_n(\varphi'-\varphi_3), \quad (12)$$

where $\gamma_n = \frac{n\pi}{a}R$, $\zeta_n = \frac{n\pi}{b}R$, $k = 2\pi/\lambda$ is the wave number, and λ is the wavelength. Also, $k2_n = -i\sqrt{\left(\frac{n\pi}{a}\right)^2 - k^2}$, $k3_n = -i\sqrt{\left(\frac{n\pi}{b}\right)^2 - k^2}$, and the dielectric permittivity of the n^{th} layer is given by $\varepsilon_n = \begin{cases} 1 & n=0 \\ 2 & n>0 \end{cases}$.

The required solution has a specific feature at the edges of the structure $(\varphi = \varphi_1, \varphi_2, \varphi_3,$ and $\varphi_4)$. It is taken into account by inserting a new unknown weighting parameter, $Y(\varphi)$, which has the same specific feature as the function required in the system of integral equations in Equation (11):

$$E_{\varphi}(\varphi) = Y(\varphi)\, f^{\langle s\rangle}(\varphi) \quad (13)$$

where

$$f^{\langle s\rangle}(\varphi) = \begin{cases} s=1 & ((\varphi-\varphi_1)(\varphi_2-\varphi))^{-\alpha} & \varphi\in[\varphi_1,\varphi_2] \\ s=2 & ((\varphi-\varphi_2)(\varphi_3-\varphi))^{-\xi} & \varphi\in[\varphi_2,\varphi_3] \\ s=3 & ((\varphi-\varphi_3)(\varphi_4-\varphi))^{-\alpha} & \varphi\in[\varphi_3,\varphi_4] \\ s=4 & ((\varphi-\varphi_4)(\varphi_1+2\pi-\varphi))^{-\xi} & \varphi\in[\varphi_4,\varphi_1+2\pi] \end{cases} \quad (14)$$

By solving the integral equations using the Krylov-Bogolyubov method [14] and calculating the coefficients of the matrix in a system of linear algebraic equations, the subsidiary field given in Equation (9) can be rewritten as (see Appendix A)

$$H_{z2}^{m}(\varphi,\varphi') = \frac{i}{2\pi RW}\sum_{n=-\infty}^{\infty}\left[\frac{H_n^{(2)}(kR)}{H_n^{(2)'}(kR)} - i\pi kRJ_n(kR)H_n^{(2)}(kR)\right]e^{in(\varphi-\varphi')} - \frac{k}{2W}H_0^{(2)}\left[2kR\left|\sin\left(\frac{\varphi-\varphi'}{2}\right)\right|\right], \quad (15)$$

where we take into account the decomposition of the Hankel function into the Bessel series (addition theorem of cylindrical functions). Here, J_n is the Bessel function of order n and $H_0^{(2)}$ is the second kind of the zero-order Hankel function. Therefore, the fields in the opening of antennas and on the reactive impedance part of the flange are found. In the following section, formulas for key parameters of the antennas are given in terms integral correlations involving the field components which have all been obtained.

3.3 Key Parameters of Antennas

The expressions for the coefficient of standing waves in the transmitting antenna, the EMF power directed into the receiving antenna, and the coefficient of coupling K_{c} between antennas are defined by the same correlations as in [15] with only a substitution of the components of the Cartesian coordinate system for those of the cylindrical coordinate system.

- The *amplitude of the reflected wave* of main type H_0^r in the active waveguide V_2 is defined by the following correlation:

$$H_0^r = H_0 - \frac{1}{Wa}\int_{\varphi_1}^{\varphi_2} E_{\varphi 2}(\varphi')Rd\varphi' \quad (16)$$

- The expression for the *coefficient of standing waves* is

$$CSW = \frac{|R|+1}{1-|R|} \quad (17)$$

where $R = 1 - \frac{1}{WH_0 a}\int_{\varphi_1}^{\varphi_2} E_{\varphi 2}(\varphi')Rd\varphi'$ is the coefficient of reflection.

- The *power of the field* acquired by the antenna V_3 is

$$P_{\mathrm{rec}} = \frac{1}{2Wb}\left|\int_{\varphi_3}^{\varphi_4} E_{\varphi 3}(\varphi')Rd\varphi'\right|^2 \quad (18)$$

- The *coefficient of coupling* between antennas is defined by

$$K_c == \frac{1}{W^2 ab}\left|\frac{R}{H_0}\int_{\varphi_3}^{\varphi_4} E_{\varphi 3}(\varphi')d\varphi'\right|^2. \quad (19)$$

The decoupling coefficient K, which is the inverse value of K_c, is defined as $K = -10\log(K_c)$.

- The *radiation pattern of antenna* A_1 can be found from the integral correlation of Equation (6), where $E_{\varphi 1}$ is already obtained from the solution of SLAE in Equation (A-1). In this process, it is required to move the point of observation P to infinity and to use the asymptote of the Hankel function with a significant

Copyright © 2010 SciRes.

argument [$H_n^{(2)}(kr) \approx i^n H_0^{(2)}(kr)$]. As a result, we obtain

$$H_{z1}(p) = H_0^{(2)}(kr) F(\varphi),\ kr \Rightarrow \infty \quad (20)$$

where $F(\varphi) = \sum_{n=-\infty}^{\infty} F_n e^{in\varphi}$ is the radiation pattern of antenna A_1, and

$F_n = \frac{i^{n-1}}{H_n^{(2)'}(kR)} \frac{1}{2\pi W} \int_0^{2\pi} E_{\varphi 1}(\varphi') e^{-in\varphi'} d\varphi'$ are the coefficients of the decomposition of the radiation pattern into a complex Fourier series. We notice here that the radiation patterns of both antennas can be calculated at once in the mode of reception by solving the problem of cylinder excitation by a flat wave.

4. Numerical Results and Discussion

4.1 Radiation of a Single Parallel-Plate Waveguide

The surface impedance $(Z = R + iX)$ has an inductive character when $X > 0$ and a capacitive character when $X < 0$. For the systems of interest, the reactive impedance is purely reactive $(Z = iX)$. **Figure 4** shows the dependences of the CSW on the value of the constant reactive impedance $Z = iX$ of the waveguide located on the surface of a circular cylinder with radius $R = 2.387\lambda$ $(kR = 15)$. The sizes of the openings of waveguides are (a) $a = 1.2\lambda$ and (b) $a = 0.2\lambda$, respectively. When the size of opening decreases, the magnitude of CSW increases by a factor of 4.5 (from **Figure 4(b)** to **Figure 4(a)**). The least value of CSW for all sizes of antennas on cylinders is found with purely reactive impedance of inductive character $(\mathrm{Im}(Z) = 1.4)$. We notice that use of the reactive impedance distribution on the surface of a cylinder (on a curved flange) leads to a significant increase of CSW. Furthermore, in the case of a cylinder with all circumstances equal, the influence of reactive impedance turns out to be less than in the plane case.

We present the radiation pattern of a single waveguide antenna on a circular cylinder of radius $R = 2.387\lambda$ with ideal conducting flange (Z=0: dotted line) and capacitive flange ($Z = -10\,i$: solid line) in **Figure 5**. The size of the aperture is $a = 0.4\lambda$ ($\varphi_1 = 20°$ and $\varphi_2 = 30°$). The dash-dotted line shows the impact of the reactive impedance part of the flange on the radiation pattern. As we can see, the capacitive impedance really distorts (or wrings out) the wave, increasing the directivity of the antenna. The dashed line represents the geome-

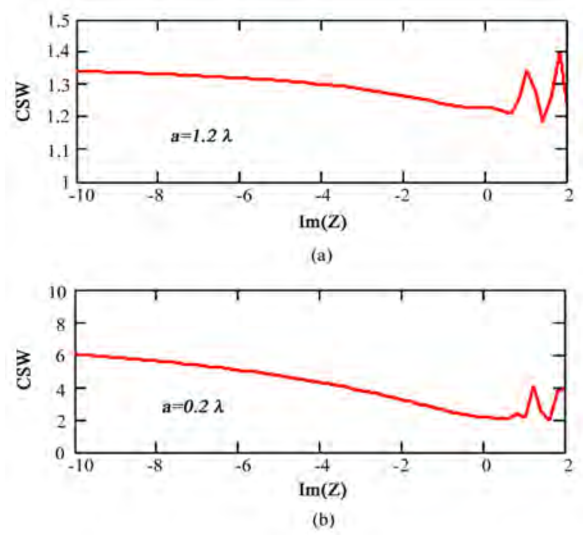

Figure 4. (Color online) The CSW as a function of the constant reactive impedance $\mathrm{Im}(Z)$ of the waveguide located on the surface of a circular cylinder with radius $R = 2.387\lambda$ $(kR = 15)$ for (a) $a = 1.2\lambda$ and (b) $a = 0.2\lambda$. An increase in the size of opening leads to a decrease of CSW.

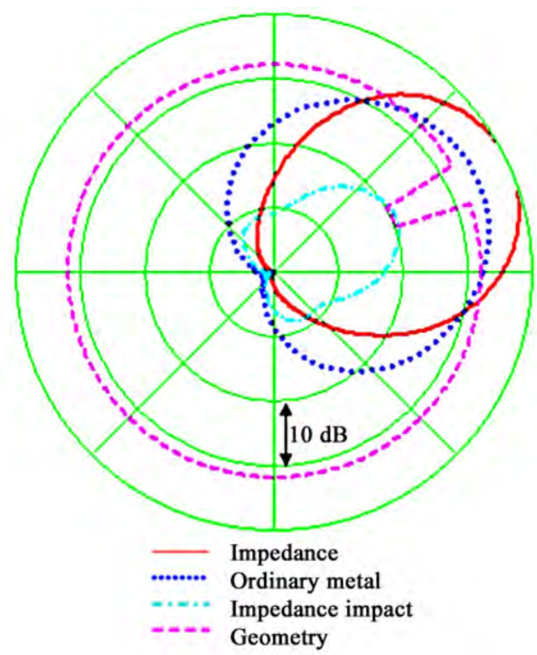

Figure 5. (Color online) Radiation pattern of a single waveguide antenna on a circular cylinder $R = 2.387\lambda$ with an ideal conducting flange ($Z = 0$: dotted line) and capacitive flange ($Z = -10i$: solid line), where the size of the aperture is equal to $a = 0.4\lambda$ ($\varphi_1 = 20°$ and $\varphi_2 = 30°$). The dash-dotted line shows the impact of the reactive impedance part of the flange on the radiation pattern. The dashed line represents the geometry of the problem

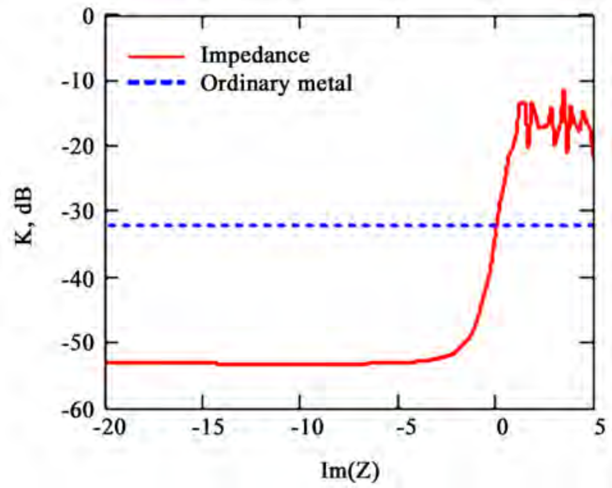

Figure 6. (Color online) Decoupling coefficient K as a function of reactivity, $Z = iX$ (solid line) with parameters $a = 0.8\lambda$, $b = 0.4\lambda$, $L = \lambda$, and $kR = 15$. The dashed line corresponds to the decoupling of the antennas on the surface of an ideal conducting cylinder

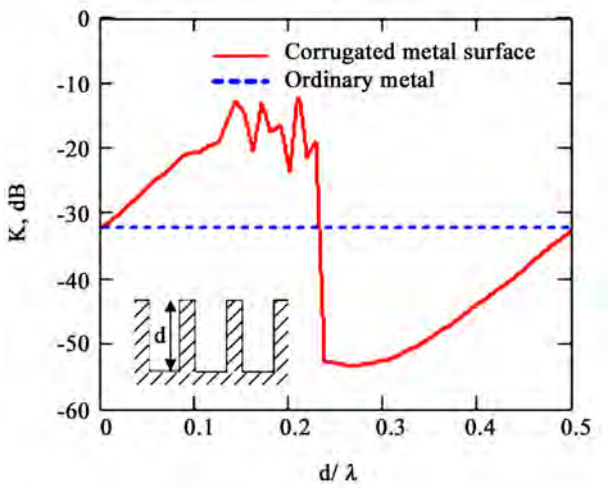

Figure 7. (Color online) Decoupling coefficient K versus the normalized depth d/λ for a corrugated structure in vacuum (solid line). The dotted line corresponds to the decoupling of antennas on the surface of an ideal conducting cylinder

try of the problem (location and relative sizes of the opening of the radiating antenna).

4.2 Radiation of Two Waveguide Antennas

Now, we study the decoupling coefficients and radiation patterns in the two waveguide antennas on the surface of a circular cylinder. **Figure 6** shows the dependence of the decoupling coefficient K on the value of the reactivity of the normalized reactive impedance of the cylindrical flange $Z = iX$ (solid line) with parameters $a = 0.8\lambda$ $b = 0.4\lambda$, $L = \lambda$, and $kR = 15$. The dashed line corresponds to the decoupling of antennas on the surface of an ideal conducting cylinder. Numerical studies show that the behavior of the decoupling coefficient for the cylindrical construction is almost the same as the plane case (see **Figure 8** in [15]). The only exception is that for the cylindrical medium the decoupling of the antennas is higher by 10 dB because of additional screening by the convex surface. In addition, the maximum value ($-52\,dB$) of the decoupling level is reached with a large value of capacitive impedance ($X \le -5$).

In order to examine the variation of the decoupling level, we consider a corrugated structure in vacuum with a constant depth of corrugation d on the cylindrical surface shown in the inset of **Figure 7**. The decoupling coefficient K as a function of the normalized depth d/λ in this structure is plotted in **Figure 7** as a solid line. The maximum level of decoupling ($K \approx -52\,dB$ when $d/\lambda \approx 0.25$) is increased by 10 dB more in comparison with the plane case [15]. The reason is that with the cylindrical surface, increasing the distance between the antennas also increases the screening by means of a surface shadowing. The constant decoupling level K for an ideal conducting cylindrical surface is shown as a dotted line.

Next, we investigate a modulation of the separation between two antennas on the surface of a circular cylinder in order to see how the decoupling level of antennas changes. In **Figure 8**, we show the dependence of the decoupling coefficient K on the surface reactive impedance $\mathrm{Im}(Z)$ for the same antennas as in **Figures 6** and **7** ($a = 0.8\lambda$, $b = 0.4\lambda$, and $kR = 15$), but located at the two different distances of (a) $L = \pi\lambda$ and (b) $L = \pi R$. When the distance between two antennas is $\pi\lambda$, which corresponds to an angular distance of $75°$ between the centers of their openings, constant reactance causes an additional increase of the decoupling up to −84 dB (solid line) in **Figure 8(a)**. The decoupling of antennas on the surface of an ideal conducting cylinder (dotted line) is also large (K= –46 dB) in comparison with the plane case. It is evident from **Figure 8(b)** that the maximum decoupling corresponds with a diametrical arrangement of antennas at $L = \pi R$ (*i.e.*, the angle between the centers of their openings is approximately equal to 180^o). It is noteworthy to mention that independent of the location of antennas, negative reactance leads to an increase of decoupling. In addition, the greater the distance between antennas, the higher the decoupling level. As for the cylinder, due to the finite nature of this distance (diametrically placed antennas are located at the maximum distance), the decoupling level is always limited.

Copyright © 2010 SciRes.

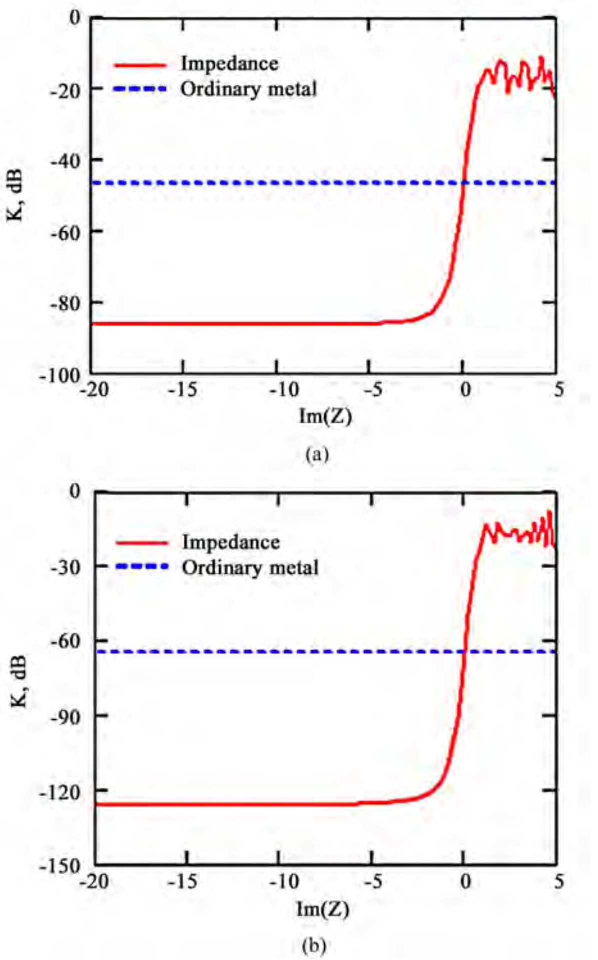

Figure 8. (Color online) (a) Decoupling coefficient K as a function of the surface reactive impedance $\mathrm{Im}(Z)$ for the same antennas as in Figures 6 and 7, but located at the two different distances of (a) $L=\pi\lambda$ (an angular distance of $75°$ between the centers of their openings) and (b) $L=\pi R$ (the angle between the centers of their openings is approximately equal to $180°$). The decoupling of antennas on the surface of an ideal conducting cylinder is shown as a dotted line

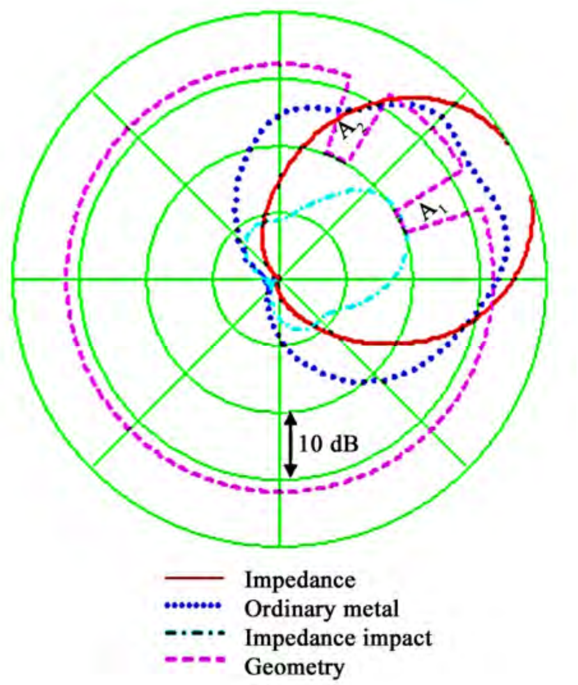

Figure 9. (Color online) Radiation patterns of the structure with the transmitting antenna A_1 ($a=0.4\lambda$, $\varphi_1=20°$, $\varphi_2=30°$) and the receiving antenna A_2 ($b=0.4\lambda$, $\varphi_3=60°$, $\varphi_4=70°$) located on an ideal conducting cylinder (dotted line) and on the reactive impedance Z cylinder (solid line), where the radius is $R=2.387\lambda$ ($kR=15$) and the distance between the antennas is $L=1.25\lambda$. The dashed line represents the geometry of the system

The radiation patterns of a system which has both the transmitting antenna A_1 and the receiving antenna A_2 are presented in **Figure 9**, where the parameters of the system are defined as $a=0.4\lambda$, $\varphi_1=20°$, $\varphi_2=30°$ for A_1, $b=0.4\lambda$, $\varphi_3=60°$, $\varphi_4=70°$ for A_2, the radius of a circular cylinder is $kR=15$,, and the distance between the antennas is $L=1.25\lambda$. The geometry of the structure is depicted as a dashed line. It is clearly seen in **Figure 9** that the radiation pattern for an ideal conducting cylinder (dotted line) is distorted due to the presence of an additional antenna. (Compare to the dotted line in **Figure 5**). On the other hand, the radiation pattern for the capacitive impedance (solid line) is not affected by the presence of a receiving antenna. Hence, the radiation pattern of both antennas coincides with that of a single antenna with a reactive impedance flange. We note that the obtained result here is in the case of frequency- independent impedance. The undistorted radiation pattern will be modified when frequency-dependent surface impedance is used. The impact of the reactive impedance part of the flange on the radiation patterns is indicated as the dash-dotted line.

5. Conclusions

On the basis of the theoretical and numerical research conducted in this paper, we obtained several significant results. First, we calculated a strict solution to the problem of the analysis of the radiation characteristics of a single antenna in the shape of the open end of a parallel-plate waveguide located on the surface of a circular cylinder. Included in this configuration were a reactive impedance flange and a receiving antenna of the same construction; specific boundary conditions of an electric field on the edge were taken into account. Additionally, correlations for the key parameters of the antennas (CSW, radiation patterns of antennas, and the decoupling coefficient) were obtained.

We have also studied the influence of a constant, purely reactive impedance (as a mathematical model of corrugated structures) on the radiation pattern, CSW, and the decoupling level of antennas. These results were obtained with the help of numerical modeling, and coincide well with standard results [16]. A comparative evaluation of the decoupling level on a plane and on the surface of a circular cylinder was performed. A specific difference between a cylindrical surface and a flat one is that for the cylindrical case, increasing the distance between the antennas also increases their screening by means of a surface shadowing.

A study of the radiation pattern for an ideal conducting cylinder showed that the presence of two antennas leads to distortion of their radiation patterns. However, the presence of capacitive impedance almost completely eliminates distortions made by the receiving antenna. The radiation pattern of both antennas coincides with that of a single antenna with a reactive impedance flange.

In conclusion, to reach the required levels of decoupling between antennas, it is necessary to use structures with a complicated reactive impedance corrugation on the flange of the antennas, just as in the case of a plane. For this purpose, in future work we need to study further how to set up and solve the problem of the synthesis of such structures.

6. Acknowledgment

One of the authors (J.-F. D. Essiben) wishes to thank Prof. Yu. V. Yukhanov from Taganrog Institute of Technology at the Southern Federal University in Russia for helpful discussions.

REFERENCES

[1] N. C. Karmakar and M. N. Mollah, "Potential Applications of PBG Engineered Structures in Microwave Engineering," *Microwave Journal*, Horizon House Publications, Inc, London, Vol. 47, 2004, pp. 22-44.

[2] A. Harvey, "Periodic and Guiding Structures at Microwave Frequencies," *IRE Transactions on Microwave Theory and Techniques*, Vol. 8, June 1959, pp. 30-61.

[3] T. C. Rao, "Plane Wave Scattering by a Corrugated Conducting Cylinder at Oblique Incidence," IEEE Transactions on Antennas and Propagation, Vol. 36, August 1988, pp. 1184-1188.

[4] G. Manara, G. Pelosi, A. Monorchio and R. Coccioli, "Plane-Wave Scattering from Cylinders with Transverse Corrugations," *Electronic Letters*, Vol. 31, No. 6, March 1995, pp. 437-438.

[5] A. Freni, "Scattering from a Dielectric Cylinder Axially Loaded with Periodic Metallic Rings," *Proceedings on Institution of Electric and Engineering-Microwave Antennas Propagation*, Vol. 143, No. 3, June 1996, pp. 233-237.

[6] A. Freni, C. Mias and R. L. Ferrari, "Hybrid Finite-Element Analysis of Electromagnetic Plane Wave Scattering from Axially Periodic Cylindrical Structures," *IEEE Transactions on Antennas and Propagation*, Vol. 46, No. 12, December 1998, pp. 1859-1866.

[7] P. S. Kildal, A. A. Kishk and A. Tengs, "Reduction of forward Sscattering from Cylindrical Objects Using Hard Surfaces," *IEEE Transactions on Antennas and Propagation*, Vol. 38, No. 10, October 1990, pp. 1537-1544.

[8] I. Short and K. M. Chen, "Backscattering from an Impedance Loaded Slotted Cylinder," *IEEE Transactions on Antennas and Propagation*, Vol. 17, No. 3, May 1969, pp. 315-323.

[9] A. G. Kurkchan and M. K. Zimnov, "Coupling between Antennas on a Cylinder in the Presence of Corrugated Structures," *Radiotechnics and Electronics*, Vol. 12, No. 9, 1985, pp. 2308-2315.

[10] S. Benenson and A. I. Kurkchan, "Decoupling of Antennas by Means of Periodic Structures," *Radiotechnics and Electronics*, Vol. 37, No. 12, 1995, pp. 77-89.

[11] A. G. Kurkchan, "Coupling between Antennas in the Presence of Corrugated Structures," Radiotechnics and Electronics, Vol. 22, No. 7, 1977, pp. 1362-1373.

[12] K. K. Belostotskaya, M. A. Vasilyev and V. M. Legkov, "Spatial Decouplings between Antennas on Big Size Solids," Radiotechnics, No. 10, pp. 77-79, 1986.

[13] V. G. Koshkidko, B. M. Petrov and Y. V. Yukhanov, "Equivalent Surface Impedance of Passive Impedance Loads on the Basis of a Hole in the Screen, Loaded with a 2D Cavity," *Radiotechnics and Electronics*, Vol. 42, No. 6, pp. 652-661, 1997.

[14] O. N. Tereshin, V. M. Sedov and A. F. Chaplin, "Synthesis of Antennas on Decelerating Structures," Communication Press, Moscow, 1980.

[15] Y. S. Joe, J.-F. D. Essiben and E. M. Cooney, "Radiation Characteristics of Waveguides Antennas Located on the Same Impedance Plane," *Journal of Physics D: Applied Physics*, Vol. 41, 2008.

[16] L. D. Bakhrakh and E. G. Zeikin, "Reference Book on Antenna Engineering," Vol. 1, Moscow, 1997.

APPENDIX A: Calculation of Subsidiary Fields Using Integral Equation

The solution of the integral equations in Equation (11) can numerically be solved by the Krylov-Bogolyubov method [14]. As a result, the integral equation is reduced to a system of linear algebraic equations (SLAE) relative to:
$Y_n = Y(\varphi_n)$:

$$\begin{cases} \sum_{m=1}^{M_{14}} Y_m T_{n,m}^{\langle 1\rangle} = -2H_0 & n = 1\cdots M_1 \\ Y_n f_n^{\langle 2\rangle} - Z_n \sum_{m=1}^{M_{14}} Y_m U_{n,m} = 0 & n = M_1+1\cdots M_{12} \\ \sum_{m=1}^{M_{14}} Y_m T_{n,m}^{\langle 2\rangle} = 0 & n = M_{12}+1\cdots M_{13} \\ Y_n f_n^{\langle 4\rangle} - Z_n \sum_{m=1}^{M_{14}} Y_m U_{n,m} = 0 & \mathrm{n} = M_{13}+1\cdots M_{14}, \end{cases} \tag{A-1}$$

where $f_n^{\langle s\rangle} = f^{\langle s\rangle}(\varphi_n)$, $T_{n,m}^{\langle 1\rangle} = \begin{cases} C_{n,m}^{\langle 1\rangle} & s=1 \\ D_{n,m}^{\langle s\rangle} & s=2,3,4 \end{cases}$,

$$T_{n,m}^{\langle 2\rangle} = \begin{cases} C_{n,m}^{\langle 3\rangle} & s=3 \\ D_{n,m}^{\langle s\rangle} & s=1,2,4 \end{cases}, \quad U_{n,m} = D_{n,m}^{\langle s\rangle}.$$

Here, $D_{n,m}^{\langle s\rangle}$, $C_{n,m}^{\langle 1\rangle}$, and $C_{n,m}^{\langle 3\rangle}$ are defined respectively as follows:

$$D_{n,m}^{\langle s\rangle} = \int_{\varphi_m-\delta}^{\varphi_m+\delta} H_{z1}^m(\varphi_n,\varphi') f^{\langle s\rangle}(\varphi') R d\varphi',$$

$$C_{n,m}^{\langle 1\rangle} = \int_{\varphi_m-\delta}^{\varphi_m+\delta} \left[H_{z1}^m(\varphi_n,\varphi') + H_{z2}^m(\varphi_n,\varphi')\right] f^{\langle 1\rangle}(\varphi') R d\varphi',$$

$$C_{n,m}^{\langle 3\rangle} = \int_{\varphi_m-\delta}^{\varphi_m+\delta} \left[H_{z1}^m(\varphi_n,\varphi') + H_{z3}^m(\varphi_n,\varphi')\right] f^{\langle 3\rangle}(\varphi') R d\varphi'.$$

Finally, $Z_n = Z(\varphi_n) \begin{cases} s=1 & m\in[1,M_1] \\ s=2 & m\in[M_1+1,M_{12}] \\ s=3 & m\in[M_{12}+1,M_{13}] \\ s=4 & m\in[M_{13}+1,M_{14}] \end{cases}$, where M_1, M_2, M_3, M_4 are the numbers of points of collocation on the parts $[\varphi_1,\varphi_2]$, $[\varphi_2,\varphi_3]$, $[\varphi_3,\varphi_4]$, $[\varphi_4,\varphi_1+2\pi]$, and $M_{12} = M_1 + M_2$, $M_{13} = M_{12} + M_3$, $M_{14} = M_{13} + M_4$.

When calculating the solutions of the integral expressions and the coefficients of the matrix of SLAE in Equation (A-1), we have to consider the difficulty of their calculation near the coincidence of the points of integration and collocation $(\varphi \Rightarrow \varphi')$, where the subsidiary fields of Equations (9) and (12) have logarithmic singularities. We observe an opportunity for improving the conformity of the rows in Equations (9) and (12). Different points ($\varphi \neq \varphi'$) in a row in Equation (9), which is shown below as Equation (A-2),

$$\begin{aligned} H_{z2}^m(\varphi,\varphi') &= \frac{i}{2\pi RW} \sum_{n=-\infty}^{\infty} \frac{H_n^{(2)}(kR)}{H_n^{(2)'}(kR)} e^{in(\varphi-\varphi')} \\ &= \frac{i}{2\pi RW} \sum_{n=-\infty}^{\infty} h_n e^{in(\varphi-\varphi')} \end{aligned} \tag{A-2}$$

conform in an unsuitable way, because the coefficients have an asymptote

$$\left.\frac{H_n^{(2)}(kR)}{H_n^{(2)'}(kR)}\right|_{kR\Rightarrow\infty} \approx -\frac{kR}{n} \tag{A-3}$$

In order to improve the conformity of the row in Equation (9), we multiply the Hankel functions in Equation (9) by the Bessel function. Then, we can get asymptotes as a closed form:

$$\left.J_n(kR) H_n^{(2)}(kR)\right|_{kR\Rightarrow\infty} \approx \frac{i}{n\pi} \tag{A-4}$$

which is different from Equation (A-3) by the constant.

J. Electromagnetic Analysis & Applications, **2010, 2: 205-243**
doi:10.4236/jemaa.2010.24029 Published Online April 2010 (http://www.SciRP.org/journal/jemaa)

Intra-Atomic Electric Field Radial Potentials in Step-Like Presentation

Levan Chkhartishvili, Tamar Berberashvili

Department of Physics, Georgian Technical University, Tbilisi, Georgia.
Email: chkharti2003@yahoo.com

Received December 27th, 2009; revised February 8th, 2010; accepted February 15th, 2010.

ABSTRACT

Within the frames of semiclassical approach, intra-atomic electric field potentials are parameterized in form of radial step-like functions. Corresponding parameters for 80 *chemical elements are tabulated by fitting of the semiclassical energy levels of atomic electrons to their first principle values. In substance binding energy and electronic structure calculations, superposition of the semiclassically parameterized constituent-atomic potentials can serve as a good initial approximation of its inner potential: the estimated errors of the determined structural and energy parameters make up a few percent.*

Keywords: *Electric Field Potential, Atoms, Step-Like Radial Functions*

1. Introduction

Because the electron mass is negligible in comparison with masses of atomic nuclei, substances, *i.e.* atoms and polyatomic bound systems – molecules or condensed matters – can be considered as one-electron systems in almost stationary self-consistent electric field generated by nuclei fixed at their equilibrium positions and space-averaged electron charge density. For this reason, electronic structure, which includes both electron energy spectrum and electron density space distribution, determines practically all principal physical properties of a substance. From its part, theoretical prediction of the substance electronic structure should be primarily based on the inner electric field potential, so that appropriate choice of the initial potential for such kind calculations greatly increases their accuracy.

When isolated atoms associate forming molecular or condensed forms of substance only part of electrons (called as valence electrons) redistributes. And what is more, corresponding changes in the electron density distribution are so weak that usually a simple superposition of the free atom's radial potentials centered at the corresponding sites of the atomic structure serves as a good initial approximation of the inner potential in any polyatomic system. At the worst, initial inner electric field potentials can be presented by superposition of the atomic-like radial potentials with different centers. Thus, in this line the key problem consists in construction of the effective atomic potentials in relevant functional form.

Relatively recently, with that end in view we have proposed piece-wise analytical and, in particular, step-like radial atomic potentials obtained within initial quasi-classical, *i.e.*, semiclassical approximation. They have been successfully used in binding energy and electronic structure calculations carried out for some polyatomic systems like the sodium diatomic molecule and crystals [1], boron-containing diatomic molecules [2,3], and mainly for boron nitride molecular, crystalline, and nanostructures [3-16]. In addition, semiclassical interatomic boron-boron pair potentials have explained some ground-state parameters of the boron nanotubes [17-19], as well as main features of the isotopic effects in boron-rich solids [20-23].

But, above cited studies exploited semiclassical potentials only of certain, namely, some light atoms, whereas full-scale calculations performed for any wide class of materials need a quantity of appropriate effective atomic potentials. Present work aims to build up semiclassical atomic potentials for the stable chemical elements in most convenient form of radial step-like functions.

The paper is organized as follows. At first, sense of the semiclassicality for the substance-electron-system is clarified. Then, a semiclassical parameterization scheme is introduced for charge distributions in atoms and atomic potentials as well. Next section presents results and brief discussion of the performed numerical calculations based on fitting of the semiclassical electron-energy spectra with these obtained from first principles. And finally, accuracies of the constructed step-like radial atomic po-

Copyright © 2010 SciRes.

tentials are estimated for energy and expansion parameters of a material.

2. Substance as a Semiclassical Electron System

Beginning from Bohr's fundamental work [24] semiclassically describing electronic spectrum of the one-electron hydrogen-like atom with Coulomb potential up to nowadays, similar analysis is widely used for light atoms. Due to exact quantum-mechanical solvability of the Coulomb potential, exact wave functions of electron-states in a hydrogen-like atom can be obtained directly from the corresponding classical orbits [25]. And therefore, quantum dynamics of the electron in a hydrogen-like atom is wholly expressed by its classical dynamics.

Classically a two-electron helium-like atom can be represented as a pair of electrons placed at the opposite ends of the straight line with nucleus at the midpoint (see e.g. [26]). This classical model added with quantization condition for electron orbital moment leads to the almost hydrogen-like electron energy spectra, where atomic number Z is substituted for the reduced value Z–1/4 (it means that another electron effectively screens nuclear electric charge). Ground state energies calculated from the obtained relation for some helium-like systems differ from the experimental ones only by 3-6% [27]. Even entirely classical model of helium atom can be successfully explored numerically to obtain its possible configurations [28]: most of the orbits are found to cause autoionization via chaotic transients. As for the modern semiclassical approach based on the conception of periodic classical orbits, it allow visually interpret physical meaning of special quantum numbers inherent to this three-particle system between ground and fragmented states [29].

For many-electron atoms, a reasonable accuracy can be achieved in terms of the self-consistent-field approximation, within which a minimum of the total energy is sought in the class of quasi-classical wave functions [30]. As is well known, many-electron systems such as heavy atoms are characterized by some quantum properties like the electron-shell effects, fluctuations in parameters' values, discrete electron energy spectrum etc, which are averaged and, therefore, invisible in semiclassical atomic models. However, it was demonstrated that semiclassical treatment of the atomic many-electron system, when it is combined with information-theory-method, reveals resources to describe such kind effects as well [31].

It was demonstrated how based on purely classical notions it is possible to reproduce general trends in inelastic scattering atomic form-factors dependences upon quantum numbers [32]. Besides, starting from classical relations together with energy conservation law and classical-quantum correspondence principle, it was found expressions of intensity-distribution and line-width of the electron–ion recombination X-ray spectrum, which is in unexpectedly good agreement with these resulted from the accurate quantum-mechanical calculations [33].

Semiclassical quantization rule leading to the exact electron energies in a hydrogen-like atom with Coulomb potential at the same time provides good accuracy of the valence electron energy value in a many-electron atom with model potential in form of sum of the nucleus Coulomb potential and a screening term [34]. Substitutions of the electron quantum numbers for their analogues in Thomas–Fermi semiclassical statistical model of atom can be applied for investigation of the excited and ionized electron states [35]. Semiclassical electron energy spectrum of Thomas–Fermi atom, which was described in terms of an effective kinetic energy obtained from the corresponding quantization rule formulated in momentum space, was found to agree essentially with that in the standard formalism employing an effective potential energy [36].

Semiclassical evaluation of sums over quantum numbers of electron states in many-electron atoms is known to be an effective tool of obtaining of the integrated atomic characteristics (see e.g. [37]) like the shell and subshell electron densities [38] or averaged electron momentum density [39] in atoms etc. Introducing of the semiclassical self-consistent intra-atomic electric field yields the relative error not more than $\sim 1/\pi^2 n^2$ in determining of the electronic energies, where n is the principal quantum number of the highest occupied electron state [40]. Then, accuracy of the semiclassical approximation should quite satisfactory even for light atoms.

Effectiveness of the Bohr-type analytical models to the description of the periodic motion of electrons in small-sized molecules also was demonstrated [41]. For a long time, semiclassical asymptotic form was known to provide a fundamental device for studying quantum systems in which non-perturbative effects play an essential role. But, the crucial step was advanced for the bound-state quantization of fermions few-body systems such as molecules. Semiclassical quantization rules were successfully applied to describe elastic interatomic scattering [42] in spectroscopy of diatomic molecules [43]. Using path integration as a relevant mathematical tool for semiclassical asymptotic form it was obtained semiclassical quantization rule for the periodic mean-field solutions [44]. Therm energies of diatomic K_2 molecule calculated by the semiclassical method showed absolute deviations of only ~ 0.05 cm^{-1} from the quantum-mechanical results [45]. Same approach was found to be a strong method for generating the interatomic potential energy curve for diatomic molecules. It was provided a semiclassical description of the shell-structure in fermions-system: level densities and shell-corrections were obtained from the periodic orbit theory [46]. The semiclassical quantification method has raised increasing interest in relation to approximated method in various physical systems such as not only atoms, but molecules etc. It would serve as a general device for evaluating the bound-state spectra, once the exact or approximate solutions for the mean-field equation are known. Usually, different methods all use only periodic and/or non-closed quasi-periodic classical orbitals as basis for the quantization. Contrary to them, in [47] it was introduced an adapted version of the semiclassical quantization method applied to molecular orbitals into path integrals formalism, and it also gives an alternative procedure for the calculation of the electronic correlation energy of a molecular system.

Primitive semiclassical treatment even reveals existence of a classical contribution to the chemical bond in small molecules: ground state electron is found to be exchanged classically between two nuclei [48]. Proceeding classical limit for a one-electron orbital model of such many-electron systems with electron periodic motion leads to visualization of its quantum description [49]. Quantum description also can be introduced starting from the formal correspondence between classical harmonics of an electron periodic motion and its quantum jumps, *i.e*. Fourier-analysis added by the simple quantization condition directly yields steady-state electron energies [50]. Even formation of the electron spin, which is considered as essentially quantum characteristic, can be explained within a classical model [51].

In case of multidimensional systems, the globally uniform semiclassical approximation for energy eigenstates can be derived explicitly [52]. This is a true semiclassical approximation producing almost accurate wave functions providing with considerable degree of overlap (more than 0.98) between semiclassical and exact quantum eigenstates. Semiclassical method of calculation was used to describe electronic super-shells in metallic clusters [53]. Later, it was supposed a general method of the quasi-classical spectral analysis useful for central potentials with Coulomb singularity or finite value at the center which are characteristic for isolated atoms and spherical clusters, respectively [54]. Atomic clusters and condensed phases can be calculated in framework of the density-functional theory (DFT) using a quasi-classical expansion of the energy functional [55].

However, as substance is considered as a non-relativistic electron system affected by the external field of nuclei fixed at their sites in structure, its inner potential do not satisfy the standard Wentzel-Kramers-Brillouin (WKB) quasi-classical condition on spatial smoothness due to singularities at nuclear sites and electron shell effects. The success of the above approaches can be explained on the basis of the quasi-classical expressions obtained by Maslov [56] for the energies of bound electronic states. It follows from these expressions that the exact and quasi-classical spectra are similar to each other irrespective of the potential smoothness at $2\Phi_0 R_0^2 >> 1$, where Φ_0 and R_0 are the characteristic values of the potential and its effective range, respectively (hereafter, all relationships will be given in the atomic system of units (a.u.)).

3. Semiclassical Parameterization of the Electric Charge Density and Electric Field Potential Distributions in an Atom

The semiclassical parameterization of the atomic electric charge density and electric field potential distributions (see e.g. [57]) can be performed in analytical form if the effective fields acting on any i th electron in a neutral atom (*i.e.*, $i = 1,2,3,...,Z$ with Z as the nucleus charge) are represented by Coulomb-like potentials

$$\Phi_i(r) = \frac{Z_i}{r} \tag{1}$$

where

$$Z_i = n_i \sqrt{2\,|\,E_i\,|} \tag{2}$$

is the effective charge of the nucleus screened by other electrons' cloud dependent on the electron-state principal quantum number n_i and its energy $E_i < 0$.

Electron charge equals to -1. Therefore, classical turning points radii r_i' and r_i'' ($r_i' < r_i''$) of the i th electron with orbital quantum number l_i can be found as the roots of the equation

$$E_i = -\Phi_i(r) + \frac{l_i(l_i+1)}{2r^2} \tag{3}$$

As a result, we obtain

$$r_i' = \frac{n_i - \sqrt{n_i^2 - l_i(l_i+1)}}{\sqrt{2\,|\,E_i\,|}} \tag{4}$$

$$r_i'' = \frac{n_i + \sqrt{n_i^2 - l_i(l_i+1)}}{\sqrt{2\,|\,E_i\,|}} \tag{5}$$

Let $\tilde{\Phi}_i(r)$ be the potential of the effective electric field induced by the i th electron. Then, potential $\tilde{\Phi}(r)$ of the electric field induced by the whole electron cloud can be written as the sum of the potentials $\tilde{\Phi}_i(r)$:

$$\tilde{\Phi}(r) = \sum_{i=1}^{i=Z} \tilde{\Phi}_i(r) \tag{6}$$

Potential of the electric field acting on an arbitrary i th electron of the atom is equal to the sum of the potentials of the nucleus Coulomb field and the field induced by all the electrons, except for the potential of the electron under consideration:

$$\frac{Z_i}{r} = \frac{Z}{r} + \tilde{\Phi}(r) - \tilde{\Phi}_i(r) \quad (7)$$

Now, we sum up such potentials over electrons. As a result, the terms independent of the electron number on the right-hand sides are multiplied by the total number Z of electrons in the atom and the sum of the potentials $\tilde{\Phi}_i(r)$ gives $\tilde{\Phi}(r)$. The solution of the obtained equation with respect to $\tilde{\Phi}(r)$ has the form

$$\tilde{\Phi}(r) = -\frac{Z^2 - \sum_{i=1}^{i=Z} Z_i}{Z-1}\frac{1}{r} \quad (8)$$

i.e. in this case, effective field of the interaction between nucleus and electron cloud also turns out to be a Coulomb-like field.

Nucleus charge equals to $+Z$ and in the ground state its relative (to the electron cloud) motion corresponds to a zero orbital quantum number. Therefore, the radius of one classical turning point for nucleus is equal to 0 and the radius $\tilde{r}$ of another turning point is a root of the equation

$$\tilde{E} = Z\tilde{\Phi}(r) \quad (9)$$

where $\tilde{E}$ is the eigenvalue of the energy associated with the relative motion electron cloud and nucleus. Under the assumption that the nucleus has an infinite mass the reduced mass of the system nucleus – electron cloud with *Z* electrons equals to the cloud total mass *Z*. Therefore, energy and, consequently, turning point radius for the nucleus motion with respect to the electron cloud are given by the formulas

$$\tilde{E} = -\frac{Z^3\left(Z^2 - \sum_{i=1}^{i=Z} Z_i\right)^2}{2(Z-1)^2} \quad (10)$$

$$\tilde{r} = \frac{2(Z-1)}{Z^2\left(Z^2 - \sum_{i=1}^{i=Z} Z_i\right)} \quad (11)$$

The semiclassical, *i.e.*, initial quasi-classical approximation implies that exponentially decaying partial electron densities are disregarded in the classically forbidden regions and that oscillations of these densities are ignored in classically allowed regions. As a result, the radial dependence of the direction-averaged partial charge density of the i th electron state in atom is represented by a piecewise constant function:

$$\begin{aligned} \rho_i(r) &= 0 && r < r_i' \\ &= -\frac{3}{4\pi(r_i''^3 - r_i'^3)} && r_i' \le r \le r_i'' \\ &= 0 && r_i'' < r \end{aligned} \quad (12)$$

A similar averaging for the nucleus motion with respect to the electron cloud nucleus is equivalent to averaging the nuclear charge over a sphere of radius $\tilde{r}$:

$$\begin{aligned} \tilde{\rho}(r) &= \frac{3Z}{4\pi\tilde{r}^3} && 0 \le r \le \tilde{r} \\ &= 0 && \tilde{r} < r \end{aligned} \quad (13)$$

Summation of similar contributions gives the distribution of the total density of the electric charge in the atom in the form of a step radial function

$$\rho(r) = \tilde{\rho}(r) + \sum_{i=1}^{i=Z} \rho_i(r) = \rho_k$$

$$R_{k-1} \le r < R_k \quad k = 1,2,3,\ldots,q \quad (14)$$

where ρ_k are constants determined from the radii of the classical turning points and R_k coincide with these radii. Here, $0 \equiv R_0 < R_1 < R_2 < \cdots < R_q < R_{q+1} \equiv \infty$ and $q \le 2Z$ is the number of layers with uniform charge densities. Parameter R_q plays the role of the quasi-classical atomic radius (the charge density is equal to zero at $r > R_q$). Mathematically, this representation is equivalent to the volume averaging in layers $R_{k-1} \le r < R_k$.

Next, we calculate the fields induced by the charged layers with densities ρ_k on the basis of the Gauss theorem and sum these fields. Then, the atomic potential can be written in the form of the continuously differentiable piecewise analytical function

$$\phi(r) = \frac{a_k}{r} + b_k r^2 + c_k \qquad R_{k-1} \le r < R_k \qquad k = 1,2,3,\ldots,q$$

$$\begin{aligned} a_k &= \frac{4\pi}{3}\sum_{i=1}^{i=k-1} \rho_i (R_i^3 - R_{i-1}^3) - \frac{4\pi}{3}\rho_k R_{k-1}^3 \\ b_k &= -\frac{2\pi}{3}\rho_k \\ c_k &= 2\pi \sum_{i=k+1}^{i=q} \rho_i (R_i^2 - R_{i-1}^2) + 2\pi\rho_k R_k^2 \end{aligned} \quad (15)$$

However, since the energy of the electronic system is a single-valued functional of the electron density, it is expedient to approximate the above potential by a step function too. Averaging over the volume can adequately perform this:

$$\varphi(r) = \frac{3a_k(R_k^2 - R_{k-1}^2)}{2(R_k^3 - R_{k-1}^3)} + \frac{3b_k(R_k^5 - R_{k-1}^5)}{5(R_k^3 - R_{k-1}^3)} + c_k = \varphi_k$$

$$R_{k-1} \le r < R_k \qquad k = 1,2,3,\ldots,q \quad (16)$$

4. Tables

The numerical values of parameters R_k, ρ_k, and φ_k can be found by fitting quasi-classical energetic levels E_i to the Hartree–Fock (HF) ab initio ones [58]. Results of calculation are presented in **Table 1** below for each

Copyright © 2010 SciRes.

chemical element taken separately. Origin of a radial layer radius is identified in parenthesis after the layer number: is it a classical turning point radius of nucleus or an electron-state? Note that inner turning points of nucleus and *s*-electron states coincide with effective atomic electric field center, *i.e.* corresponding radii equal to 0. Radii of inner and outer classical turning points for rest electron-states are distinguished by single and double priming.

Values are shown with seven significant digits in accordance with the input data (HF energies) accuracy. Such high accuracy is useful in interim calculations. As for the final results, they should be expressed in round numbers to the three or four significant digits because the relative errors of the semiclassical calculations aiming to found structural and energy parameters for polyatomic systems usually make up a few percent.

Table 1. Calculated semiclassical parameters of the atoms

k	1 (**1 H**)	1 (1*s*)
R_k	1.000000 E + 00	2.000000 E + 00
ρ_k	2.088909 E + 01	−2.984155 E – 02
φ_k	4.875000 E − 01	5.892857 E − 02

k	1 (**2 He**)	2 (1*s*)
R_k	3.875716 E − 01	1.476061 E + 00
ρ_k	8.052884 E + 00	−1.484666 E − 01
φ_k	4.187991 E + 00	3.082284 E − 01

k	1 (**3 Li**)	2 (1*s*)	3 (2*s*)
R_k	1.349014 E − 01	8.984357 E − 01	6.383510 E + 00
ρ_k	2.910724 E + 02	−6.593034 E − 01	− 9.177675 E − 04
φ_k	2.312713 E + 01	2.009273 E + 00	4.311415 E − 02

k	1 (**4 Be**)	2 (1*s*)	3 (2*s*)
R_k	5.596220 E − 02	6.500727 E − 01	5.086001 E + 00
ρ_k	5.446885 E + 03	−1.741653 E + 00	3.629210 E − 03
φ_k	8.057431 E + 01	4.887950 E + 00	1.097914 E − 01

k	1 (**5 B**)	2 (1*s*)	3 (2*p*')	4 (2*s*)	5 (2*p*")
R_k	2.758476 E − 02	5.098016 E − 01	7.441219 E − 01	4.021346 E + 00	4.337060 E + 00
ρ_k	5.686514 E + 04	− 3.610951 E + 00	− 7.342212 E − 03	− 1.028341 E − 02	− 2.941197 E − 03
φ_k	2.105468 E + 02	8.882329 E + 00	3.652920 E + 00	2.060720 E − 01	6.135348 E − 04

k	1 (**6 C**)	2 (1*s*)	3 (2*p*')	4 (2*s*)	5 (2*p*")
R_k	1.542721 E − 02	4.202289 E − 01	6.292303 E − 01	3.367110 E + 00	3.667423 E + 00
ρ_k	3.901153 E + 05	−6.446545 E + 00	− 1.250747 E − 02	− 2.223623 E − 02	− 9.728757 E − 03
φ_k	578818 E + 02	1.399183 E + 01	5.842260 E + 00	3.410756 E − 01	1.835877 E−03

k	1 (**7 N**)	2 (1*s*)	3 (2*p*')	4 (2*s*)	5 (2*p*")
R_k	9.446222 E − 03	3.577244 E − 01	5.498034 E − 01	2.909074 E + 00	3.204489 E + 00
ρ_k	1.982589 E + 06	− 1.044967 E + 01	− 1.939444 E − 02	− 4.126981 E − 02	− 2.187537 E − 02
φ_k	8.784581 E + 02	2.022523 E + 01	8.464698 E + 00	5.096684 E − 01	3.993358 E − 03

Copyright © 2010 SciRes.

k	1 (**8 O**)	2 (1*s*)	3 (2*p*')	4 (2*s*)	5 (2*p*")
R_k	6.103946 E − 03	3.110705 E −01	5.210723 E − 01	2.535595 E + 00	3.037032 E + 00
ρ_k	8.397857 E + 06	− 1.589154 E + 01	− 2.928881 E − 02	− 6.355156 E − 02	− 3.426275 E − 02
φ_k	1.559999 E + 03	2.773984 E + 01	1.102222 E + 01	7.898878 E − 01	1.796550 E − 02

k	1 (**9 F**)	2 (1*s*)	3 (2*p*')	4 (2*s*)	5 (2*p*")
R_k	4.176561 E − 03	2.753309 E − 01	4.847945 E − 01	2.255511 E + 00	2.825589 E + 00
ρ_k	2.949151 E + 07	− 2.291743 E + 01	− 4.161086 E − 02	− 9.479146 E − 02	− 5.318060 E − 02
φ_k	2.571045 E + 03	3.638866 E + 01	1.405815 E + 01	1.114922 E + 00	3.595575 E − 02

k	1 (**10 Ne**)	2 (1*s*)	3 (2*p*')	4 (2*s*)	5 (2*p*")
R_k	2.985142 E − 03	2.470362 E − 01	4.491695 E − 01	2.035740 E + 00	2.617951 E + 00
ρ_k	8.974622 E + 07	− 3.172744 E + 01	− 5.659451 E − 02	− 1.368319 E − 01	− 8.023741 E − 02
φ_k	4.002938 E + 03	4.617305 E + 01	1.754276 E + 01	1.481199 E + 00	5.649046 E − 02

k	1 (**11 Na**)	2 (1*s*)	3 (2*p*')
R_k	2.333813 E − 03	2.222812 E − 01	3.361773 E − 01
ρ_k	2.065883 E + 08	− 4.357330 E + 01	− 9.895069 E − 02
φ_k	5.636078 E + 03	5.702576 E + 01	2.540262 E + 01

4 (2*s*)	5 (2*p*")	6 (3*s*)
1.691207 E + 00	1.959385 E + 00	9.942100 E + 00
− 2.903333 E − 01	− 1.916255 E − 01	− 2.429277 E − 04
2.264005 E + 00	4.264542 E − 01	2.565704 E − 02

k	1 (**12 Mg**)	2 (1*s*)	3 (2*p*')
R_k	1.833883 E − 03	2.019651 E − 01	2.741860 E − 01
ρ_k	4.644914 E + 08	− 5.811295 E + 01	− 1.551165 E − 01
φ_k	7.829429 E + 03	6.933347 E + 01	3.379468 E + 01

4 (2*s*)	5 (2*p*")	6 (3*s*)
1.457155 E + 00	1.598073 E + 00	8.433944 E + 00
− 5.078705 E − 01	− 3.535498 E − 01	− 7.958830 E − 04
3.315594 E + 00	9.711561 E − 01	6.118891 E − 02

k	1 (**13 Al**)	2 (1*s*)	3 (2*p*')	4 (3*p*')
R_k	1.462229 E − 03	1.848984 E − 01	2.308930 E − 01	5.466816 E − 01
ρ_k	9.926781 E + 08	− 7.576501 E + 01	− 2.311670 E − 01	− 8.218780 E − 01
φ_k	1.064293 E + 04	8.299728 E + 01	4.322824 E + 01	1.753508 E + 01

5 (2*s*)	6 (2*p*")	7 (3*s*)	8 (3*p*")
1.276364 E + 00	1.345743 E + 00	6.764067 E + 00	8.712604 E + 00
− 8.222391 E − 01	− 5.926148 E − 01	− 1.903885 E − 03	− 3.610562 E − 04
3.600567 E + 00	1.684978 E + 00	1.386415 E − 01	2.846971 E − 03

k	1 (**14 Si**)	2 (1*s*)	3 (2*p*')	4 (3*p*')
R_k	1.177767 E − 03	1.704832 E − 01	2.007802 E − 01	4.595484 E − 01
ρ_k	2.045794 E + 09	− 9.668486 E + 01	− 3.248175 E − 01	− 1.223166 E + 00
φ_k	1.423563 E + 04	9.804605 E + 01	5.346299 E + 01	2.372269 E + 01

5 (2*s*)	6 (2*p*")	7 (3*s*)	8 (3*p*")
1.139926 E + 00	1.170233 E + 00	5.774354 E + 00	7.323940 E + 00
− 1.224381 E + 00	− 9.020437 E − 01	− 3.695549 E − 03	− 1.215666 E − 03
5.013770 E + 00	2.545996 E + 00	2.317236 E − 01	6.068273 E − 03

k	1 (**15 P**)	2 (1*s*)	3 (2*p*')	4 (3*p*')
R_k	9.593563 E − 04	1.581438 E − 01	1.782334 E − 01	4.002321 E − 01
ρ_k	4.055672 E + 09	− 1.211595 E + 02	− 4.380049 E − 01	− 1.722228 E + 00
φ_k	1.873096 E + 04	1.144569 E + 02	6.457731 E + 01	3.040964 E + 01

5 (2*s*)	6 (2*p*")	7 (3*s*)	8 (3*p*")
1.032033 E + 00	1.038820 E + 00	5.083961 E + 00	6.378601 E + 00
− 1.724988 E + 00	− 1.290617 E + 00	− 6.393927 E − 03	− 2.760347 E − 03
6.608240 E + 00	3.548359 E + 00	3.396463 E − 01	9.624267 E − 03

k	1 (**16 S**)	2 (1*s*)	3 (2*p*')	4 (3*p*')
R_k	7.873147 E − 04	1.474384 E − 01	1.602340 E − 01	3.787647 E − 01
ρ_k	7.826836 E + 09	− 1.495490 E + 02	− 5.752957 E − 01	− 2.342732 E + 00
φ_k	2.435211 E + 04	1.322761 E + 02	7.674520 E + 01	3.528555 E + 01

5 (2*p*")	6 (2*s*)	7 (3*s*)	8 (3*p*")
9.339120 E − 01	9.425845 E − 01	4.523887 E + 00	6.036469 E + 00
− 2.347074 E + 00	− 5.796381 E − 01	− 9.499509 E − 03	− 4.342400 E − 03
8.375741 E + 00	4.756158 E + 00	5.098488 E − 01	2.058169 E − 02

k	1 (**17 Cl**)	2 (1*s*)	3 (2*p*')	4 (3*p*')
R_k	6.532226 E − 04	1.380891 E − 01	1.457901 E − 01	3.520031 E − 01
ρ_k	1.456052 E + 10	− 1.820631 E + 02	− 7.359436 E − 01	− 3.082461 E + 00
φ_k	3.119221 E + 04	1.514459 E + 02	8.983302 E + 01	4.146700 E + 01

5 (2*p*")	6 (2*s*)	7 (3*s*)	8 (3*p*")
8.497267 E − 01	8.684381 E − 01	4.095949 E + 00	5.609963 E + 00
− 3.089224 E + 00	− 7.427061 E − 01	− 1.371081 E − 02	− 6.762524 E − 03
1.047479 E + 01	6.101408 E + 00	6.943084 E − 01	3.204793 E − 02

k	1 (**18 Ar**)	2 (1*s*)	3 (2*p*')	4 (3*p*')
R_k	5.474781 E − 04	1.298535 E − 01	1.338860 E − 01	3.258315 E − 01
ρ_k	2.618688 E + 10	− 2.189839 E + 02	− 9.217434 E − 01	− 3.951462 E + 00
φ_k	3.941303 E + 04	1.719603 E + 02	1.038562 E + 02	4.862917 E + 01

Copyright © 2010 SciRes.

5 (2*p*")	6 (2*s*)	7 (3*s*)	8 (3*p*")
7.803446 E − 01	8.057526 E − 01	3.753883 E + 00	5.192860 E + 00
− 3.961694 E + 00	− 9.319752 E − 01	− 1.925783 E − 02	− 1.023175 E − 02
1.282209 E + 01	7.582522 E + 00	8.919572 E − 01	4.376578 E − 02

k	1 (**19 K**)	2 (2*p*')	3 (1*s*)	4 (3*p*')	5 (2*p*")
R_k	4.727958 E − 04	1.220427 E − 01	1.223829 E − 01	2.564030 E − 01	7.113169 E − 01
ρ_k	4.291847 E + 10	− 2.616615 E + 02	− 2.656616 E + 02	− 5.178522 E + 00	− 5.199519 E + 00
φ_k	4.817966 E + 04	1.942944 E + 02	1.195273 E + 02	6.680192 E + 01	1.623827 E + 01

6 (2*s*)	7 (3*s*)	8 (3*p*")	9 (4*s*)
7.430389 E − 01	3.208255 E + 00	4.086360 E + 00	1.473043 E + 01
− 1.199407 E + 00	− 3.553070 E − 02	− 2.107182 E − 02	− 7.469050 E − 05
9.178612 E + 00	1.258072 E + 00	2.068058 E − 01	1.499003 E − 02

k	1 (**20 Ca**)	2 (2*p*')	3 (1*s*)	4 (3*p*')	5 (2*p*")
R_k	4.088020 E − 04	1.121988 E − 01	1.157157 E − 01	2.163349 E − 01	6.539423 E − 01
ρ_k	6.988798 E + 10	− 3.096286 E + 02	− 3.147766 E + 02	− 6.625287 E + 00	− 6.660246 E + 00
φ_k	5.866054 E + 04	2.246811 E + 02	1.363192 E + 02	8.373755 E + 01	1.982931 E + 01

6 (2*s*)	7 (3*s*)	8 (3*p*")	9 (4*s*)
6.895990 E − 01	2.831339 E + 00	3.447784 E + 00	1.279289 E + 01
− 1.512189 E + 00	− 5.622245 E − 02	− 3.518632 E − 02	− 2.280529 E − 04
1.103673 E + 01	1.726474 E + 00	4.329498 E − 01	3.507845 E − 02

k	1 (**21 Sc**)	2 (2*p*')	3 (1*s*)	4 (3*p*')
R_k	3.495658 E − 04	1.046439 E − 01	1.097974 E − 01	1.996252 E − 01
ρ_k	1.173664 E + 11	− 3.625008 E + 02	− 3.688463 E + 02	− 8.130180 E + 00
φ_k	7.203863 E + 04	2.552117 E + 02	1.537630 E + 02	9.620138 E + 01

5 (2*p*")	6 (2*s*)	7 (3*d*')	8 (3*s*)
6.099095 E − 01	6.475133 E − 01	1.529288 E + 00	2.647865 E + 00
− 8.174672 E + 00	− 1.829179 E + 00	− 7.046518 E − 02	− 7.177448 E − 02
2.333772 E + 01	1.310249 E + 01	5.350410 E + 00	1.412970 E + 00

9 (3*p*")	10 (4*s*)	11 (3*d*")
3.181477 E + 00	5.707379 E + 00	1.234108 E + 01
− 4.605550 E − 02	− 1.563323 E − 03	− 2.540280 E − 04
5.766749 E − 01	2.237779 E − 01	2.179856 E − 02

k	1 (**22 Ti**)	2 (2*p*')	3 (1*s*)	4 (3*p*')
R_k	3.013518 E − 04	9.820236 E − 02	1.044639 E − 01	1.869609 E − 01
ρ_k	1.919167 E + 11	− 4.209588 E + 02	− 4.286367 E + 02	− 9.801412 E + 00
φ_k	8.755133 E + 04	2.872142 E + 02	1.721800 E + 02	1.087104 E + 02

5 (2*p*")	6 (2*s*)	7 (3*d*')	8 (3*s*)
5.723653 E − 01	6.110909 E − 01	1.908091 E + 00	2.502871 E + 00
− 9.855572 E + 00	− 2.177684 E + 00	− 8.538408 E − 02	− 8.673223 E − 02
2.709414 E + 01	1.537353 E + 01	4.186494 E + 00	1.335356 E + 00

9 (3*p*")	10 (3*d*")	11 (4*s*)
2.979643 E + 00	7.121092 E + 00	8.521671 E + 00
− 5.627954 E − 02	− 2.119704 E − 03	− 7.715554 E − 04
7.476607 E − 01	1.196428 E − 01	3.156347 E − 03

k	1 (**23 V**)	2 (2*p*')	3 (1*s*)	4 (3*p*')
R_k	2.601095 E − 04	9.256893 E − 02	9.962640 E − 02	1.762791 E − 01
ρ_k	3.120117 E + 11	− 4.853546 E + 02	− 4.945213 E + 02	− 1.166471 E + 01
φ_k	1.060522 E + 05	3.209083 E + 02	1.916313 E + 02	1.217554 E + 02

5 (2*p*")	6 (2*s*)	7 (3*d*')	8 (3*s*)
5.395313 E − 01	5.788639 E − 01	1.867140 E + 00	2.377964 E + 00
− 1.172932 E + 01	− 2.562651 E + 00	− 1.010817 E − 01	− 1.032399 E − 01
3.114340 E + 01	1.785930 E + 01	4.730460 E + 00	1.618205 E + 00

9 (3*p*")	10 (3*d*")	11 (4*s*)
2.809404 E + 00	6.968261 E + 00	7.924130 E + 00
− 6.773191 E − 02	− 3.117812 E − 03	− 9.595919 E − 04
9.784493 E − 01	1.402956 E − 01	1.832263 E − 03

k	1 (**24 Cr**)	2 (2*p*')	3 (1*s*)	4 (3*p*')
R_k	2.257520 E − 04	8.758647 E − 02	9.521818 E − 02	1.670378 E − 01
ρ_k	4.979986 E + 11	− 5.559828 E + 02	− 5.668046 E + 02	− 1.373243 E + 01
φ_k	1.275136 E + 05	3.562990E + 02	2.121004E + 02	1.353698E + 02

5 (2*p*")	6 (2*s*)	7 (3*d*')	8 (3*s*)
5.104914 E − 01	5.500740 E − 01	1.831115 E + 00	2.268075 E + 00
− 1.380838 E + 01	− 2.986651 E + 00	− 1.179983 E − 01	− 1.210491 E − 01
3.546478 E + 01	2.053528 E + 01	5.299796 E + 00	1.929230 E + 00

9 (3*p*")	10 (3*d*")	11 (4*s*)
2.662124 E + 00	6.833814 E + 00	7.498190 E + 00
− 8.012597 E − 02	− 4.183420 E − 03	− 1.132588 E − 03
1.243684 E + 00	1.661301 E − 01	1.045829 E − 03

k	1 (**25 Mn**)	2 (2*p*')	3 (1*s*)	4 (3*p*')
R_k	1.970173 E − 04	8.315498 E − 02	9.118571 E − 02	1.590773 E − 01
ρ_k	7.804374 E + 11	− 6.331017 E + 02	− 6.457474 E + 02	− 1.600771 E + 01
φ_k	1.522077 E + 05	3.933287 E + 02	2.335698 E + 02	1.494468 E + 02

5 (2*p*")	6 (2*s*)	7 (3*d*')	8 (3*s*)
4.846627 E − 01	5.242371 E − 01	1.800835 E + 00	2.171677 E + 00
− 1.609563 E + 01	− 3.449931 E + 00	− 1.358885 E − 01	− 1.398977 E − 01
4.004232 E + 01	2.339427 E + 01	5.880152 E + 00	2.258767 E + 00

9 (3*p*")	10 (3*d*")	11 (4*s*)
2.535256 E + 00	6.720807 E + 00	7.077436 E + 00
− 9.327942 E − 02	− 5.355993 E − 03	− 1.346833 E − 03
1.535328 E + 00	1.929413 E − 01	3.586332 E − 04

k	1 (**26 Fe**)	2 (2*p*')	3 (1*s*)	4 (3*p*')
R_k	1.728400 E − 04	7.911165 E − 02	8.747507 E − 02	1.512669 E − 01
ρ_k	1.202131 E + 12	− 7.171896 E + 02	− 7.318750 E + 02	− 1.854820 E + 01
φ_k	1.804475 E + 05	4.323994 E + 02	2.561417 E + 02	1.647530 E + 02

5 (2*p*")	6 (2*s*)	7 (3*d*')	8 (3*s*)
4.610965 E − 01	5.005045 E − 01	1.764513 E + 00	2.077770 E + 00
− 1.865046 E + 01	− 3.965039 E + 00	− 1.568596 E − 01	− 1.619738 E − 01
4.495410 E + 01	2.645283 E + 01	6.529329 E + 00	2.639717 E + 00

9 (3*p*")	10 (3*d*")	11 (4*s*)
2.410779 E + 00	6.585254 E + 00	7.033322 E + 00
− 1.087447 E − 01	− 6.486578 E − 03	− 1.372334 E − 03
1.883139 E + 00	2.331049 E − 01	5.767085 E − 04

k	1 (**27 Co**)	2 (2*p*')	3 (1*s*)	4 (3*p*')
R_k	1.524057 E − 04	7.547369 E − 02	8.405654 E − 02	1.444711 E − 01
ρ_k	1.820837 E + 12	− 8.083521 E + 02	− 8.252652 E + 02	− 2.131927 E + 01
φ_k	2.125211 E + 05	4.731134 E + 02	2.797123 E + 02	1.805247 E + 02

5 (2*p*")	6 (2*s*)	7 (3*d*')	8 (3*s*)
4.398929 E − 01	4.789933 E − 01	1.733761 E + 00	1.994624 E + 00
− 2.143665 E + 01	− 4.523643 E + 00	− 1.790090 E − 01	− 1.852988 E − 01
5.011827 E + 01	2.969002 E + 01	7.183303 E + 00	3.034107 E + 00

9 (3*p*")	10 (3*d*")	11 (4*s*)
2.302473 E + 00	6.470483 E + 00	6.883165 E + 00
− 1.251318 E − 01	− 7.753902 E − 03	− 1.464120 E − 03
2.253930 E + 00	2.716290 E − 01	5.219691 E − 04

k	1 (**28 Ni**)	2 (2*p*')	3 (1*s*)	4 (3*p*')
R_k	1.350222 E − 04	7.216906 E − 02	8.089558 E − 02	1.383599 E − 01
ρ_k	2.715524 E + 12	− 9.069139 E + 02	− 9.262582 E + 02	− 2.434036 E + 01
φ_k	2.487756 E + 05	5.155529 E + 02	3.043036 E + 02	1.969151 E + 02

Copyright © 2010 SciRes.

5 (2*p*")	6 (2*s*)	7 (3*d*')	8 (3*s*)
4.206321 E − 01	4.593284 E − 01	1.705828 E + 00	1.919013 E + 00
− 2.447399 E + 01	− 5.129635 E + 00	− 2.027591 E − 01	− 2.103064 E − 01
5.555121 E + 01	3.311022 E + 01	7.853485 E + 00	3.448915 E + 00

9 (3*p*")	10 (3*d*")	11 (4*s*)
2.205076 E + 00	6.366238 E + 00	6.728001 E + 00
− 1.427436 E − 01	− 9.115030 E − 03	− 1.567773 E − 03
2.654621 E + 00	3.114798 E − 01	4.295498 E − 04

k	1 (**29 Cu**)	2 (2*p*')	3 (1*s*)	4 (3*p*')
R_k	1.220837 E − 04	6.915185 E − 02	7.796404 E − 02	1.328183 E − 01
ρ_k	3.804836 E + 12	− 1.013164 E + 03	− 1.035152 E + 03	− 2.762119 E + 01
φ_k	2.849738 E + 05	5.586503 E + 02	3.288432 E + 02	2.128615 E + 02

5 (2*p*")	6 (2*s*)	7 (3*d*')	8 (3*s*)
4.030465 E − 01	4.412704 E − 01	1.042111 E + 00	1.849776 E + 00
− 2.777226 E + 01	− 5.783729 E + 00	− 2.269000 E − 01	− 2.641396 E − 01
6.017921 E + 01	3.563878 E + 01	1.517850 E + 01	4.534901 E + 00

9 (3*p*")	10 (3*d*")	11 (4*s*)
2.116759 E + 00	3.889212 E + 00	1.060109 E + 01
− 1.887026 E − 01	− 3.764039 E − 02	− 4.007654 E − 04
2.139620 E + 00	6.068395 E − 01	3.377457 E − 02

k	1 (**30 Zn**)	2 (2*p*')	3 (1*s*)	4 (3*p*')
R_k	1.093014 E − 04	6.639125 E − 02	7.523854 E − 02	1.278388 E − 01
ρ_k	5.484732 E + 12	− 1.127357 E + 03	− 1.152204 E + 03	− 3.116592 E + 01
φ_k	3.292847 E + 05	6.042967 E + 02	3.552648 E + 02	2.302047 E + 02

5 (2*p*")	6 (2*s*)	7 (3*d*')	8 (3*s*)
3.869566 E − 01	4.246594 E − 01	1.013522 E + 00	1.786819 E + 00
− 3.133533 E + 01	− 6.488273 E + 00	− 2.535231 E − 01	− 2.985017 E − 01
6.593855 E + 01	3.922154 E + 01	1.655417 E + 01	5.018828 E + 00

9 (3*p*")	10 (3*d*")	11 (4*s*)
2.037400 E + 00	3.782514 E + 00	1.045940 E + 01
− 2.148067 E − 01	− 4.539589 E − 02	− 4.172736 E − 04
2.411364 E + 00	6.624929 E − 01	3.470547 E − 02

k	1 (**31 Ga**)	2 (2*p*')	3 (1*s*)	4 (3*p*')	5 (2*p*")
R_k	9.999056 E − 05	6.354192 E − 02	7.266068 E − 02	1.183149 E − 01	3.703495 E − 01
ρ_k	7.402800 E + 12	− 1.251794 E + 03	− 1.280136 E + 03	− 3.549781 E + 01	− 3.571151 E + 01
φ_k	3.719511 E + 05	6.541462 E + 02	3.827763 E + 02	2.556463 E + 02	7.203164 E + 01

Copyright © 2010 SciRes.

6 (4*p*')	7 (2*s*)	8 (3*d*')	9 (3*s*)
4.000629 E − 01	4.075339 E − 01	8.207280 E − 01	1.677752 E + 00
− 7.369772 E + 00	− 7.369910 E + 00	− 3.156732 E − 01	− 4.003778 E − 01
4.294966 E + 01	4.044939 E + 01	2.158163 E + 01	5.860955 E + 00

10 (3*p*'')	11 (3*d*'')	12 (4*s*)	13 (4*p*'')
1.885615 E + 00	3.062999 E + 00	8.681390 E + 00	1.198854 E + 01
− 2.992761 E − 01	− 8.557296 E − 02	− 8.683064 E − 04	− 1.385572 E − 04
2.525737 E + 00	9.701396 E − 01	8.953004 E − 02	3.130941 E − 03

k	1 (**32 Ge**)	2 (2*p*')	3 (1*s*)	4 (3*p*')	5 (4*p*')
R_k	9.152975 E − 05	6.091629 E − 02	7.025164 E − 02	1.102557 E − 01	3.407788 E − 01
ρ_k	9.962644 E + 12	− 1.385189 E + 03	− 1.417356 E + 03	− 4.023520 E + 01	− 4.049928 E + 01
φ_k	4.194475 E + 05	7.062215 E + 02	4.114887 E + 02	2.818673 E + 02	8.232897 E + 01

6 (2*p*'')	7 (2*s*)	8 (3*d*')	9 (3*s*)
3.550461 E − 01	3.916665 E − 01	7.011994 E − 01	1.582128 E + 00
− 4.049972 E + 01	− 8.332968 E + 00	− 3.861721 E − 01	− 5.219974 E − 01
5.031343 E + 01	4.588502 E + 01	2.635623 E + 01	6.739995 E + 00

10 (3*p*'')	11 (3*d*'')	12 (4*s*)	13 (4*p*'')
1.757173 E + 00	2.616912 E + 00	7.604480 E + 00	1.021199 E + 01
− 4.014337 E − 01	− 1.373594 E − 01	− 1.534117 E − 03	− 4.483593 E − 04
2.784645 E + 00	1.339787 E + 00	1.525060 E − 01	6.312235 E − 03

k	1 (**33 As**)	2 (2*p*')	3 (1*s*)	4 (3*p*')	5 (4*p*')
R_k	8.390709 E − 05	5.848880 E − 02	6.799527 E − 02	1.032950 E − 01	3.005274 E − 01
ρ_k	1.333612 E + 13	− 1.527877 E + 03	− 1.564217 E + 03	− 4.540040 E + 01	− 4.572154 E + 01
φ_k	4.718582 E + 05	7.604931 E + 02	4.413606 E + 02	3.089537 E + 02	9.868202 E + 01

6 (2*p*'')	7 (2*s*)	8 (3*d*')	9 (3*s*)
3.408977 E − 01	3.769232 E − 01	6.168400 E − 01	1.497231 E + 00
− 4.572252 E + 01	− 9.382132 E + 00	− 4.658747 E − 01	− 6.653952 E − 01
5.747501 E + 01	4.960630 E + 01	3.109604 E + 01	7.683508 E + 00

10 (3*p*'')	11 (3*d*'')	12 (4*s*)	13 (4*p*'')
1.646238 E + 00	2.302078 E + 00	6.830392 E + 00	9.005793 E + 00
− 5.231378 E − 01	− 2.019994 E − 01	− 2.478899 E − 03	− 9.805796 E − 04
3.142610 E + 00	1.769067 E + 00	2.236234 E − 01	9.621769 E − 03

k	1 (**34 Se**)	2 (2*p*')	3 (1*s*)	4 (3*p*')	5 (4*p*')
R_k	7.701127 E − 05	5.622750 E − 02	6.587597 E − 02	9.705244 E − 02	2.878107 E − 01
ρ_k	1.777164 E + 13	− 1.680309 E + 03	− 1.721213 E + 03	− 5.104387 E + 01	− 5.143105 E + 01
φ_k	5.296960 E + 05	8.171156 E + 02	4.724217 E + 02	3.373356 E + 02	1.075189 E + 02

6 (2*p*")	7 (2*s*)	8 (3*d*')	9 (3*s*)
3.277179 E − 01	3.631299 E − 01	5.508007 E − 01	1.419578 E + 00
− 5.143254 E + 01	− 1.052897 E + 01	− 5.575898 E − 01	− 8.378243 E − 01
6.232486 E + 01	5.356944 E + 01	3.603637 E + 01	8.745636 E + 00

10 (3*p*")	11 (3*d*")	12 (4*s*)	13 (4*p*")
1.546749 E + 00	2.055616 E + 00	6.181776 E + 00	8.624716 E + 00
− 6.709217 E − 01	− 2.837442 E − 01	− 3.509678 E − 03	− 1.488515 E − 03
3.616572 E + 00	2.303229 E + 00	3.376347 E − 01	1.833763 E − 02

k	1 (**35 Br**)	2 (2*p*')	3 (1*s*)	4 (3*p*')	5 (4*p*')
R_k	7.079964 E − 05	5.413089 E − 02	6.388372 E − 02	9.159978 E − 02	2.701979 E − 01
ρ_k	2.354433 E + 13	− 1.842653 E + 03	− 1.888496 E + 03	− 5.714848 E + 01	− 5.760900 E + 01
φ_k	5.931226 E + 05	8.758716 E + 02	5.046158 E + 02	3.665159 E + 02	1.196651 E + 02

6 (2*p*")	7 (2*s*)	8 (3*d*')	9 (3*s*)
3.154980 E − 01	3.502848 E − 01	4.996283 E − 01	1.350318 E + 00
− 5.761125 E + 01	− 1.176836 E + 01	− 6.593011 E − 01	− 1.034761 E + 00
6.833061 E + 01	5.776175 E + 01	4.103985 E + 01	9.882824 E + 00

10 (3*p*")	11 (3*d*")	12 (4*s*)	13 (4*p*")
1.459849 E + 00	1.864638 E + 00	5.676813 E + 00	8.096922 E + 00
− 8.408365 E − 01	− 3.803189 E − 01	− 4.858655 E − 03	− 2.248732 E − 03
4.163553 E + 00	2.892445 E + 00	4.591730 E − 01	2.713501 E − 02

k	1 (**36 Kr**)	2 (2*p*')	3 (1*s*)	4 (3*p*')	5 (4*p*')
R_k	6.520398 E − 05	5.218195 E − 02	6.200750 E − 02	8.678239 E − 02	2.523121 E − 01
ρ_k	3.100213 E + 13	− 2.015226 E + 03	− 2.066399 E + 03	− 6.373287 E + 01	− 6.427441 E + 01
φ_k	6.624313 E + 05	9.367502 E + 02	5.379329 E + 02	3.965350 E + 02	1.337821 E + 02

6 (2*p*")	7 (2*s*)	8 (3*d*')	9 (3*s*)
3.041387 E − 01	3.382960 E − 01	4.584139 E − 01	1.288048 E + 00
− 6.427773 E + 01	− 1.310405 E + 01	− 7.715564 E − 01	− 1.257663 E + 00
7.503190 E + 01	6.217318 E + 01	4.615233 E + 01	1.109493 E + 01

10 (3*p*")	11 (3*d*")	12 (4*s*)	13 (4*p*")
1.383073 E + 00	1.710824 E + 00	5.268325 E + 00	7.560943 E + 00
− 1.034231 E + 00	− 4.926861 E − 01	− 6.579293 E − 03	− 3.313988 E − 03
4.773982 E + 00	3.534833 E + 00	5.868131 E − 01	3.586672 E − 02

k	1 (**37 Rb**)	2 (2*p*')	3 (1*s*)	4 (3*p*')	5 (4*p*')
R_k	6.070802 E − 05	5.026544 E − 02	6.022254 E − 02	8.132292 E − 02	2.029644 E − 01
ρ_k	3.947980 E + 13	− 2.200059 E + 03	− 2.257313 E + 03	− 7.124147 E + 01	− 7.189957 E + 01
φ_k	7.312598 E + 05	1.001329 E + 03	5.724190 E + 02	4.312196 E + 02	1.753015 E + 02

Copyright © 2010 SciRes.

6 (2*p*")	7 (2*s*)	8 (3*d*')	9 (3*s*)	10 (3*p*")
2.929685E − 01	3.264912 E − 01	4.121461 E − 01	1.218004 E + 00	1.296064 E + 00
− 7.190594E + 01	− 1.465283 E + 01	− 9.336976 E − 01	− 1.602583 E + 00	− 1.338345 E + 00
8.859241E + 01	6.646259 E + 01	5.220725 E + 01	1.238409 E + 01	5.373080 E + 00

11 (3*d*")	12 (4*s*)	13 (4*p*")	14 (5*s*)
1.538150 E + 00	4.582967 E + 00	6.082158 E + 00	1.904387 E + 01
− 6.802465 E − 01	− 1.136136 E − 02	− 6.401139 E − 03	− 3.456575 E − 05
4.252708 E + 00	8.138172 E − 01	1.393163 E − 01	1.057707 E − 02

k	1 (**38 Sr**)	2 (2*p*')	3 (1*s*)	4 (3*p*')	5 (4*p*')
R_k	5.649045 E − 05	4.848135 E − 02	5.853622 E − 02	7.657762 E − 02	1.743202 E − 01
ρ_k	5.032339 E + 13	− 2.396022 E + 03	− 2.459831 E + 03	− 7.933502 E + 01	− 8.012319 E + 01
φ_k	8.071016 E + 05	1.068257 E + 03	6.081450 E + 02	4.667447 E + 02	2.124328 E + 02

6 (2*p*")	7 (2*s*)	8 (3*d*')	9 (3*s*)	10 (3*p*")
2.825700 E − 01	3.154582 E − 01	3.757189 E − 01	1.155770 E + 00	1.220437 E + 00
− 8.013324 E + 01	− 1.632401 E + 01	− 1.114481 E + 00	− 1.997390 E + 00	− 1.688127 E + 00
1.001483 E + 02	7.106794 E + 01	5.837499 E + 01	1.384092 E + 01	6.125594 E + 00

11 (3*d*")	12 (4*s*)	13 (4*p*")	14 (5*s*)
1.402202 E + 00	4.107361 E + 00	5.223789 E + 00	1.673859 E + 01
− 8.999501 E − 01	− 1.704132 E − 02	− 1.015079 E − 02	− 1.018086 E − 04
5.104113 E + 00	1.102047 E + 00	2.781945 E − 01	2.447504 E − 02

k	1 (**39 Y**)	2 (2*p*')	3 (1*s*)	4 (3*p*')
R_k	5.236921 E − 05	4.685108 E − 02	5.694566 E − 02	7.275406 E − 02
ρ_k	6.482580 E + 13	− 2.602725 E + 03	− 2.673430 E + 03	− 8.784124 E + 01
φ_k	8.935358 E + 05	1.136812 E + 03	6.450321 E + 02	5.017009 E + 02

5 (4*p*')	6 (2*p*")	7 (2*s*)	8 (3*d*')
1.601441 E − 01	2.730681 E − 01	3.053329 E − 01	3.490053 E − 01
− 8.876033 E + 01	− 8.877329 E + 01	− 1.806852 E + 01	− 1.295142 E + 00
2.395223 E + 02	1.095471 E + 02	7.606533 E + 01	6.442781 E + 01

9 (3*s*)	10 (3*p*")	11 (3*d*")	12 (4*d*')
1.104356 E + 00	1.159500 E + 00	1.302505 E + 00	1.337515 E + 00
− 2.396705 E + 00	− 2.042206 E + 00	− 1.123117 E + 00	− 2.155444 E − 02
1.542110 E + 01	7.004576 E + 00	6.043694 E + 00	5.413486 E + 00

13 (4*s*)	14 (4*p*")	15 (4*d*")	16 (5*s*)
3.841116 E + 00	4.798980 E + 00	1.143536 E + 01	1.414640 E + 01
− 2.171434 E − 02	− 1.328936 E − 02	− 3.285598 E − 04	− 1.686566 E − 04
1.360085 E + 00	3.863704 E − 01	6.436441 E − 02	2.580686 E − 03

k	1 (**40 Zr**)	2 (2p')	3 (1s)	4 (3p')
R_k	4.854586 E − 05	4.533534 E − 02	5.543996 E − 02	6.942112 E − 02
ρ_k	8.346702 E + 13	− 2.820873 E + 03	− 2.898909 E + 03	− 9.688049 E + 01
φ_k	9.886325 E + 05	1.207368 E + 03	6.830739 E + 02	5.371539 E + 02

5 (4p')	6 (2p'')	7 (2s)	8 (3d')
1.497748 E − 01	2.642337 E − 01	2.958863 E − 01	3.270379 E − 01
− 9.793841 E + 01	− 9.795425 E + 01	− 1.991792 E + 01	− 1.486163 E + 00
2.648215 E + 02	1.187383 E + 02	8.135216 E + 01	7.060441 E + 01

9 (3s)	10 (3p'')	11 (3d'')	12 (4d')
1.058841 E + 00	1.106382 E + 00	1.220522 E + 00	1.301045 E + 00
− 2.824948 E + 00	− 2.422741 E + 00	− 1.364817 E + 00	− 2.603216 E − 02
1.711908 E + 01	7.983580 E + 00	7.073825 E + 00	6.258831 E + 00

13 (4s)	14 (4p'')	15 (4d'')	16 (5s)
3.636969 E + 00	4.488245 E + 00	1.112355 E + 01	1.218499 E + 01
− 2.637962 E − 02	− 1.645480 E − 02	− 6.113773 E − 04	− 2.639161 E − 04
1.634497 E + 00	5.108769 E − 01	6.803978 E − 02	6.220605 E − 04

k	1 (**41 Nb**)	2 (2p')	3 (1s)	4 (3p')
R_k	4.501991 E − 05	4.391736 E − 02	5.401178 E − 02	6.643865 E − 02
ρ_k	1.072707 E + 14	− 3.050890 E + 03	− 3.136732 E + 03	− 1.064995 E + 02
φ_k	1.092722 E + 06	1.280030 E + 03	7.222732 E + 02	5.733900 E + 02

5 (4p')	6 (2p'')	7 (2s)	8 (3d')
1.412630 E − 01	2.559691 E − 01	2.870219 E − 01	3.082248 E − 01
− 1.077064 E + 02	− 1.077253 E + 02	− 2.188346 E + 01	− 1.690672 E + 00
2.899560 E + 02	1.280690 E + 02	8.690561 E + 01	7.697269 E + 01

9 (3s)	10 (3p'')	11 (3d'')	12 (4d')
1.017632 E + 00	1.058850 E + 00	1.150311 E + 00	1.272790 E + 00
− 3.289871 E + 00	− 2.836797 E + 00	− 1.629909 E + 00	− 3.070995 E − 02
1.893695 E + 01	9.059018 E + 00	8.198586 E + 00	7.145154 E + 00

13 (4s)	14 (4p'')	15 (4d'')	16 (5s)
3.464973 E + 00	4.233175 E + 00	1.088198 E + 01	1.109917 E + 01
− 3.126663 E − 02	− 1.978928 E − 02	− 9.058751 E − 04	− 3.491964 E − 04
1.940829 E + 00	6.632702 E − 01	7.957632 E − 02	3.449854 E − 05

k	1 (**42 Mo**)	2 (2p')	3 (1s)	4 (3p')
R_k	4.178552 E − 05	4.258720 E − 02	5.265520 E − 02	6.374337 E − 02
ρ_k	1.374305 E + 14	− 3.293107 E + 03	− 3.387246 E + 03	− 1.167202 E + 02
φ_k	1.206027 E + 06	1.354802 E + 03	7.626188 E + 02	6.104650 E + 02

Copyright © 2010 SciRes.

5 (4*p*')	6 (2*p*")	7 (2*s*)	8 (3*d*')
1.340394 E − 01	2.482164 E − 01	2.786829 E − 01	2.918330 E − 01
− 1.180867 E + 02	− 1.181088 E + 02	− 2.396970 E + 01	− 1.909450 E + 00
3.152121 E + 02	1.376027 E + 02	9.271058 E + 01	8.354308 E + 01

9 (3*s*)	10 (3*p*")	11 (3*d*")	12 (4*d*')
9.800179 E − 01	1.015894 E + 00	1.089135 E + 00	1.249745 E + 00
− 3.793542 E + 00	− 3.286271 E + 00	− 1.919725 E + 00	− 3.563374 E − 02
2.086513 E + 01	1.021983 E + 01	9.409282 E + 00	8.064772 E + 00

13 (4*s*)	14 (4*p*")	15 (5*s*)	16 (4*d*")
3.316004 E + 00	4.016708 E + 00	1.031409 E + 01	1.068495 E + 01
− 3.641780 E − 02	− 2.332308 E − 02	− 1.219220 E − 03	− 7.840598 E − 04
2.272332 E + 00	8.374436 E − 01	1.059247 E − 01	2.258214 E − 04

k	1 (**43 Tc**)	2 (2*p*')	3 (1*s*)	4 (3*p*')
R_k	3.882324 E − 05	4.133751 E − 02	5.136509 E − 02	6.129718 E − 02
ρ_k	1.754303 E + 14	− 3.547815 E + 03	− 3.650753 E + 03	− 1.275539 E + 02
φ_k	1.328965 E + 06	1.431661 E + 03	8.041074 E + 02	6.483741 E + 02

5 (4*p*')	6 (2*p*")	7 (2*s*)	8 (3*d*')
1.278604 E − 01	2.409326 E − 01	2.708275 E − 01	2.774215 E − 01
− 1.290906 E + 02	− 1.291161 E + 02	− 2.617834 E + 01	− 2.142288 E + 00
3.405277 E + 02	1.473462 E + 02	9.876592 E + 01	9.031936 E + 01

9 (3*s*)	10 (3*p*")	11 (3*d*")	12 (4*d*')
9.455719 E − 01	9.769087 E − 01	1.035351 E + 00	1.231746 E + 00
− 4.335521 E + 00	− 3.770769 E + 00	− 2.234002 E + 00	− 4.076921 E − 02
2.289872 E + 01	1.146057 E + 01	1.070110 E + 01	9.005113 E + 00

13 (4*s*)	14 (4*p*")	15 (5*s*)	16 (4*d*")
3.186168 E + 00	3.831546 E + 00	9.587477 E + 00	1.053106 E + 01
− 4.179288 E − 02	− 2.703122 E − 02	− 1.565457 E − 03	− 1.023670 E − 03
2.622872 E + 00	1.028803 E + 00	1.492681 E − 01	2.032708 E − 03

k	1 (**44 Ru**)	2 (2*p*')	3 (1*s*)	4 (3*p*')
R_k	3.611369 E − 05	4.015578 E − 02	5.013584 E − 02	5.902079 E − 02
ρ_k	2.230224 E + 14	− 3.815532 E + 03	− 3.927828 E + 03	− 1.390723 E + 02
φ_k	1.461909 E + 06	1.510763 E + 03	8.467422 E + 02	6.874083 E + 02

5 (4*p*')	6 (2*p*")	7 (2*s*)	8 (3*d*')
1.220143 E − 01	2.340450 E − 01	2.633820 E − 01	2.643215 E − 01
− 1.407939 E + 02	− 1.408232 E + 02	− 2.852738 E + 01	− 2.394761 E + 00
3.673248 E + 02	1.575063 E + 02	1.050439 E + 02	9.734860 E + 01

Copyright © 2010 SciRes.

9 (3*s*)	10 (3*p*")	11 (3*d*")	12 (4*d*')
9.133153 E − 01	9.406294 E − 01	9.864613 E − 01	1.209399 E + 00
− 4.930517 E + 00	− 4.303789 E + 00	− 2.582260 E + 00	− 4.650346 E − 02
2.504522 E + 01	1.278456 E + 01	1.208312 E + 01	1.002162 E + 01

13 (4*s*)	14 (4*p*")	15 (5*s*)	16 (4*d*")
3.062729 E + 00	3.656358 E + 00	9.373947 E + 00	1.034000 E + 01
− 4.780123 E − 02	− 3.118181 E − 02	− 1.877428 E − 03	− 1.297767 E − 03
3.014346 E + 00	1.252608 E + 00	1.818008 E − 01	2.533380 E − 03

k	1 (**45 Rh**)	2 (2*p*')	3 (1*s*)	4 (3*p*')
R_k	3.363296 E − 05	3.904164 E − 02	4.896407 E − 02	5.693585 E − 02
ρ_k	2.823766 E + 14	− 4.096380 E + 03	− 4.218567 E + 03	− 1.512420 E + 02
φ_k	1.605423 E + 06	1.591948 E + 03	8.905132 E + 02	7.273057 E + 02

5 (4*p*')	6 (2*p*")	7 (3*d*')	8 (2*s*)
1.169241 E − 01	2.275514 E − 01	2.526218 E − 01	2.563458 E − 01
− 1.531597 E + 02	− 1.531930 E + 02	− 3.100646 E + 01	− 3.391110 E + 01
3.942567 E + 02	1.678941 E + 02	1.127274 E + 02	1.045915 E + 02

9 (3*s*)	10 (3*p*")	11 (3*d*")	12 (4*d*')
8.835513 E − 01	9.074011 E − 01	9.427974 E − 01	1.191622 E + 00
− 5.567006 E + 00	− 4.874783 E + 00	− 2.957121 E + 00	− 5.247938 E − 02
2.720889 E + 01	1.418261 E + 01	1.354179 E + 01	1.105142 E + 01

13 (4*s*)	14 (4*p*")	15 (5*s*)	16 (4*d*")
2.953454 E + 00	3.503823 E + 00	9.043605 E + 00	1.018801 E + 01
− 5.406222 E − 02	− 3.552900 E − 02	− 2.228368 E − 03	− 1.582837 E − 03
3.420811 E + 00	1.490568 E + 00	2.257527 E − 01	4.333491 E − 03

k	1 (**46 Pd**)	2 (2*p*')	3 (1*s*)	4 (3*p*')
R_k	3.135993 E − 05	3.798848 E − 02	4.784571 E − 02	5.501025 E − 02
ρ_k	3.560771 E + 14	− 4.390715 E + 03	− 4.523348 E + 03	− 1.640911 E + 02
φ_k	1.760059 E + 06	1.675240 E + 03	9.354178 E + 02	7.681297 E + 02

5 (4*p*')	6 (2*p*")	7 (3*d*')	8 (2*s*)
1.123683 E − 01	2.214131 E − 01	2.420456 E − 01	2.496803 E − 01
− 1.662173 E + 02	− 1.662548 E + 02	− 3.362176 E + 01	− 3.692404 E + 01
4.216182 E + 02	1.785547 E + 02	1.209265 E + 02	1.120601 E + 02

9 (3*s*)	10 (3*p*")	11 (3*d*")	12 (4*d*')
8.558870 E − 01	8.767124 E − 01	9.033265 E − 01	1.176168 E + 00
− 6.248755 E + 00	− 5.487216 E + 00	− 3.361044 E + 00	− 5.876710 E − 02
2.945320 E + 01	1.565481 E + 01	1.507872 E + 01	1.210346 E + 01

Copyright © 2010 SciRes.

13 (4*s*)	14 (4*p*")	15 (5*s*)	16 (4*d*")
2.854421 E + 00	3.367301 E + 00	8.721407 E + 00	1.005589 E + 01
− 6.064830 E − 02	− 4.011839 E − 02	− 2.600952 E − 03	− 1.881202 E − 03
3.846500 E + 00	1.746075 E + 00	2.771911 E − 01	6.997619 E − 03

k	1 (**47 Ag**)	2 (2*p*')	3 (1*s*)	4 (3*p*')
R_k	2.952782 E − 05	3.699131 E − 02	4.677718 E − 02	5.322435 E − 02
ρ_k	4.358279 E + 14	− 4.698854 E + 03	− 4.842505 E + 03	− 1.776379 E + 02
φ_k	1.909909 E + 06	1.759912 E + 03	9.807244 E + 02	8.091657 E + 02

5 (4*p*')	6 (2*p*")	7 (3*d*')	8 (2*s*)
1.082510 E − 01	2.156012 E − 01	2.324222 E − 01	2.433561 E − 01
− 1.799854 E + 02	− 1.800274 E + 02	− 3.637649 E + 01	− 4.010617 E + 01
4.487302 E + 02	1.887680 E + 02	1.286466 E + 02	1.190270 E + 02

9 (4*d*')	10 (3*s*)	11 (3*p*")	12 (3*d*")
7.049601 E − 01	8.300820 E − 01	8.482500 E − 01	8.674116 E − 01
− 6.976692 E + 00	− 6.986521 E + 00	− 6.151728 E + 00	− 3.804267 E + 00
3.908188 E + 01	1.891337 E + 01	1.646990 E + 01	1.596332 E + 01

13 (4*s*)	14 (4*p*")	15 (4*d*")	16 (5*s*)
2.763928 E + 00	3.243917 E + 00	6.027200 E + 00	1.387693 E + 01
− 7.458398 E − 02	− 5.197082 E − 02	− 1.000752 E − 02	− 1.786739 E − 04
4.016741 E + 00	1.410594 E + 00	3.639316 E − 01	2.123996 E − 02

k	1 (**48 Cd**)	2 (2*p*')	3 (1*s*)	4 (3*p*')
R_k	2.764401 E − 05	3.604624 E − 02	4.575532 E − 02	5.156591 E − 02
ρ_k	5.424374 E + 14	− 5.022756 E + 03	− 5.176336 E + 03	− 1.918938 E + 02
φ_k	2.083482 E + 06	1.853729 E + 03	1.034221 E + 03	8.581836 E + 02

5 (4*p*')	6 (2*p*")	7 (3*d*')	8 (2*s*)
1.045398 E − 01	2.100929 E − 01	2.236414 E − 01	2.373506 E − 01
− 1.944751 E + 02	− 1.945217 E + 02	− 3.927316 E + 01	− 4.345964 E + 01
4.832583 E + 02	2.063170 E + 02	1.436819 E + 02	1.332878 E + 02

9 (4*d*')	10 (3*s*)	11 (3*p*")	12 (3*d*")
6.778536 E − 01	8.059884 E − 01	8.218190 E − 01	8.346412 E − 01
− 5.182215 E + 00	− 7.763532 E + 00	− 6.851616 E + 00	− 4.270299 E + 00
4.795679 E + 01	2.494971 E + 01	2.186001 E + 01	2.135897 E + 01

13 (4*s*)	14 (4*p*")	15 (4*d*")	16 (5*s*)
2.681445 E + 00	3.132706 E + 00	5.795447 E + 00	1.373979 E + 01
− 8.382595 E − 02	− 5.906115 E − 02	− 1.246825 E − 02	− 1.840775 E − 04
6.073621 E + 00	2.658194 E + 00	1.097410 E + 00	3.335212 E − 01

Copyright © 2010 SciRes.

k	1 (**49 In**)	2 (2p')	3 (1s)	4 (3p')	5 (4p')
R_k	2.611485 E − 05	3.511143 E − 02	4.477062 E − 02	4.972748 E − 02	9.754386 E − 02
ρ_k	6.568177 E + 14	− 5.360185 E + 03	− 5.528167 E + 03	− 2.075506 E + 02	− 2.104289 E + 02
φ_k	2.251429 E + 06	1.938178 E + 03	1.075775 E + 03	8.976829 E + 02	5.220315 E + 02

6 (2p")	7 (3d')	8 (2s)	9 (5p')	10 (4d')
2.046444 E − 01	2.137762 E − 01	2.314069 E − 01	3.250338 E − 01	5.745003 E − 01
− 2.104863 E + 02	− 4.250458 E + 01	− 4.729780 E + 01	− 8.766608 E + 00	− 8.766671 E + 00
2.130830 E + 02	1.462519 E + 02	1.349310 E + 02	9.904672 E + 01	4.714387 E + 01

11 (3s)	12 (3p")	13 (3d")	14 (4s)
7.794883 E − 01	7.925194 E − 01	7.978237 E − 01	2.535737 E + 00
− 8.786849 E + 00	− 7.778728 E + 00	− 4.900401 E + 00	− 1.071865 E − 01
2.418580 E + 01	1.920578 E + 01	1.889586 E + 01	4.776507 E + 00

15 (4p")	16 (4d")	17 (5s)	18 (5p")
2.923061 E + 00	4.911808 E + 00	1.158315 E + 01	1.559485 E + 01
− 7.790259 E − 02	− 2.054839 E − 02	− 3.701749 E − 04	− 6.294652 E − 05
1.688160 E + 00	5.692079 E − 01	5.639479 E − 02	2.097238 E − 03

k	1 (**50 Sn**)	2 (2p')	3 (1s)	4 (3p')	5 (4p')
R_k	2.467213 E − 05	3.422326 E − 02	4.382713 E − 02	4.802160 E − 02	9.169330 E − 02
ρ_k	7.948065 E + 14	− 5.714333 E + 03	− 5.895736 E + 03	− 2.240491 E + 02	− 2.272451 E + 02
φ_k	2.431725 E + 06	2.031427 E + 03	1.125036 E + 03	9.447684 E + 02	5.671729 E + 02

6 (2p")	7 (3d')	8 (2s)	9 (5p')	10 (4d')
1.994678 E − 01	2.048100 E − 01	2.257492 E − 01	2.804256 E − 01	5.062632 E − 01
− 2.273142 E + 02	− 4.591169 E + 01	− 5.136238 E + 01	− 9.860977 E + 00	− 9.861173 E + 00
2.264465 E + 02	1.556454 E + 02	1.433694 E + 02	1.153567 E + 02	5.888310 E + 01

11 (3s)	12 (3d")	13 (3p")	14 (4s)
7.547442 E − 01	7.643613 E − 01	7.653325 E − 01	2.409355 E + 00
− 9.890659 E + 00	− 8.780099 E + 00	− 3.329406 E + 00	− 1.333130 E − 01
2.747505 E + 01	2.064088 E + 01	2.044099 E + 01	5.225673 E + 00

15 (4p")	16 (4d")	17 (5s)	18 (5p")
2.747739 E + 00	4.328401 E + 00	1.024433 E + 01	1.345458 E + 01
− 9.917492 E − 02	− 3.012673 E − 02	− 6.401462 E − 04	− 1.960355 E − 04
1.880047 E + 00	7.646722 E − 01	9.464658 E − 02	4.190133 E − 03

k	1 (**51 Sb**)	2 (2p')	3 (1s)	4 (3p')	5 (4p')
R_k	2.332088 E − 05	3.337787 E − 02	4.292223 E − 02	4.643023 E − 02	8.664807 E − 02
ρ_k	9.599455 E + 14	− 6.083905 E + 03	− 6.279443 E + 03	− 2.414227 E + 02	− 2.449588 E + 02
φ_k	2.624084 E + 06	2.126981 E + 03	1.175481 E + 03	9.929617 E + 02	6.127320 E + 02

Copyright © 2010 SciRes.

6 (2*p*")	7 (3*d*')	8 (2*s*)	9 (5*p*')	10 (4*d*')
1.945405 E − 01	1.965963 E − 01	2.203544 E − 01	2.495391 E − 01	4.559489 E − 01
− 2.450406 E + 02	− 4.950237 E + 01	− 5.566519 E + 01	− 1.104041 E + 01	− 1.104083 E + 01
2.399941 E + 02	1.653418 E + 02	1.520799 E + 02	1.300246 E + 02	7.044826 E + 01

11 (3*s*)	12 (3*d*")	13 (3*p*")	14 (4*s*)
7.315308 E − 01	7.337072 E − 01	7.399704 E − 01	2.297336 E + 00
− 1.108120 E + 01	− 9.861523 E + 00	− 3.698705 E + 00	− 1.625863 E − 01
3.066017 E + 01	2.227480 E + 01	2.209584 E + 01	5.720609 E + 00

15 (4*p*")	16 (4*d*")	17 (5*s*)	18 (5*p*")
2.596551 E + 00	3.898228 E + 00	9.270607 E + 00	1.197267 E + 01
− 1.232070 E − 01	− 4.138160 E − 02	− 1.016576 E − 03	− 4.173142 E − 04
2.112967 E + 00	9.840578 E − 01	1.370464 E − 01	6.326601 E − 03

k	1 (**52 Te**)	2 (2*p*')	3 (1*s*)	4 (3*p*')	5 (4*p*')
R_k	2.205345 E − 05	3.257040 E − 02	4.205326 E − 02	4.492876 E − 02	8.208538 E − 02
ρ_k	1.157405 E + 15	− 6.469406 E + 03	− 6.679851 E + 03	− 2.597405 E + 02	− 2.636431 E + 02
φ_k	2.829311 E + 06	2.224939 E + 03	1.227111 E + 03	1.042414 E + 03	6.598953 E + 02

6 (3*d*')	7 (2*p*")	8 (2*s*)	9 (5*p*')	10 (4*d*')
1.889628 E − 01	1.898342 E − 01	2.151935 E − 01	2.406710 E − 01	4.149085 E − 01
− 2.637394 E + 02	− 2.776199 E + 02	− 6.023488 E + 01	− 1.232182 E + 01	− 1.232244 E + 01
2.550619 E + 02	1.753634 E + 02	1.606489 E + 02	1.377109 E + 02	8.029383 E + 01

11 (3*d*")	12 (3*s*)	13 (3*p*")	14 (4*s*)
7.052189 E − 01	7.095263 E − 01	7.160411 E − 01	2.194126 E + 00
− 1.237601 E + 01	− 5.435748 E + 00	− 4.099042 E + 00	− 1.964236 E − 01
3.412204 E + 01	2.401900 E + 01	2.376272 E + 01	6.286788 E + 00

15 (4*p*")	16 (4*d*")	17 (5*s*)	18 (5*p*")
2.459822 E + 00	3.547345 E + 00	8.448161 E + 00	1.154719 E + 01
− 1.512217 E − 01	− 5.497902 E − 02	− 1.412092 E − 03	− 6.202203 E − 04
2.405228 E + 00	1.258944 E + 00	2.074935 E − 01	1.204640 E − 02

k	1 (**53 I**)	2 (2*p*')	3 (1*s*)	4 (3*p*')	5 (4*p*')
R_k	2.086803 E − 05	3.180051 E − 02	4.121852 E − 02	4.352442 E − 02	7.808259 E − 02
ρ_k	1.392332 E + 15	− 6.870988 E + 03	− 7.097090 E + 03	− 2.789775 E + 02	− 2.832702 E + 02
φ_k	3.047541 E + 06	2.325207 E + 03	1.279941 E + 03	1.092975 E + 03	7.075875 E + 02

6 (3*d*')	7 (2*p*")	8 (2*s*)	9 (5*p*')	10 (4*d*')
1.819331 E − 01	1.853470 E − 01	2.102648 E − 01	2.273653 E − 01	3.822704 E − 01
− 2.833820 E + 02	− 2.911583 E + 02	− 6.505592 E + 01	− 1.369398 E + 01	− 1.369489 E + 01
2.731331 E + 02	1.857106 E + 02	1.685551 E + 02	1.479557 E + 02	9.094124 E + 01

Copyright © 2010 SciRes.

11 ($3d''$)	12 ($3s$)	13 ($3p''$)	14 ($4s$)
6.789834 E − 01	6.888415 E − 01	6.936597 E − 01	2.101721 E + 00
− 1.376339 E + 01	− 5.987138 E + 00	− 4.526363 E + 00	− 2.336622 E − 01
3.772690 E + 01	2.586681 E + 01	2.548103 E + 01	6.899952 E + 00

15 ($4p''$)	16 ($4d''$)	17 ($5s$)	18 ($5p''$)
2.339872 E + 00	3.268298 E + 00	7.803381 E + 00	1.090880 E + 01
− 1.822322 E − 01	− 7.041664 E − 02	− 1.924337 E − 03	− 9.195065 E − 04
2.730047 E + 00	1.556790 E + 00	2.824270 E − 01	1.830144 E − 02

k	1 (**54 Xe**)	2 ($2p'$)	3 ($1s$)	4 ($3p'$)	5 ($4p'$)
R_k	1.976032 E − 05	3.106561 E − 02	4.041604 E − 02	4.220737 E − 02	7.452533 E − 02
ρ_k	1.670796 E + 15	− 7.288990 E + 03	− 7.531521 E + 03	− 2.991585 E + 02	− 3.038657 E + 02
φ_k	3.279111 E + 06	2.427739 E + 03	1.333923 E + 03	1.144606 E + 03	7.559227 E + 02

6 ($3d'$)	7 ($2p''$)	8 ($2s$)	9 ($5p'$)	10 ($4d'$)
1.754323 E − 01	1.810636 E − 01	2.055529 E − 01	2.134902 E − 01	3.554090 E − 01
− 3.039943 E + 02	− 3.126674 E + 02	− 7.013605 E + 01	− 1.516040 E + 01	− 1.516174 E + 01
2.916489 E + 02	1.963378 E + 02	1.766887 E + 02	1.594076 E + 02	1.021463 E + 02

11 ($3d''$)	12 ($3s$)	13 ($3p''$)	14 ($4s$)
6.547224 E − 01	6.693523 E − 01	6.726696 E − 01	2.018208 E + 00
− 1.524696 E + 01	− 6.573828 E + 00	− 4.981703 E + 00	− 2.744835 E − 01
4.139147 E + 01	2.780050 E + 01	2.727882 E + 01	7.550129 E + 00

15 ($4p''$)	16 ($4d''$)	17 ($5s$)	18 ($5p''$)
2.233273 E + 00	3.038641 E + 00	7.276186 E + 00	1.024308 E + 01
− 2.164013 E − 01	− 8.779759 E − 02	− 2.572283 E − 03	− 1.332830 E − 03
3.079605 E + 00	1.873818 E + 00	3.598366 E − 01	2.419956 E − 02

k	1 (**55 Cs**)	2 ($2p'$)	3 ($1s$)	4 ($3p'$)	5 ($4p'$)
R_k	1.882567 E − 05	3.034583 E − 02	3.964060 E − 02	4.085289 E − 02	7.021561 E − 02
ρ_k	1.967990 E + 15	− 7.725818 E + 03	− 7.986020 E + 03	− 3.208696 E + 02	− 3.260607 E + 02
φ_k	3.505658 E + 06	2.533596 E + 03	1.388984 E + 03	1.198794 E + 03	8.156654 E + 02

6 ($3d'$)	7 ($5p'$)	8 ($2p''$)	9 ($2s$)	10 ($4d'$)
1.687565 E − 01	1.746273 E − 01	1.768685 E − 01	2.009346 E − 01	3.222227 E − 01
− 3.262145 E + 02	− 3.359582 E + 02	− 3.359606 E + 02	− 7.575875 E + 01	− 1.690460 E + 01
3.125647 E + 02	2.091124 E + 02	2.029666 E + 02	1.847288 E + 02	1.168266 E + 02

11 ($3d''$)	12 ($3s$)	13 ($3p''$)	14 ($4s$)	15 ($4p''$)
6.298078 E − 01	6.493185 E − 01	6.510829 E − 01	1.918350 E + 00	2.104125 E + 00
− 1.701896 E + 01	− 7.275268 E + 00	− 5.531181 E + 00	− 3.400614 E − 01	− 2.724285 E − 01
4.560922 E + 01	2.963468 E + 01	2.894976 E + 01	8.178919 E + 00	3.407417 E + 00

Copyright © 2010 SciRes.

16 (4*d*")	17 (5*s*)	18 (5*p*")	19 (6*s*)
2.754908 E + 00	6.371605 E + 00	8.378469 E + 00	2.412889 E + 01
− 1.186612 E − 01	− 4.298250 E − 03	− 2.452407 E − 03	− 1.699414 E − 05
2.230443 E + 00	5.019411 E − 01	9.493183 E − 02	7.804349 E − 03

k	1 (**56 Ba**)	2 (2*p*')	3 (1*s*)	4 (3*p*')	5 (4*p*')
R_k	1.792580 E − 05	2.965819 E − 02	3.889412 E − 02	3.958653 E − 02	6.648555 E − 02
ρ_k	2.320937 E + 15	− 8.179920 E + 03	− 8.458643 E + 03	− 3.436230 E + 02	− 3.493284 E + 02
φ_k	3.748586 E + 06	2.641857 E + 03	1.445293 E + 03	1.254123 E + 03	8.757556 E + 02

6 (5*p*')	7 (3*d*')	8 (2*p*")	9 (2*s*)	10 (4*d*')
1.518527 E − 01	1.626049 E − 01	1.728606 E − 01	1.965160 E − 01	2.961243 E − 01
− 3.495095 E + 02	− 3.495132 E + 02	− 3.604051 E + 02	− 8.168176 E + 01	− 1.876769 E + 01
3.578978 E + 02	2.377281 E + 02	2.187389 E + 02	1.930848 E + 02	1.294398 E + 02

11 (3*d*")	12 (3*s*)	13 (3*p*")	14 (4*s*)	15 (4*p*")
6.068497 E − 01	6.304911 E − 01	6.309005 E − 01	1.829902 E + 00	1.992348 E + 00
− 1.891503 E + 01	− 8.023115 E + 00	− 6.118073 E + 00	− 4.126575 E − 01	− 3.347359 E − 01
4.988457 E + 01	3.163095 E + 01	3.077654 E + 01	8.913591 E + 00	3.824103 E + 00

16 (4*d*")	17 (5*s*)	18 (5*p*")	19 (6*s*)
2.531775 E + 00	5.749176 E + 00	7.285766 E + 00	2.137902 E + 01
− 1.536089 E − 01	− 6.265215 E − 03	− 3.752607 E − 03	− 4.886279 E − 05
2.660332 E + 00	6.818691 E − 01	1.877558 E − 01	1.790125 E − 02

k	1 (**57 La**)	2 (2*p*')	3 (1*s*)	4 (3*p*')	5 (4*p*')
R_k	1.692451 E − 05	2.902829 E − 02	3.818004 E − 02	3.859718 E − 02	6.475144 E − 02
ρ_k	2.806973 E + 15	− 8.648024 E + 03	− 8.945288 E + 03	− 3.663737 E + 02	− 3.725292 E + 02
φ_k	4.041273 E + 06	2.750477 E + 03	1.502852 E + 03	1.307546 E + 03	9.178818 E + 02

6 (5*p*')	7 (3*d*')	8 (2*p*")	9 (2*s*)
1.492569 E − 01	1.579506 E − 01	1.691893 E − 01	1.924604 E − 01
− 3.727252 E + 02	− 3.727291 E + 02	− 3.846125 E + 02	− 8.734805 E + 01
3.729340 E + 02	2.494777 E + 02	2.300989 E + 02	2.021814 E + 02

10 (4*d*')	11 (3*d*")	12 (3*p*")	13 (3*s*)
2.863917 E − 01	5.894798 E − 01	6.151331 E − 01	6.155785 E − 01
− 2.037232 E + 01	− 2.053520 E + 01	− 8.651790 E + 00	− 2.496299 E + 00
1.372805 E + 02	5.348854 E + 01	3.393667 E + 01	3.292557 E + 01

14 (4*s*)	15 (4*p*")	16 (4*f*')	17 (4*d*")
1.785570 E + 00	1.940382 E + 00	2.298301 E + 00	2.448564 E + 00
− 4.494250 E − 01	− 3.655542 E − 01	− 1.694816 E − 01	− 1.702380 E − 01
9.680064 E + 00	4.253781 E + 00	3.240094 E + 00	2.588716 E + 00

Copyright © 2010 SciRes.

18 (5*s*)	19 (4*f*")	20 (5*p*")	21 (6*s*)
5.648357 E + 00	6.894903 E + 00	7.161220 E + 00	2.121609 E + 01
− 7.356273 E − 03	− 4.706705 E − 03	− 3.950365 E − 03	− 4.999715 E − 05
7.526164 E − 01	2.064493 E − 01	1.488919 E − 01	1.818341 E − 02

k	1 (**58 Ce**)	2 (2*p*')	3 (1*s*)	4 (3*p*')	5 (4*p*')
R_k	1.599118 E − 05	2.842692 E − 02	3.749201 E − 02	3.767547 E − 02	6.322577 E − 02
ρ_k	3.386083 E + 15	− 9.133412 E + 03	− 9.449945 E + 03	− 3.900092 E + 02	− 3.966276 E + 02
φ_k	4.352190 E + 06	2.861066 E + 03	1.561513 E + 03	1.361690 E + 03	9.593886 E + 02

6 (5*p*')	7 (3*d*')	8 (2*p*")	9 (2*s*)
1.472617 E − 01	1.536583 E − 01	1.656842 E − 01	1.885836 E − 01
− 3.968383 E + 02	− 3.968423 E + 02	− 4.097497 E + 02	− 9.321721 E + 01
3.867739 E + 02	2.608374 E + 02	2.416580 E + 02	2.115025 E + 02

10 (4*d*')	11 (3*d*")	12 (3*p*")	13 (3*s*)
2.781337 E − 01	5.734605 E − 01	6.004435 E − 01	6.016325 E − 01
− 2.202548 E + 01	− 2.220331 E + 01	− 9.295950 E + 00	− 2.677542 E + 00
1.449479 E + 02	5.710741 E + 01	3.630382 E + 01	3.511709 E + 01

14 (4*s*)	15 (4*p*")	16 (4*f*')	17 (4*d*")
1.746119 E + 00	1.894663 E + 00	2.055460 E + 00	2.377961 E + 00
− 4.850018 E − 01	− 3.953169 E − 01	− 1.847051 E − 01	− 1.868198 E − 01
1.043088 E + 01	4.660491 E + 00	3.931914 E + 00	3.110304 E + 00

18 (5*s*)	19 (4*f*")	20 (5*p*")	21 (6*s*)
5.566603 E + 00	6.166379 E + 00	7.065490 E + 00	2.108081 E + 01
− 8.994719 E − 03	− 6.226691 E − 03	− 4.112028 E − 03	− 5.096590 E − 05
7.995669 E − 01	2.456582 E − 01	1.710934 E − 01	1.840633 E − 02

k	1 (**59 Pr**)	2 (2*p*')	3 (3*p*')	4 (1*s*)	5 (4*p*')
R_k	1.512190 E − 05	2.785126 E − 02	3.680808 E − 02	3.682849 E − 02	6.183397 E − 02
ρ_k	4.073279 E + 15	− 9.636514 E + 03	− 9.973082 E + 03	− 9.980179 E + 03	− 4.216776 E + 02
φ_k	4.681737 E + 06	2.973704 E + 03	1.621891 E + 03	1.416684 E + 03	1.000719 E + 03

.

6 (5*p*')	7 (3*d*')	8 (2*p*")	9 (2*s*)
1.455508 E − 01	1.496529 E − 01	1.623291 E − 01	1.848684 E − 01
− 4.219028 E + 02	− 4.219070 E + 02	− 4.358787 E + 02	− 9.931069 E + 01
4.001429 E + 02	2.720948 E + 02	2.534467 E + 02	2.210478 E + 02

10 (4*d*')	11 (3*p*")	12 (3*d*")	13 (3*s*)
2.707756 E − 01	5.585121 E − 01	5.866197 E − 01	5.884677 E − 01
− 2.373995 E + 01	− 2.393267 E + 01	− 9.960942 E + 00	− 2.863529 E + 00
1.526084 E + 02	6.078199 E + 01	3.872898 E + 01	3.736104 E + 01

Copyright © 2010 SciRes.

14 (4*s*)	15 (4*p*")	16 (4*f*')	17 (4*d*")
1.709870 E + 00	1.852956 E + 00	1.908274 E + 00	2.315051 E + 00
− 5.205225 E − 01	− 4.250118 E − 01	− 1.998558 E − 01	− 2.038198 E − 01
1.118484 E + 01	5.061475 E + 00	4.525381 E + 00	3.569309 E + 00

18 (5*s*)	19 (4*f*")	20 (5*p*")	21 (6*s*)
5.494347 E + 00	5.724821 E + 00	6.983402 E + 00	2.095775 E + 01
− 1.110054 E − 02	− 8.221864 E − 03	− 4.257831 E − 03	− 5.186893 E − 05
8.379122 E − 01	2.752646 E − 01	1.889244 E − 01	1.860202 E − 02

k	1 (**60 Nd**)	2 (2*p*')	3 (3*p*')	4 (1*s*)	5 (4*p*')
R_k	1.429845 E − 05	2.729903 E − 02	3.598534 E − 02	3.618805 E − 02	6.052815 E − 02
ρ_k	4.899993 E + 15	− 1.015774 E + 04	− 1.051515 E + 04	− 1.052275 E + 04	− 4.477293 E + 02
φ_k	5.035292 E + 06	3.088887 E + 03	1.688947 E + 03	1.473064 E + 03	1.041376 E + 03

6 (5*p*')	7 (3*d*')	8 (2*p*")	9 (2*s*)
1.439487 E − 01	1.458807 E − 01	1.591104 E − 01	1.813003 E − 01
− 4.479693 E + 02	− 4.479737 E + 02	− 4.630575 E + 02	− 1.056481 E + 02
4.139305 E + 02	2.838705 E + 02	2.659183 E + 02	2.312467 E + 02

10 (4*d*')	11 (3*d*")	12 (3*p*")	13 (3*s*)
2.639634 E − 01	5.444343 E − 01	5.735075 E − 01	5.759484 E − 01
− 2.552730 E + 01	− 2.573532 E + 01	− 1.065151 E + 01	− 3.056072 E + 00
1.608111 E + 02	6.497240 E + 01	4.165075 E + 01	4.009460 E + 01

14 (4*s*)	15 (4*p*")	16 (4*d*")	17 (4*f*')
1.675726 E + 00	1.813825 E + 00	1.832209 E + 00	2.256809 E + 00
− 5.569315 E − 01	− 3.168863 E − 01	− 2.154176 E − 01	− 2.213890 E − 01
1.238404 E + 01	5.893310 E + 00	5.410196 E + 00	4.318720 E + 00

18 (5*s*)	19 (5*p*")	20 (4*f*")	21 (6*s*)
5.426173 E + 00	5.496626 E + 00	6.906539 E + 00	2.083995 E + 01
− 1.336062 E − 02	− 1.037207 E − 02	− 4.400710 E − 03	− 5.275352 E − 05
1.059656 E + 00	4.268438 E − 01	3.170839 E − 01	6.749257 E − 02

k	1 (**61 Pm**)	2 (2*p*')	3 (3*p*')	4 (1*s*)	5 (4*p*')
R_k	1.355498 E − 05	2.676874 E − 02	3.520315 E − 02	3.556952 E − 02	5.929694 E − 02
ρ_k	5.847159 E + 15	− 1.069743 E + 04	− 1.107650 E + 04	− 1.108461 E + 04	− 4.748046 E + 02
φ_k	5.400008 E + 06	3.205363 E + 03	1.756347 E + 03	1.529583 E + 03	1.081710 E + 03

6 (3*d*')	7 (5*p*')	8 (2*p*")	9 (2*s*)
1.423181 E − 01	1.424408 E − 01	1.560196 E − 01	1.778704 E − 01
− 4.750599 E + 02	− 4.913051 E + 02	− 4.913096 E + 02	− 1.122356 E + 02
4.272666 E + 02	2.949123 E + 02	2.776764 E + 02	2.408401 E + 02

10 (4*d*')	11 (3*d*'')	12 (3*p*'')	13 (3*s*)
2.576158 E − 01	5.311385 E − 01	5.610415 E − 01	5.640176 E − 01
− 2.738987 E + 01	− 2.761365 E + 01	− 1.136849 E + 01	− 3.255421 E + 00
1.683087 E + 02	6.842279 E + 01	4.381140 E + 01	4.205992 E + 01

14 (4*s*)	15 (4*p*'')	16 (4*f*')	17 (4*d*'')
1.643422 E + 00	1.776930 E + 00	1.784150 E + 00	2.202538 E + 00
− 5.943078 E − 01	− 4.867371 E − 01	− 2.314269 E − 01	− 2.395107 E − 01
1.277106 E + 01	5.915201 E + 00	5.450483 E + 00	4.332152 E + 00

18 (4*f*'')	19 (5*s*)	20 (5*p*'')	21 (6*s*)
5.352450 E + 00	5.361529 E + 00	6.834191 E + 00	2.072706 E + 01
− 1.572286 E − 02	− 7.639086 E − 03	− 4.541128 E − 03	− 5.362020 E − 05
9.264694 E − 01	3.046666 E − 01	2.061615 E − 01	1.896759 E − 02

k	1 (**62 Sm**)	2 (2*p*')	3 (3*p*')	4 (1*s*)	5 (4*p*')
R_k	1.284936 E − 05	2.625936 E − 02	3.446021 E − 02	3.497183 E − 02	5.814608 E − 02
ρ_k	6.976837 E + 15	− 1.125583 E + 04	− 1.165740 E + 04	− 1.166605 E + 04	− 5.029050 E + 02
φ_k	5.789945 E + 06	3.324344 E + 03	1.825273 E + 03	1.587449 E + 03	1.122785 E + 03

6 (3*d*')	7 (5*p*')	8 (2*p*'')	9 (2*s*)
1.389563 E − 01	1.410812 E − 01	1.530507 E − 01	1.745725 E − 01
− 5.031758 E + 02	− 5.206288 E + 02	− 5.206335 E + 02	− 1.190690 E + 02
4.468028 E + 02	3.063691 E + 02	2.878084 E + 02	2.510747 E + 02

10 (4*d*')	11 (3*d*'')	12 (3*p*'')	13 (3*s*)
2.517731 E − 01	5.185918 E − 01	5.492012 E − 01	5.526584 E − 01
− 2.932322 E + 01	− 2.956295 E + 01	− 1.210992 E + 01	− 3.460731 E + 00
1.762967 E + 02	7.236629 E + 01	4.645429 E + 01	4.450105 E + 01

14 (4*s*)	15 (4*f*')	16 (4*p*'')	17 (4*d*'')
1.613085 E + 00	1.732378 E + 00	1.742442 E + 00	2.152586 E + 00
− 6.321350 E − 01	− 5.183802 E − 01	− 5.289767 E − 01	− 2.582047 E − 01
1.358776 E + 01	6.391937 E + 00	5.920541 E + 00	4.697597 E + 00

18 (4*f*'')	19 (5*s*)	20 (5*p*'')	21 (6*s*)
5.197135 E + 00	5.301955 E + 00	6.768956 E + 00	2.062113 E + 01
− 1.847299 E - 02	− 7.876521 E − 03	− 4.672957 E − 03	− 5.445075 E − 05
1.005250 E + 00	3.186345 E − 01	2.091799 E − 01	1.913206 E − 02

k	1 (**63 Eu**)	2 (2*p*')	3 (3*p*')	4 (1*s*)	5 (4*p*')
R_k	1.219082 E − 05	2.576970 E − 02	3.375364 E − 02	3.439396 E − 02	5.706899 E − 02
ρ_k	8.301428 E + 15	− 1.183327 E + 04	− 1.225816 E + 04	− 1.226736 E + 04	− 5.320452 E + 02
φ_k	6.201154 E + 06	3.445400E + 03	1.895290 E + 03	1.646235 E + 03	1.164159 E + 03

Copyright © 2010 SciRes.

6 (3*d*')	7 (5*p*')	8 (2*p*'')	9 (2*s*)
1.357784 E − 01	1.398620 E − 01	1.501968 E − 01	1.713991 E − 01
− 5.323316 E + 02	− 5.510390 E + 02	− 5.510438 E + 02	− 1.261507 E + 02
4.666162 E + 02	3.178006 E + 02	2.979675 E + 02	2.615256 E + 02

10 (4*d*')	11 (3*d*'')	12 (3*p*'')	13 (3*s*)
2.463879 E − 01	5.067318 E − 01	5.379403 E − 01	5.418307 E − 01
− 3.132728 E + 01	− 3.158308 E + 01	− 1.287570 E + 01	− 3.671886 E + 00
1.843447 E + 02	7.637629 E + 01	4.915445 E + 01	4.699317 E + 01

14 (4*s*)	15 (4*f*')	16 (4*p*'')	17 (4*d*'')
1.584561 E + 00	1.676329 E + 00	1.710165 E + 00	2.106543 E + 00
− 6.703014 E − 01	− 5.502921 E − 01	− 5.639366 E − 01	− 2.775422 E − 01
1.440904 E + 01	6.931056 E + 00	6.421800 E + 00	5.042089 E + 00

18 (4*f*'')	19 (5*s*)	20 (5*p*'')	21 (6*s*)
5.028988 E + 00	5.247153 E + 00	6.710462 E + 00	2.052170 E + 01
− 2.174508 E − 02	− 8.100574 E − 03	− 4.795583 E − 03	− 5.524607 E − 05
1.093016 E + 00	3.350770 E − 01	2.119955 E − 01	1.928248 E − 02

k	1 (**64 Gd**)	2 (2*p*')	3 (3*p*')	4 (1*s*)	5 (4*p*')
R_k	1.157214 E − 05	2.529679 E − 02	3.306830 E − 02	3.383459 E − 02	5.597565 E − 02
ρ_k	9.859391 E + 15	− 1.243045 E + 04	− 1.287962 E + 04	− 1.288941 E + 04	− 5.623746 E + 02
φ_k	6.636392 E + 06	3.568843 E + 03	1.966987 E + 03	1.706333 E + 03	1.207276 E + 03

6 (3*d*')	7 (5*p*')	8 (2*p*'')	9 (2*s*)
1.327075 E − 01	1.383863 E − 01	1.474405 E − 01	1.683315 E − 01
− 5.626781 E + 02	− 5.827144 E + 02	− 5.827193 E + 02	− 1.335489 E + 02
4.871441 E + 02	3.299331 E + 02	3.087194 E + 02	2.722655 E + 02

10 (4*d*')	11 (3*d*'')	12 (3*p*'')	13 (3*s*)
2.408313 E − 01	4.952712 E − 01	5.270179 E − 01	5.313159 E − 01
− 3.344636 E + 01	− 3.372027 E + 01	− 1.368393 E + 01	− 3.895931 E + 00
1.929045 E + 02	8.062657 E + 01	5.201204 E + 01	4.963145 E + 01

14 (4*s*)	15 (4*p*'')	16 (4*f*')	17 (4*d*'')
1.555765 E + 00	1.677401 E + 00	1.696154 E + 00	2.059036 E + 00
− 7.125924 E − 01	− 5.857953 E − 01	− 2.822890 E − 01	− 2.973424 E − 01
1.534610 E + 01	7.325831 E + 00	6.736773 E + 00	5.441206 E + 00

18 (4*f*'')	19 (5*s*)	20 (5*p*'')	21 (6*s*)
5.088462 E + 00	5.185206 E + 00	6.639659 E + 00	2.041409 E + 01
− 2.342792 E − 02	− 8.374598 E − 03	− 4.949733 E − 03	− 5.612436 E − 05
1.110918 E + 00	3.285374 E − 01	2.153353 E − 01	1.946442 E − 02

Copyright © 2010 SciRes.

k	1 (**65 Tb**)	2 (2p')	3 (3p')	4 (1s)	5 (4p')
R_k	1.099388 E − 05	2.484157 E − 02	3.241524 E − 02	3.329320 E − 02	5.495105 E − 02
ρ_k	1.167810 E + 16	− 1.304731 E + 04	− 1.352163 E + 04	− 1.353202 E + 04	− 5.937848 E + 02
φ_k	7.094619 E + 06	3.694361 E + 03	2.039781 E + 03	1.767355 E + 03	1.250692 E + 03

6 (3d')	7 (5p')	8 (2p")	9 (2s)
1.297977 E − 01	1.370587 E − 01	1.447873 E − 01	1.653759 E − 01
− 5.941056 E + 02	− 6.155199 E + 02	− 6.155250 E + 02	− 1.412059 E + 02
5.079517 E + 02	3.420359 E + 02	3.194925 E + 02	2.832223 E + 02

10 (4d')	11 (3d")	12 (3p")	13 (3s)
2.357027 E − 01	4.844117 E − 01	5.166100 E − 01	5.212751 E − 01
− 3.563983 E + 01	− 3.593202 E + 01	− 1.451773 E + 01	− 4.126144 E + 00
2.015240 E + 02	8.494418 E + 01	5.492782 E + 01	5.232165 E + 01

14 (4s)	15 (4p")	16 (4f')	17 (4d")
1.528655 E + 00	1.646698 E + 00	1.695881 E + 00	2.015188 E + 00
− 7.552868 E − 01	− 6.216232 E − 01	− 3.008211 E − 01	− 3.177642 E − 01
1.628864 E + 01	7.862463 E + 00	7.114606 E + 00	5.792547 E + 00

18 (4f")	19 (5s)	20 (5p")	21 (6s)
5.087643 E + 00	5.128200 E + 00	6.575961 E + 00	2.031322 E + 01
− 2.557768 E − 02	− 8.634514 E − 03	− 5.094160 E − 03	− 5.696462 E − 05
1.149220 E + 00	3.282643 E − 01	2.184604 E − 01	1.963136 E − 02

k	1 (**66 Dy**)	2 (2p')	3 (3p')	4 (1s)	5 (4p')
R_k	1.045269 E − 05	2.440289 E − 02	3.179110 E − 02	3.276889 E − 02	5.398232 E − 02
ρ_k	1.379658 E + 16	− 1.368419 E + 04	− 1.418455 E + 04	− 1.419557 E + 04	− 6.263047 E + 02
φ_k	7.576753 E + 06	3.821960 E + 03	2.113703 E + 03	1.829316 E + 03	1.294514 E + 03

6 (3d')	7 (5p')	8 (2p")	9 (2s)
1.270311 E − 01	1.358371 E − 01	1.422305 E − 01	1.625253 E − 01
− 6.266431 E + 02	− 6.494872 E + 02	− 6.494924 E + 02	− 1.491312 E + 02
5.290553 E + 02	3.541427 E + 02	3.303080 E + 02	2.943813 E + 02

10 (4d')	11 (3d")	12 (3p")	13 (3s)
2.309114 E − 01	4.740864 E − 01	5.066629 E − 01	5.116604 E − 01
− 3.791227 E + 01	− 3.822303 E + 01	− 1.537886 E + 01	− 4.363147 E + 00
2.102216 E + 02	8.932320 E + 01	5.788990 E + 01	5.505145 E + 01

14 (4s)	15 (4p")	16 (4f')	17 (4d")
1.502929 E + 00	1.617668 E + 00	1.686402 E + 00	1.974224 E + 00
− 7.986697 E − 01	− 6.580243 E − 01	− 3.196398 E − 01	− 3.387848 E − 01
1.722567 E + 01	8.385086 E + 00	7.508497 E + 00	6.148345 E + 00

Copyright © 2010 SciRes.

18 (4*f*")	19 (5*s*)	20 (5*p*")	21 (6*s*)
5.059205 E + 00	5.074819 E + 00	6.517351 E + 00	2.021750 E + 01
− 2.803033 E − 02	− 8.885350 E − 03	− 5.232098 E − 03	− 5.777754 E − 05
1.178608 E + 00	3.118441 E − 01	2.048830 E − 01	1.315337 E − 02

k	1 (**67 Ho**)	2 (2*p*')	3 (3*p*')	4 (1*s*)	5 (4*p*')
R_k	9.945252 E − 06	2.397961 E − 02	3.119218 E − 02	3.226082 E − 02	5.305342 E − 02
ρ_k	1.626068 E + 16	− 1.434149 E + 04	− 1.486882 E + 04	− 1.488048 E + 04	− 6.599750 E + 02
φ_k	8.084010 E + 06	3.951747 E + 03	2.188906 E + 03	1.892339 E + 03	1.339029 E + 03

6 (3*d*')	7 (5*p*')	8 (2*p*")	9 (2*s*)
1.243882 E − 01	1.346577 E − 01	1.397634 E − 01	1.597724 E − 01
− 6.603314 E + 02	− 6.846629 E + 02	− 6.846682 E + 02	− 1.573397 E + 02
5.505829 E + 02	3.664274 E + 02	3.413134 E + 02	3.058120 E + 02

10 (4*d*')	11 (3*d*")	12 (3*p*")	13 (3*s*)
2.263474 E − 01	4.642232 E − 01	4.971177 E − 01	5.024187 E − 01
− 4.027217 E + 01	− 4.060211 E + 01	− 1.627070 E + 01	− 4.608181 E + 00
2.191267 E + 02	9.384923 E + 01	6.097224 E + 01	5.789403 E + 01

14 (4*s*)	15 (4*p*")	16 (4*f*')	17 (4*d*")
1.478214 E + 00	1.589832 E + 00	1.680044 E + 00	1.935203 E + 00
− 8.433617 E − 01	− 6.955431 E − 01	− 3.390715 E − 01	− 3.603710 E − 01
1.823287 E + 01	8.969195 E + 00	7.941848 E + 00	6.547806 E + 00

18 (5*s*)	19 (4*f*")	20 (5*p*")	21 (6*s*)
5.023137 E + 00	5.040132 E + 00	6.460761 E + 00	2.012445 E + 01
− 3.043672 E − 02	− 2.666954 E − 02	− 5.370063 E − 03	− 5.858267 E − 05
1.254156 E + 00	3.325995 E − 01	2.233961 E − 01	1.994078 E − 02

k	1 (**68 Er**)	2 (2*p*')	3 (3*p*')	4 (1*s*)	5 (4*p*')
R_k	9.469073 E − 06	2.357091 E − 02	3.061683 E − 02	3.176825 E − 02	5.216126 E − 02
ρ_k	1.912044 E + 16	− 1.501953 E + 04	− 1.557477 E + 04	− 1.558710 E + 04	− 6.948161 E + 02
φ_k	8.617273 E + 06	4.083653 E + 03	2.265324 E + 03	1.956354 E + 03	1.384176 E + 03

6 (3*d*')	7 (5*p*')	8 (2*p*")	9 (2*s*)
1.218603 E − 01	1.335162 E − 01	1.373813 E − 01	1.571122 E − 01
− 6.951912 E + 02	− 7.210684 E + 02	− 7.210739 E + 02	− 1.658366 E + 02
5.724670 E + 02	3.788218 E + 02	3.524393 E + 02	3.174441 E + 02

10 (4*d*')	11 (3*d*")	12 (3*p*")	13 (3*s*)
2.219906 E − 01	4.547890 E − 01	4.879482 E − 01	4.935263 E − 01
− 4.272134 E + 01	− 4.307108 E + 01	− 1.719384 E + 01	− 4.861411 E + 00
2.281714 E + 02	9.845260 E + 01	6.410479 E + 01	6.077933 E + 01

Copyright © 2010 SciRes.

14 (4*s*)	15 (4*p*")	16 (4*f*')	17 (4*d*")
1.454434 E + 00	1.563097 E + 00	1.676339 E + 00	1.897953 E + 00
− 8.894001 E − 01	− 7.342118 E − 01	− 3.591345 E − 01	− 3.825247 E − 01
1.924028 E + 01	9.544839 E + 00	8.344504 E + 00	6.920616 E + 00

18 (5*s*)	19 (4*f*")	20 (5*p*")	21 (6*s*)
4.973004 E + 00	5.029016 E + 00	6.405994 E + 00	2.003387 E + 01
− 3.278073 E − 02	− 3.272135 E − 02	− 5.508257 E − 03	− 5.938094 E − 05
1.310607 E + 00	3.202432 E − 01	2.122952 E − 01	1.541445 E − 02

k	1 (**69 Tm**)	2 (2*p*')	3 (3*p*')	4 (1*s*)	5 (4*p*')
R_k	9.022326 E − 06	2.317622 E − 02	3.006476 E − 02	3.129052 E − 02	5.131126 E − 02
ρ_k	2.242874 E + 16	− 1.571857 E + 04	− 1.630266 E + 04	− 1.631569 E + 04	− 7.308296 E + 02
φ_k	9.176975 E + 06	4.217696 E + 03	2.342943 E + 03	2.021375 E + 03	1.429839 E + 03

6 (3*d*')	7 (5*p*')	8 (2*p*")	9 (2*s*)
1.194452 E − 01	1.324514 E − 01	1.350809 E − 01	1.545411 E − 01
− 7.312236 E + 02	− 7.587025 E + 02	− 7.587081 E + 02	− 1.746181 E + 02
5.947097 E + 02	3.912844 E + 02	3.636650 E + 02	3.293243 E + 02

10 (4*d*')	11 (3*d*")	12 (3*p*")	13 (3*s*)
2.178790 E − 01	4.457756 E − 01	4.791497 E − 01	4.849797 E − 01
− 4.525532 E + 01	− 4.562524 E + 01	− 1.814636 E + 01	− 5.122005 E + 00
2.373568 E + 02	1.031677 E + 02	6.733126 E + 01	6.375168 E + 01

14 (4*s*)	15 (4*p*")	16 (4*f*')	17 (4*d*")
1.431713 E + 00	1.537626 E + 00	1.667520 E + 00	1.862801 E + 00
− 9.362794 E − 01	− 7.735846 E − 01	− 3.795567 E − 01	− 4.053003 E − 01
2.029026 E + 01	1.015463 E + 01	8.798674 E + 00	7.337621 E + 00

18 (5*s*)	19 (4*f*")	20 (5*p*")	21 (6*s*)
4.925525 E + 00	5.002560 E + 00	6.354907 E + 00	1.994718 E + 01
− 3.538065 E − 02	− 3.138504 E − 02	− 5.641505 E − 03	− 6.015851 E − 05
1.391601 E + 00	3.364342 E − 01	2.255136 E − 01	2.023324 E − 02

k	1 (**70 Yb**)	2 (2*p*')	3 (3*p*')	4 (1*s*)	5 (4*p*')
R_k	8.533454 E − 06	2.279488 E − 02	2.953483 E − 02	3.082698 E − 02	5.050267 E − 02
ρ_k	2.689273 E + 16	− 1.643892 E + 04	− 1.705282 E + 04	− 1.706656 E + 04	− 7.680314 E + 02
φ_k	9.843350 E + 06	4.356263 E + 03	2.424143 E + 03	2.089788 E + 03	1.478365 E + 03

6 (3*d*')	7 (5*p*')	8 (2*p*")	9 (2*s*)
1.171367 E − 01	1.314809 E − 01	1.328583 E − 01	1.520552 E − 01
− 7.684410 E + 02	− 7.975768 E + 02	− 7.975825 E + 02	− 1.836854 E + 02
6.196960 E + 02	4.061612 E + 02	3.773473 E + 02	3.438525 E + 02

Copyright © 2010 SciRes.

10 (4*d*')	11 (3*d*'')	12 (3*p*'')	13 (3*s*)
2.140080 E − 01	4.371600 E − 01	4.707041 E − 01	4.767629 E − 01
− 4.787355 E + 01	− 4.826391 E + 01	− 1.912814 E + 01	− 5.390067 E + 00
2.490679 E + 02	1.103905 E + 02	7.305095 E + 01	6.921061 E + 01

14 (4*s*)	15 (4*p*'')	16 (4*d*'')	17 (4*f*')
1.410030 E + 00	1.513395 E + 00	1.652496 E + 00	1.829705 E + 00
− 9.841722 E − 01	− 8.138557 E − 01	− 4.005970 E − 01	− 4.046665 E − 01
2.378244 E + 01	1.319903 E + 01	1.171609 E + 01	1.020663 E + 01

18 (5*s*)	19 (5*p*'')	20 (6*s*)	21 (4*f*'')
4.880889 E + 00	4.957488 E + 00	6.308344 E + 00	1.986459 E + 01
− 1.430803 E − 02	− 1.020179 E − 02	− 6.132236 E − 03	− 4.263839 E − 04
3.435089 E + 00	1.892657 E + 00	1.467032 E + 00	1.425577 E − 01

k	1 (**71 Lu**)	2 (2*p*')	3 (3*p*')	4 (1*s*)	5 (4*p*')
R_k	8.266763 E − 06	2.241482 E − 02	2.895126 E − 02	3.037472 E − 02	4.909457 E − 02
ρ_k	3.000290 E + 16	− 1.718498 E + 04	− 1.783064 E + 04	− 1.784522 E + 04	− 8.077731 E + 02
φ_k	1.030606 E + 07	4.493213 E + 03	2.505109 E + 03	2.156018 E + 03	1.536383 E + 03

6 (3*d*')	7 (5*p*')	8 (2*p*'')	9 (2*s*)	10 (4*d*')
1.145729 E − 01	1.230806 E − 01	1.306431 E − 01	1.495764 E − 01	2.060470 E − 01
− 8.082229 E + 02	− 8.393586 E + 02	− 8.393656 E + 02	− 1.937087 E + 02	− 5.103228 E + 01
6.427891 E + 02	4.323445 E + 02	3.989907 E + 02	3.527581 E + 02	2.592397 E + 02

11 (3*d*'')	12 (3*p*'')	13 (3*s*)	14 (5*d*')	15 (4*f*')
4.275920 E − 01	4.614035 E − 01	4.677554 E − 01	9.189539 E − 01	1.362795 E + 00
− 5.146966 E + 01	− 2.033393 E + 01	− 5.748237 E + 00	− 1.082878 E + 00	− 1.082977 E + 00
1.129170 E + 02	7.322243 E + 01	6.907144 E + 01	3.719560 E + 01	1.636277 E + 01

16 (4*s*)	17 (4*p*'')	18 (4*d*'')	19 (4*f*'')
1.374502 E + 00	1.471199 E + 00	1.761641 E + 00	4.088386 E + 00
− 1.133767 E + 00	− 9.498991 E − 01	− 5.000522 E − 01	− 6.267649 E − 02
1.166921 E + 01	1.081014 E + 01	8.408322 E + 00	1.930121 E + 00

20 (5*s*)	21 (5*p*'')	22 (5*d*'')	23 (6*s*)
4.645356 E + 00	5.905303 E + 00	1.341504 E + 01	1.902817 E + 01
− 1.188695 E − 02	− 7.123908 E − 03	− 1.682207 E − 04	− 6.930276 E − 05
5.542266 E − 01	3.295314 E − 01	6.708647 E − 02	4.500897 E − 03

k	1 (**72 Hf**)	2 (2*p*')	3 (3*p*')	4 (1*s*)	5 (4*p*')
R_k	7.942153 E − 06	2.204711 E − 02	2.838944 E − 02	2.993548 E − 02	4.777245 E − 02
ρ_k	3.431067 E + 16	− 1.795337 E + 04	− 1.863188 E + 04	− 1.864735 E + 04	− 8.488828 E + 02
φ_k	1.087839 E + 07	4.634963 E + 03	2.590096 E + 03	2.225943 E + 03	1.597709 E + 03

Copyright © 2010 SciRes.

6 (3*d*')	7 (5*p*')	8 (2*p*")	9 (2*s*)	10 (4*d*')
1.121167 E − 01	1.166256 E − 01	1.285000 E − 01	1.471763 E − 01	1.987707 E − 01
− 8.493792 E + 02	− 8.825983 E + 02	− 8.826065 E + 02	− 2.041024 E + 02	− 5.433133 E + 01
6.689327 E + 02	4.589846 E + 02	4.212568 E + 02	3.644445 E + 02	2.720719 E + 02

11 (3*d*")	12 (3*p*")	13 (3*s*)	14 (5*d*')	15 (4*f*')
4.184252 E − 01	4.524498 E − 01	4.590678 E − 01	7.958842 E − 01	1.182512 E + 00
− 5.481852 E + 01	− 2.159127 E + 01	− 6.122393 E + 00	− 1.187123 E + 00	− 1.187427 E + 00
1.181039 E + 02	7.603467 E + 01	7.156347 E + 01	4.406821 E + 01	2.099441 E + 01

16 (4*s*)	17 (4*p*")	18 (4*d*")	19 (4*f*")
1.340888 E + 00	1.431579 E + 00	1.699431 E + 00	3.547535 E + 00
− 1.265168 E + 00	− 1.067123 E + 00	− 5.788844 E − 01	− 9.169640 E − 02
1.329924 E + 01	1.101342 E + 01	8.611454 E + 00	2.453383 E + 00

20 (5*s*)	21 (5*p*")	22 (5*d*")	23 (6*s*)
4.454872 E + 00	5.595599 E + 00	1.161845 E + 01	1.856056 E + 01
− 1.395547 E − 02	− 8.554943 E − 03	− 3.792083 E − 04	− 7.467376 E − 05
7.626280 E − 01	4.153868 E − 01	9.719603 E − 02	7.325306 E − 03

k	1 (**73 Ta**)	2 (2*p*')	3 (3*p*')	4 (1*s*)	5 (4*p*')
R_k	7.631713 E − 06	2.169085 E − 02	2.784660 E − 02	2.950866 E − 02	4.651300 E − 02
ρ_k	3.920741 E + 16	− 1.874457 E + 04	− 1.945706 E + 04	− 1.947345 E + 04	− 8.914216 E + 02
φ_k	1.147814 E + 07	4.779089 E + 03	2.676727 E + 03	2.297139 E + 03	1.660270 E + 03

6 (3*d*')	7 (5*p*')	8 (2*p*")	9 (2*s*)	10 (4*d*')
1.097535 E − 01	1.111061 E − 01	1.264236 E − 01	1.448492 E − 01	1.919797 E − 01
− 8.919505 E + 02	− 9.273707 E + 02	− 9.273802 E + 02	− 2.148920 E + 02	− 5.778574 E + 01
6.957360 E + 02	4.852762 E + 02	4.430852 E + 02	3.764243 E + 02	2.852119 E + 02

11 (3*d*")	12 (3*p*")	13 (3*s*)	14 (5*d*')	15 (4*f*')
4.096055 E − 01	4.437983 E − 01	4.506598 E − 01	7.279785 E − 01	1.052722 E + 00
− 5.832648 E + 01	− 2.280348 E + 01	− 6.515035 E + 00	− 1.298346 E + 00	− 1.298943 E + 00
1.234953 E + 02	7.900383 E + 01	7.420106 E + 01	4.903137 E + 01	2.527371 E + 01

16 (4*s*)	17 (4*p*")	18 (4*d*")	19 (4*f*")
1.308684 E + 00	1.393838 E + 00	1.641369 E + 00	3.158166 E + 00
− 1.409128 E + 00	− 1.196100 E + 00	− 6.671165 E − 01	− 1.263770 E − 01
1.484975 E + 01	1.131803 E + 01	8.915607 E + 00	3.000450 E + 00

20 (5*s*)	21 (5*p*")	22 (5*d*")	23 (6*s*)
4.287157 E + 00	5.330777 E + 00	1.062715 E + 01	1.819478 E + 01
− 1.619138 E − 02	− 1.013193 E − 02	− 6.761963 E − 04	− 7.926851 E − 05
9.792991 E − 01	5.038921 E − 01	1.234208 E − 01	9.712115 E − 03

Copyright © 2010 SciRes.

k	1 (**74 W**)	2 (2*p*')	3 (3*p*')	4 (1*s*)	5 (4*p*')
R_k	7.335294 E − 06	2.134557 E − 02	2.732218 E − 02	2.909372 E − 02	4.531461 E − 02
ρ_k	4.476005 E + 16	− 1.955890 E + 04	− 2.030652 E + 04	− 2.032387 E + 04	− 9.354103 E + 02
φ_k	1.210557 E + 07	4.925515 E + 03	2.764911 E + 03	2.369521 E + 03	1.723925 E + 03

6 (5*p*')	7 (3*d*')	8 (2*p*")	9 (2*s*)	10 (4*d*')
1.062835 E − 01	1.074799 E − 01	1.244111 E − 01	1.425921 E − 01	1.856389 E − 01
− 9.359824 E + 02	− 9.359932 E + 02	− 9.737090 E + 02	− 2.260828 E + 02	− 6.139738 E + 01
7.309494 E + 02	5.113910 E + 02	4.618265 E + 02	3.886275 E + 02	2.985765 E + 02

11 (3*d*")	12 (3*p*")	13 (3*s*)	14 (5*d*')	15 (4*f*')
4.011205 E − 01	4.354405 E − 01	4.425243 E − 01	6.785347 E − 01	9.535360 E − 01
− 6.199545 E + 01	− 2.427965 E + 01	− 6.926302 E + 00	− 1.416575 E + 00	− 1.417558 E + 00
1.290182 E + 02	8.205992 E + 01	7.691620 E + 01	5.342073 E + 01	2.945134 E + 01

16 (4*s*)	17 (4*p*")	18 (4*d*")	19 (4*f*")
1.277873 E + 00	1.357926 E + 00	1.587157 E + 00	2.860608 E + 00
− 1.565828 E + 00	− 1.337016 E + 00	− 7.649445 E − 01	− 1.668816 E − 01
1.633277 E + 01	1.168801 E + 01	9.286319 E + 00	3.565638 E + 00

20 (5*s*)	21 (5*p*")	22 (5*d*")	23 (6*s*)
4.137164 E + 00	5.099395 E + 00	9.905362 E + 00	1.789615 E + 01
− 1.861103 E − 02	− 1.186834 E − 02	− 1.066182 E − 03	− 8.330332 E − 05
1.197595 E + 00	5.905312 E − 01	1.466285 E − 01	1.066271 E − 02

k	1 (**75 Re**)	2 (2*p*')	3 (3*p*')	4 (1*s*)	5 (4*p*')
R_k	7.052590 E − 06	2.101090 E − 02	2.681617 E − 02	2.869023 E − 02	4.417950 E − 02
ρ_k	5.104189 E + 16	− 2.039662 E + 04	− 2.118055 E + 04	− 2.119890 E + 04	− 9.808544 E + 02
φ_k	1.276098 E + 07	5.074261 E + 03	2.854636 E + 03	2.443103 E + 03	1.788532 E + 03

6 (5*p*')	7 (3*d*')	8 (2*p*")	9 (2*s*)	10 (4*d*')
1.020708 E − 01	1.052952 E − 01	1.224605 E − 01	1.404029 E − 01	1.797421 E − 01
− 9.814717 E + 02	− 9.814839 E + 02	− 1.021596 E + 03	− 2.376730 E + 02	− 6.516340 E + 01
7.738094 E + 02	5.373127 E + 02	4.779253 E + 02	4.011031 E + 02	3.121685 E + 02

11 (3*d*")	12 (3*p*")	13 (3*s*)	14 (5*d*')	15 (4*f*')
3.929669 E − 01	4.273761 E − 01	4.346616 E − 01	6.321120 E − 01	8.751885 E − 01
− 6.582227 E + 01	− 2.570976 E + 01	− 7.355407 E + 00	− 1.541238 E + 00	− 1.542757 E + 00
1.347099 E + 02	8.524797 E + 01	7.975271 E + 01	5.819505 E + 01	3.383441 E + 01

16 (4*s*)	17 (4*p*")	18 (4*d*")	19 (4*f*")
1.248527 E + 00	1.323911 E + 00	1.536742 E + 00	2.625565 E + 00
− 1.734519 E + 00	− 1.489190 E + 00	− 8.718813 E − 01	− 2.130049 E − 01
1.778149 E + 01	1.212521 E + 01	9.722206 E + 00	4.151119 E + 00

Copyright © 2010 SciRes.

20 (5*s*)	21 (5*p*")	22 (5*d*")	23 (6*s*)
4.003368 E + 00	4.897269 E + 00	9.227675 E + 00	1.766722 E + 01
− 2.124345 E − 02	− 1.380188 E − 02	− 1.606236 E − 03	− 8.658389 E − 05
1.415530 E + 00	6.732158 E − 01	1.719958 E − 01	1.225940 E − 02

k	1 (**76 W**)	2 (2*p*')	3 (3*p*')	4 (1*s*)	5 (4*p*')
R_k	6.782561 E − 06	2.068583 E − 02	2.632472 E − 02	2.829760 E − 02	4.307877 E − 02
ρ_k	5.814921 E + 16	− 2.125837 E + 04	− 2.207983 E + 04	− 2.209924 E + 04	− 1.027866 E + 03
φ_k	1.344595 E + 07	5.225432 E + 03	2.946108 E + 03	2.517994 E + 03	1.854817 E + 03

6 (5*p*')	7 (3*d*')	8 (2*p*")	9 (2*s*)	10 (4*d*')
9.799526 E − 02	1.031804 E − 01	1.205659 E − 01	1.382751 E − 01	1.740920 E − 01
− 1.028532 E + 03	− 1.028545 E + 03	− 1.071175 E + 03	− 2.497110 E + 02	− 6.911444 E + 01
8.191251 E + 02	5.643502 E + 02	4.943785 E + 02	4.138285 E + 02	3.261744 E + 02

11 (3*d*")	12 (3*p*")	13 (3*s*)	14 (5*d*')	15 (4*f*')
3.850746 E − 01	4.195437 E − 01	4.270153 E − 01	6.193245 E − 01	8.085513 E − 01
− 6.983957 E + 01	− 2.720979 E + 01	− 7.808158 E + 00	− 1.676031 E + 00	− 1.677970 E + 00
1.405995 E + 02	8.855556 E + 01	8.269640 E + 01	6.040299 E + 01	3.733654 E + 01

16 (4*s*)	17 (4*p*")	18 (4*d*")	19 (4*f*")
1.219978 E + 00	1.290925 E + 00	1.488435 E + 00	2.425654 E + 00
− 1.921159 E + 00	− 1.658201 E + 00	− 9.923529 E − 01	− 2.672200 E − 01
1.927409 E + 01	1.264124 E + 01	1.024084 E + 01	4.810809 E + 00

20 (5*s*)	21 (5*p*")	22 (5*d*")	23 (6*s*)
3.872806 E + 00	4.701730 E + 00	9.041002 E + 00	1.736408 E + 01
− 2.403135 E − 02	− 1.581149 E − 02	− 2.030086 E − 03	− 9.119816 E − 05
1.678574 E + 00	7.911883 E − 01	1.919439 E − 01	1.255294 E − 02

k	1 (**77 Ir**)	2 (2*p*')	3 (3*p*')	4 (1*s*)	5 (4*p*')
R_k	6.524992 E − 06	2.037057 E − 02	2.585066 E − 02	2.791552 E − 02	4.203832 E − 02
ρ_k	6.617015 E + 16	− 2.214417 E + 04	− 2.300436 E + 04	− 2.302485 E + 04	− 1.076373 E + 03
φ_k	1.416063 E + 07	5.378885 E + 03	3.039060 E + 03	2.594036 E + 03	1.921907 E + 03

6 (5*p*')	7 (3*d*')	8 (2*p*")	9 (2*s*)	10 (4*d*')
9.440459 E − 02	1.011485 E − 01	1.187284 E − 01	1.362102 E − 01	1.688400 E − 01
− 1.077089 E + 03	− 1.077105 E + 03	− 1.122356 E + 03	− 2.621587 E + 02	− 7.322356 E + 01
8.638821 E + 02	5.912136 E + 02	5.111503 E + 02	4.268041 E + 02	3.403589 E + 02

11 (3*d*")	12 (3*p*")	13 (3*s*)	14 (5*d*')	15 (4*f*')
3.774915 E − 01	4.119886 E − 01	4.196280 E − 01	5.983490 E − 01	7.535920 E − 01
− 7.401849 E + 01	− 2.876770 E + 01	− 8.279000 E + 00	− 1.817282 E + 00	− 1.819790 E + 00
1.466288 E + 02	9.197084 E + 01	8.573813 E + 01	6.355893 E + 01	4.117309 E + 01

Copyright © 2010 SciRes.

16 (4*s*)	17 (4*p*")	18 (4*d*")	19 (4*f*")
1.192849 E + 00	1.259747 E + 00	1.443532 E + 00	2.260776 E + 00
− 2.120161 E + 00	− 1.838851 E + 00	− 1.122330 E + 00	− 3.274016 E − 01
2.075273 E + 01	1.320819 E + 01	1.080825 E + 01	5.489014 E + 00

20 (5*s*)	21 (5*p*")	22 (5*d*")	23 (6*s*)
3.755672 E + 00	4.529453 E + 00	8.734797 E + 00	1.712980 E + 01
− 2.703104 E − 02	− 1.801785 E − 02	− 2.603355 E − 03	− 9.499142 E − 05
1.938918 E + 00	9.033696 E − 01	2.149277 E − 01	1.326012 E − 02

k	1 (**78 Pt**)	2 (2*p*')	3 (3*p*')	4 (1*s*)	5 (4*p*')
R_k	6.279256 E − 06	2.006461 E − 02	2.539271 E − 02	2.754356 E − 02	4.104965 E − 02
ρ_k	7.521102 E + 16	− 2.305439 E + 04	− 2.395454 E + 04	− 2.397616 E + 04	− 1.126414 E + 03
φ_k	1.490592 E + 07	5.534636 E + 03	3.133523 E + 03	2.671247 E + 03	1.989927 E + 03

6 (5*p*')	7 (3*d*')	8 (2*p*")	9 (2*s*)	10 (4*d*')
9.115679 E − 02	9.919285 E − 02	1.169451 E − 01	1.342048 E − 01	1.639215 E − 01
− 1.127184 E + 03	− 1.127201 E + 03	− 1.175181 E + 03	− 2.750300 E + 02	− 7.749827 E + 01
9.087151 E + 02	6.181979 E + 02	5.282418 E + 02	4.400267 E + 02	3.547585 E + 02

11 (3*d*")	12 (3*p*")	13 (3*s*)	14 (5*d*')	15 (4*f*')
3.701928 E − 01	4.046900 E − 01	4.124811 E − 01	5.775879 E − 01	7.069320 E − 01
− 7.836692 E + 01	− 3.038651 E + 01	− 8.769163 E + 00	− 1.965711 E + 00	− 1.968898 E + 00
1.528042 E + 02	9.549197 E + 01	8.887572 E + 01	6.694126 E + 01	4.511803 E + 01

16 (4*s*)	17 (4*p*")	18 (4*d*")	19 (4*f*")
1.166953 E + 00	1.230120 E + 00	1.401480 E + 00	2.120796 E + 00
− 2.332757 E + 00	− 2.032301 E + 00	− 1.262751 E + 00	− 3.940994 E − 01
2.224029 E + 01	1.382535 E + 01	1.142476 E + 01	6.196621 E + 00

20 (5*s*)	21 (5*p*")	22 (5*d*")	23 (6*s*)
3.648215 E + 00	4.373626 E + 00	8.431724 E + 00	1.692784 E + 01
− 3.024032 E − 02	− 2.040700 E − 02	− 3.285504 E − 03	− 9.843213 E − 05
2.205280 E + 00	1.017173 E + 00	2.390923 E − 01	1.402244 E − 02

k	1 (**79 Au**)	2 (2*p*')	3 (3*p*')	4 (1*s*)	5 (4*p*')
R_k	6.044821 E − 06	1.976755 E − 02	2.495013 E − 02	2.718132 E − 02	4.010913 E − 02
ρ_k	8.538629 E + 16	− 2.398938 E + 04	− 2.493072 E + 04	− 2.495351 E + 04	− 1.178013 E + 03
φ_k	1.568253 E + 07	5.692682 E + 03	3.229489 E + 03	2.749620 E + 03	2.058871 E + 03

6 (5*p*')	7 (3*d*')	8 (2*p*")	9 (2*s*)	10 (4*d*')
8.819474 E − 02	9.730951 E − 02	1.152137 E − 01	1.322567 E − 01	1.593048 E − 01
− 1.178838 E + 03	− 1.178857 E + 03	− 1.229677 E + 03	− 2.883314 E + 02	− 8.194135 E + 01
9.537326 E + 02	6.453641 E + 02	5.456497 E + 02	4.534934 E + 02	3.693735 E + 02

11 (3*d*")	12 (3*p*")	13 (3*s*)	14 (5*d*')	15 (4*f*')
3.631640 E − 01	3.976366 E − 01	4.055643 E − 01	5.576508 E − 01	6.666796 E − 01
− 8.288773 E + 01	− 3.206721 E + 01	− 9.278955 E + 00	− 2.121442 E + 00	− 2.125426 E + 00
1.591232 E + 02	9.911578 E + 01	9.210602 E + 01	7.048931 E + 01	4.916488 E + 01

16 (4*s*)	17 (4*p*")	18 (4*d*")	19 (4*f*")
1.142212 E + 00	1.201935 E + 00	1.362009 E + 00	2.000039 E + 00
− 2.559251 E + 00	− 2.238845 E + 00	− 1.413880 E + 00	− 4.674971 E − 01
2.374419 E + 01	1.448861 E + 01	1.208641 E + 01	6.934115 E + 00

20 (5*s*)	21 (5*p*")	22 (5*d*")	23 (6*s*)
3.548987 E + 00	4.231509 E + 00	8.140679 E + 00	1.675164 E + 01
− 3.367208 E − 02	− 2.299068 E − 02	− 4.085500 E − 03	− 1.015709 E − 04
2.477770 E + 00	1.132656 E + 00	2.642118 E − 01	1.480553 E − 02

k	1 (**80 Hg**)	2 (2*p*')	3 (3*p*')	4 (1*s*)	5 (4*p*')
R_k	5.821331 E − 06	1.947908 E − 02	2.452258 E − 02	2.682846 E − 02	3.921587 E − 02
ρ_k	9.681318 E + 16	− 2.494941 E + 04	− 2.593320 E + 04	− 2.595720 E + 04	− 1.231179 E + 03
φ_k	1.649075 E + 07	5.852996 E + 03	3.326914 E + 03	2.829128 E + 03	2.128635 E + 03

6 (5*p*')	7 (3*d*')	8 (2*p*")	9 (2*s*)	10 (4*d*')
8.550357 E − 02	9.549643 E − 02	1.135324 E − 01	1.303637 E − 01	1.549764 E − 01
− 1.232061 E + 03	− 1.232082 E + 03	− 1.285853 E + 03	− 3.020634 E + 02	− 8.655148 E + 01
9.986890 E + 02	6.726233 E + 02	5.633633 E + 02	4.671986 E + 02	3.841763 E + 02

11 (3*d*")	12 (3*p*")	13 (3*s*)	14 (5*d*')	15 (4*f*')
3.563975 E − 01	3.908226 E − 01	3.988730 E − 01	5.364145 E − 01	6.316740 E − 01
− 8.757939 E + 01	− 3.380894 E + 01	− 9.807862 E + 00	− 2.284060 E + 00	− 2.289033 E + 00
1.655741 E + 02	1.028348 E + 02	9.542193 E + 01	7.446016 E + 01	5.345713 E + 01

16 (4*s*)	17 (4*p*")	18 (4*d*")	19 (4*f*")
1.118616 E + 00	1.175167 E + 00	1.325003 E + 00	1.895022 E + 00
− 2.799053 E + 00	− 2.457940 E + 00	− 1.575308 E + 00	− 5.473941 E − 01
2.525985 E + 01	1.518807 E + 01	1.278284 E + 01	7.692339 E + 00

20 (5*s*)	21 (5*p*")	22 (5*d*")	23 (6*s*)
3.457738 E + 00	4.102389 E + 00	7.830668 E + 00	1.660763 E + 01
− 3.737423 E − 02	− 2.582468 E − 02	− 5.077650 E − 03	− 1.042362 E − 04
2.748177 E + 00	1.242705 E + 00	2.904978 E − 01	1.570841 E − 02

From the presented results one can drew following conclusions. In accordance with well-known ionization potential – atomic number relationship, quasi-classical atomic radius R_q reveals a quasi-periodic dependence upon the parameter Z with maxima at hydrogen H and typical metals (including all alkali elements) Li, Na, Al, K, Ga, Rb, Ag, In, Cs, Tl corresponding to the atomic ionization potentials' minima.

Schematic-plots of the obtained $\rho(r)$ and $-\varphi(r)$ functions in the step-like form are shown in **Figures 1** and **2**, respectively. Electric-charge-density reveals sharp and positive main maximum in the vicinity of center, which corresponds to the nucleus vibrations' region, broad negative minimum, which corresponds to the electron-density main maximum located at relatively short distance from the center, and a few extremes at relatively

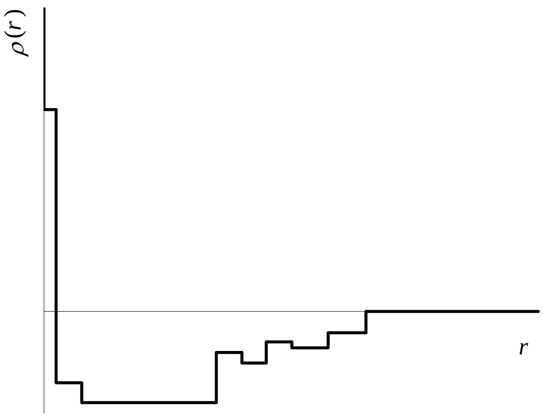

Figure 1. Schematic-plot of the electric-charge-density step-like radial distribution in atoms

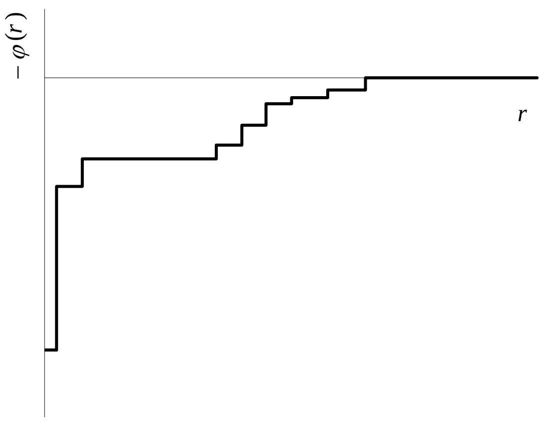

Figure 2. Schematic-plot of the electron-potential-energy step-like radial distribution in atoms

long distance, which are characteristic for the shell-structure of atoms. As for the electron-potential-energy-function, anywhere it is negative and monotonously rises. Thus, it posses only minimum at the center (an additional minimum may be revealed in effective-potential-function). Of course, behind the atomic radius both $\rho(r)$ and $-\varphi(r)$ functions in the step-like presentation are identically zero.

5. Accuracy of Binding-Energy and Electronic-Structure Calculations Based on Radial Step-Like Atomic Potentials

It is not out of place to consider accuracy of the binding energy and electronic-structure calculations carried out within the semiclassical approximation, *i.e.* on the basis of above introduced radial step-like atomic potentials. It is most convenient to estimate the method accuracy for Thomas-Fermi (TF) statistical semiclassical atomic model starting from the only analytical solution

$$\varphi(r) = \frac{81\pi^2}{8r^4} - F \tag{17}$$

of the TF equation. Here F is the Fermi-energy for intra-atomic electron gas, *i.e.* higher occupied electron level. Corresponding electron charge density is expressed by the function

$$\rho(r) = -\frac{243\pi}{8r^6} \tag{18}$$

As electron charge equals to -1 its potential energy in atom $U(r) = -\varphi(r) \to -1/r^4 \to -\infty$ when $r \to 0$. Then, inner turning point radius $r' = 0$ for any electron bound in TF "atom". As for the outer turning point radius r'' of the electron with energy $E \le F$, it can be found as only real positive root of the equation $E = U_{eff}(r)$, where $U_{eff}(r) = U(r) + l(l+1)/2r^2$ is the effective potential energy of the electron with orbital quantum number l, *i.e.*

$$E = F - \frac{81\pi^2}{8r^4} + \frac{l(l+1)}{2r^2} \tag{19}$$

Because differences between semiclassical electron energies are negligible if compared with their depth, one can suppose that approximately all of them coincide with Fermi-energy, $E = F$. In that case, the product $l(l+1)$ also should be substituted for its standard semiclassical expression $(l+1/2)^2$. As a result, we get

$$r'' = \frac{9\pi}{2l+1} \tag{20}$$

Consequently, averaged partial charge density of a l-electron-subshell equals to

$$\rho_l(r) = \frac{-1}{4\pi r''^3/3} = -\frac{(2l+1)^3}{972\pi^4} \tag{21}$$

and 0, respectively, inside and outside the r''-sphere.

As is known, when summation over the principal and orbital quantum numbers n and l characterizing electron motion in central-symmetric electric field is substituted for semiclassical integration the combinations $\nu = n - 1/2$ and $\lambda = l + 1/2$ serve as integration variables. As $l \le n-1$ the limit of integration over λ should be taken equal to $n - 1 + 1/2 = \nu$. As for the degeneracy factor, it equals to $2(2l+1) = 4\lambda$. Note that partial electron charge density takes on a nonzero value $-2\lambda^3/243\pi^4$ if $r \le r'' = 9\pi/2\lambda$. Consequently,

$\lambda \leq 9\pi/2r$. But, $\nu_{\max} = \lambda_{\max}$ and, then, the ratio $9\pi/2r$ should serve as the limit of integration over ν too.

Now we can found total electron charge density by means of semiclassical integration:

$$\rho_{Semiclassical}(r) = -\int_0^{\frac{9\pi}{2r}} d\nu \int_0^{\nu} d\lambda \; 4\lambda \; \frac{2\lambda^3}{243\pi^4} = -\frac{729\pi^2}{80r^6} \quad (22)$$

It yields semiclassical atomic potential in following form

$$\varphi_{Semiclassical}(r) = \frac{81\pi^2(90\pi^2)^{1/3}}{80r^4} - F \quad (23)$$

Variable parts of the obtained semiclassical expressions reveal same radial dependences ($\sim -1/r^6$ and $\sim 1/r^6$, respectively, for electron charge density and potential) as corresponding exact analytical solutions, but differ from them by the multipliers $3\pi/10$ and $(3\pi/10)^{2/3}$. Therefore, semiclassically determined structural and energy parameters are expected to be distinguished from their exact values by the multipliers of order of magnitude $\sim (10/3\pi)^{1/3} \approx 1.02 \sim 1$ and $\sim (3\pi/10)^{2/3} \approx 0.96 \sim 1$, respectively. Thus the estimated errors of the semiclassical approach make up a few percent. This conclusion is actually proved by the above cited calculations performed for some one-, two-, and three-dimensional real polyatomic structures.

6. Conclusions

Obtained results, numerically reflected in presented tables, vividly show that an effective method of parameterization of the intra-atomic electric field can by based on semiclassical approach. Such possibility follows from the Maslov criterion, according to which the exact and semiclassical atomic electron-energy spectra should be similar to each other irrespective of the atomic potentials' smoothness properties. Within the semiclassical approximation, intra-atomic eclectic charge density and electric field potential distributions can be presented by the step-like radial functions, where nucleus and electron-states classical turning point radii play role of the steps' limits, while charge density and potential inside a step are substituted for their volume averaged values. Superposition of the semiclassical atomic step-like radial potentials can serve as an initial approximation for the substance inner potential. Binding energy and electronic structure calculations based on such potential allow determining of the substance structural and energy parameters with relative accuracy making up a few percent, what is quite sufficient for materials science purposes.

7. Acknowledgment

Authors are very grateful to the Georgia National Science Foundation (GNSF) for the financial assistance (Grant #GNSF/ST08/4-411).

REFERENCES

[1] L. S. Chkhartishvili, "Selection of Equilibrium Configurations for Crystalline and Molecular Structures Based on Quasi-Classical Inter-Atomic Potential," *Transactions of the Global Transaction Unit*, Vol. 3(427), 1999, pp. 13-19.

[2] L. Chkhartishvili, D. Lezhava, O. Tsagareishvili and D. Gulua, "Ground State Parameters of B_2, BC, BN and BO Diatomic Molecules," *Transactions of the AMIAG*, Vol. 1, 2004, pp. 295-300.

[3] L. Chkhartishvili, D. Lezhava and O. Tsagareishvili, "Quasi-Classical Determination of Electronic Energies and Vibration Frequencies in Boron Compounds," *Journal of Solid State Chemistry*, Vol. 154, 2000, pp. 148-152.

[4] L. Chkhartishvili and D. Lezhava, "Zero-Point Vibration Effect on Crystal Binding Energy: Quasi-Classical Calculation for Laminated Boron Nitride," *Transactions of the Global Transaction Unit*, Vol. 6(439), 2001, pp. 87-90.

[5] L. Chkhartishvili, "Ground State Parameters of Wurtzite Boron Nitride: Quasi-Classical Estimations," *Proceedings of the 1st International Boron Symposium*, 2002, pp. 139-143.

[6] L. Chkhartishvili, "Quasi-Classical Approach: Electronic Structure of Cubic Boron Nitride Crystals," *Journal of Solid State Chemistry*, Vol. 177, 2004, pp. 395-399.

[7] L. S. Chkhartishvili, "Quasi-Classical Estimates of the Lattice Constant and Band Gap of a Crystal: Two-Dimensional Boron Nitride," *Physics of the Solid State*, Vol. 46, 2004, pp. 2126-2133.

[8] L. Chkhartishvili, Quasi-Classical Analysis of Boron-Nitride Binding," *Proceedings of the 2nd International Boron Symposium*, 2004, pp. 165-171.

[9] L. Chkhartishvili, "Quasi-Classical Analysis of Electron Bandwidths in Wurtzite-Like Boron Nitride," *Transactions of the IChTU*, Vol. 1, 2005, pp. 296-314.

[10] L. S. Chkhartishvili, "Analytical Optimization of the Lattice Parameter Using the Binding Energy Calculated in the Quasi-Classical Approximation," *Physics of the Solid State*, Vol. 48, 2006, pp. 846-853.

[11] L. Chkhartishvili, "Density of Electron States in Wurtzite-Like Boron Nitride: A Quasi-Classical Calculation," *Materials Science*: *An Indian Journal*, Vol. 2, 2006, pp. 18-23.

[12] L. Chkhartishvili, "Zero-Point Vibration Energy within Quasi-Classical Approximation: Boron Nitrides," *Proceedings of the Javakhishvili TSU* (*Physics*), Vol. 40, 2006, pp. 130-138.

[13] L. S. Chkhartishvili, "Equilibrium Geometry of the Boron Nitride Ultra-Small-Radius Nanotubes," *Material Science*

Copyright © 2010 SciRes.

of Nanostructures, Vol. 1, 2009, pp. 33-44.

[14] L. Chkhartishvili, "Boron Nitride Nanosystems of Regular Geometry," *Journal of Physics*: *Conference Series*, Vol. 176, 2009, p. 17.

[15] L. Chkhartishvili, "Equilibrium Geometries of the Boron Nitride Layered Systems," *Proceedings of the* 4*th International Boron Symposium*, 2009, pp. 161-170.

[16] L. Chkhartishvili, "Boron Nitride Nanosystems," In L. Chkhartishvili (Ed.), *Boron Based Solids*, Research Signpost, Trivandrum, 2010, in Press.

[17] L. Chkhartishvili, On Quasi-Classical Estimations of Boron Nanotubes Ground-State Parameters," *Journal of Physics*: *Conference Series*, Vol. 176, 2009, p. 9.

[18] L. Chkhartishvili, "Molar Binding Energy of the Boron Nanosystems," *Proceedings of the* 4*th International Boron Symposium*, 2009, pp. 153-160.

[19] L. Chkhartishvili, Nanotubular Boron: Ground-State Estimates," *Georgian International Journal of Science and Technology*, 2010, in Press.

[20] L. S. Chkhartishvili, D. L. Gabunia and O. A. Tsagareishvili, "Estimation of the Isotopic Effect on the Melting Parameters of Boron," *Inorganic Materials*, Vol. 43, 2007, pp. 594-596.

[21] L. S. Chkhartishvili, D. L. Gabunia and O. A. Tsagareishvili, "Effect of the Isotopic Composition on the Lattice Parameter of Boron," *Powder Metallurgy* & *Metal Ceramics*, Vol. 47, 2008, 616-621.

[22] D. Gabunia, O. Tsagareishvili, L. Chkhartishvili and L. Gabunia, "Isotopic Composition Dependences of Lattice Constant and Thermal Expansion of β-Rhombohedral Boron," *Journal of Physics*: *Conference Series*, Vol. 176, 2009.

[23] L. Chkhartishvili, "Isotopic Effects of Boron," *Trends in Inorganic Chemistry*, 2010, in Press.

[24] N. Bohr, "On the Constitution of Atoms and Molecules," *Philosophical Magazine*, Vol. 26, 1913, pp. 1-25.

[25] K. G. Kay, "Exact Wave Functions for Coulomb Problem from Classical Orbits," *Physical Review Letters*, Vol. 83, 1999, pp. 5190-5193.

[26] S. I. Nikitin and V. N. Ostrovskij "Problem of the Vibration-Rotation States in Two-Electron Atom," In V. N. Ostrovskij (Ed.), *Perturbation Theory in Atomic Calculations*, Nauka, Moscow, 1985, pp. 146-165.

[27] B. Baghchi and P. Holody, "An Interesting Application of Bohr Theory," *American Journal of Physics*, Vol. 56, 1988, pp. 746-747.

[28] T. Yamamoto and K. Kaneko, "Exploring a Classical Model of the Helium Atom," *Progress in Theoretical Physics*, Vol. 100, 1998, pp. 1089-1100.

[29] G. Tanner, K. Richter and J.-M. Rost, "The Theory of Two-Electron Atoms: Between Ground State and Complete Fragmentation," *Reviews of Modern Physics*, Vol. 72, 2000, pp. 497-544.

[30] K. M. Magomedov and P. M. Omarova, "Quasi-Classical Calculation of Electronic Systems," Dagestan Academy of Sciences Press, Makhachkala, 1989.

[31] M. Casas, A. Plastino and A. Puente, "Alternative Approach to the Semiclassical Description of *N*-Fermions Systems," *Physical Review A*, Vol. 49, 1994, pp. 2312-2317.

[32] D. Vrinceanu and M. R. Flannery, "Classical Atomic form Factor," *Physical Review Letters*, Vol. 82, 1999, pp. 3412-3415.

[33] A. Jaroń, J. Z. Kamiński and F. Ehlotzky, "Bohr's Correspondence Principle and *X*-Ray Generation by Laser-Stimulated Electron–Ion Recombination," *Physical Review A*, Vol. 63, 2001, p. 4.

[34] M. I. Petrashen, "On Semiclassical Method of Solving of the Wave Equation," *Proceedings of the Leningrad State University* (*Series of Physical Sciences*), Vol. 7, 1949, pp. 59-78.

[35] R. Gaspar, I. I. Glembotskij, I. Y. Petkyavichyus and A. P. Yutsis, "Quantum Numbers and Universal Potential," In A. P. Yutsis (Ed.), *Theory of Atoms and Atomic Spectra*, I., Latvian State University, Riga, 1974, pp. 54-58.

[36] B. Rohwedder and B.-G. Englert, "Semiclassical Quantization in Momentum Space," *Physical Review A*, Vol. 49, 1994, pp. 2340-2346.

[37] M. G. Veselov and L. N. Labzovskij, "Atomic Theory, Electron Shell Structure," Nauka, Moscow, 1986.

[38] R. Sakenshaft and L. Spruch, "Semiclassical Evaluation of Sums of Squares of Hydrogenic Bound-State Wave Functions," *Journal of Physics B*, Vol. 18, 1985, pp. 1919-1925.

[39] J. Tao and G. Li, "Approximate Bound to the Average Electron Momentum Density for Atomic Systems," *Physica Scripta*, Vol. 58, 1998, pp. 193-195.

[40] K. M. Magomedov, "On Quasi-Classical Self-Consistent Atomic Field," *Proceedings of the USSR Academy of Sciences*, Vol. 285, 1985, pp. 1110-1115.

[41] A.-N. Popa, "Accurate Bohr-Type Semiclassical Model for Atomic and Molecular Systems," *Reports of the Institute of Atomic Physics*, Vol. E12, 1991, pp. 1-90.

[42] J. N. L. Connor, "Semiclassical Theory of Elastic Scattering," In M. S. Child (Ed.), *Semiclassical Methods in Molecular Scattering and Spectroscopy*, Reidel Publishing, Dordrecht–Boston–London, 1979, pp. 45-107.

[43] R. J. le Roy, "Applications of Bohr Quantization in Diatomic Molecular Spectroscopy," In M. S. Child (Ed.), *Semiclassical Methods in Molecular Scattering and Spectroscopy*, Reidel Publishing, Dordrecht–Boston–London, 1979, pp. 109-126.

[44] H. Kuratsuji, "Semiclassical Asymptotics for Fermions Systems Based on the Coherent-State Path Integral," *Physics Letters A*, Vol. 108, 1985, pp. 139-143.

[45] J.-T. Kim, "Semiclassical Wentzel-Kramers-Brillouin (WKB) Method for Generating the Potential Energy Curve and the Therm Energies of Diatomic K_2 Molecule," *The Journal of the Korean Physical Society*, Vol. 35, 1999, pp. 168-170.

[46] A. G. Magner, S. N. Fedotkin, F. A. Ivanyuk, P. Meier and M. Brack, "Shells and Periodic Orbits in Fermions Systems," *Czechoslovak Journal of Physics*, Vol. 48, 1998, pp. 845-852.

[47] J. Marañon, "Path Integral's Semiclassical Quantification," *Quantum Chemistry*, Vol. 52, 1994, pp. 609-616.

[48] K. Sohlberg, R. E. Tuzun, B. G. Sumpter and D. W. Noid, Full Three-Body Primitive Semiclassical Treatment of H_2^+," *Physical Review A*, Vol. 57, 1998, pp. 906-913.

[49] F. Remacle and R. D. Levine, "On the Classic Limit for Electronic Structure and Dynamics in the Orbital Approximation," *Journal of Chemical Physics*, Vol. 113, 2000, pp. 4515-4523.

[50] W. A. Fedak and J. J. Prentis, "Quantum Jumps and Classical Harmonics," *American Journal of Physics*, Vol. 70, 2002, pp. 332-344.

[51] A. G. Chirkov and I. V. Kazanets, "Classical Physics and Electron Spin," *Technical Physics*, Vol. 45, 2000, pp. 1110-1114.

[52] M. Madhusoodanan and K. G. Kay, "Globally Uniform Semiclassical Wave-Function for Multidimensional Systems," *Journal of Chemical Physics*, Vol. 109, 1998, pp. 2644-2655.

[53] G. V. Shpatakovskaya, "Quasi-Classical Description of Electronic Super-Shells in Simple Metal Clusters," *JETP Letters*, Vol. 70, 1999, pp. 334-339.

[54] G. V. Shpatakovskaya, "Quasi-Classical Analysis of the Spectra of Two Groups of Central Potentials," *JETP Letters*, Vol. 73, 2001, pp. 268-270.

[55] M. Brack, "The Physics of Simple Metal Clusters: Self-Consistent Jellium Model and Semiclassical Approaches," *Reviews of Modern Physics*, Vol. 65-I, 1993, pp. 677-732.

[56] V. P. Maslov, "Perturbation Theory and Asymptotic Methods," Moscow University Press, Moscow, 1965.

[57] L. Chkhartishvili, "Quasi-Classical Theory of Substance Ground State," Technical University Press, Tbilisi, 2004.

[58] C. Froese–Fischer, "The Hartree–Fock Method for Atoms, A numerical approach," Wiley, New York, 1977.

Copyright © 2010 SciRes.

J. Electromagnetic Analysis & Applications, **2010, 2: 244-251**
doi:10.4236/jemaa.2010.24030 Published Online April 2010 (http://www.SciRP.org/journal/jemaa)

Scientific Research

Utilization of Energy Capacitor Systems in Power Distribution Networks with Renewable Energy Sources

Yaser Soliman Qudaih, Takashi Hiyama

Computer Science and Electrical Engineering Department, Kumamoto University, Kumamoto, Japan.
Email: Yaser_qudaih@yahoo.com

Received December18th, 2009; revised February 11th, 2010; accepted February15th, 2010.

ABSTRACT

The impact of power fluctuation caused by renewable sources is highly negative. This article discusses the idea of an energy capacitor system (*ECS*) *which regulates the power balance in a distribution system based on Multi-Agent System* (*MAS*)*. Energy Capacitor system as a storage device plays the main role to control the system's power quality by absorbing the fluctuations. Load Following Operation* (*LFO*) *process and coordination control scheme between the ECS and diesel generator have been introduced. Results show the efficient utilization of the ECS based on a special index defined in this paper to evaluate the power fluctuations in the distribution system. The results also show the useful implementation of the control scheme by revealing the capability of keeping the ECS stored energy in the specified range.*

Keywords**:** *Energy capacitor system, Load following operation, Multi agents, Distributed Generation*

1. Introduction

Utilization of Distributed Generation to power distribution system has been rabidly increased. Such a technology has been presented strongly in the top of many researches in the field of power system [1,2]. However, deregulation of electrical utilities, environmental concerns and globalization could be the main reasons behind such phenomena. Using small and clean distributed power sources, such as photovoltaic, wind energy, fuel cells and energy capacitor devices, became a vital need to withstand the burdens of technological race. Providing an integrated performance and flexibility of the power system, is an urgent need to be implemented especially in the presence of uncontrollable and environmentally dependant power sources.

Previous studies explained the situation when dealing with distribution systems in the presence of distributed generation [3-5]. Optimum sizing and placement is one of the most important aspect regarding to dispersed sources [3]. Acharia *et al.* discussed analytically the allocation of distributed generation in primary distribution network [4], others achieved to find the optimal allocation for reliability, losses, and voltage improvement [5], and others discussed about the distributed generation contribution to primary frequency control [6]. It is however, the impact of distributed generation makes the system very sensitive to perturbations.

In this paper, the ECS as a new technology of energy saving is proposed to be utilized in power distribution system. Thus, many other applications of the capacitors and ultra capacitors have been reviewed in order to make the study more comprehensive. Okamura [7] introduced the ECS in a basic study; however, overall characteristics have been discussed. It has been noticed that ECS applications are rapidly increased such as [8-11].

In this work, the control scheme based on the coordination between the ECS and the DG, as controllable devices, has been proposed together with multi-agents and computer network utilization which is widely used application. The influence of the computer network failure has been checked and treated in proper way. PI and PID controllers have been used to solve the problem of ECS size limitation and to complete the coordination process.

Nomenclature:
PV: Photovoltaic; DG: Diesel generator; WTG: Wind turbine generator V_a, V_b, and V_c: Nominal line voltages; I_a, I_b, and I_c: Currents injected; P_{up}: Power from the upper system; P_{ecs}: Power from the ECS unit; E_{ecs}: ECS Stored energy; P_{dg}: Power from the diesel unit; P_{pv}: Total output from PV units; P_{wt}: Total output from wind turbine; DP_{set}: Control Signal to the diesel generator; P_{target}: Upper system target power; $P_{ref.}$: Monitored power from upper system.

Copyright © 2010 SciRes.

A long process of parameters and gains tuning has been hold based on trial and error methodology. Yet, further studies in the control strategies are ongoing, such as [12], where intelligent controllers, namely fuzzy logic switching have been utilized.

Medium tension Power distribution system as a very important and sensitive part of the total power system, which links the transmission and consumers, also supplies many industries and other vital parts and utilities, has been discussed. **Table 1** shows the 30-bus 12.66 kV power distribution system data [13]. Unlike many other cases such as in [14-15], the study in this work and the related simulations have discussed more details of the distributed generation effect via using dynamic models of the DG and the WTG.

2. Model Description

Figure 1 shows the Single line diagram of the target system also the main diagram of the Matlab/Simulink representation. In the single line diagram, dotted lines are representing tie lines. However, the simulation has been made with all tie lines open to represent the base case according to [12].

The dispersed sources added to the system are DG, WTG and PV including the ECS as a storage device, such a model can be considered as a flexible tool to implement several applications to the distribution system such as reconfiguration [16] and distributed generation allocation [17]. The mathematical expressions of using the components in the distribution system are expressed by the concept of connecting any device to the distribution network. In our case the three phase voltage from the distribution system is used as an input and the output will be the current injected to the system. That can be explained as follow:

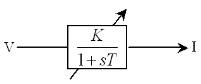

where, V = $[v_a, v_b, v_c]^T$ and I = $[i_a, i_b, i_c]^T$;

Table 1. The 33-bus distribution system data

			Load at receiving end	
Line no.	**Resistance (Ω)**	**Reactance (Ω)**	**Real power(MW)**	**Reactive power (MVAr)**
1	0.0922	0.0477	0.1	0.6
2	0.493	0.2411	0.09	0.04
3	0.366	0.1864	0.12	0.08
4	0.3811	0.1941	0.06	0.03
5	0.819	0.707	0.06	0.02
6	0.1872	0.6188	0.2	0.1
7	1.7114	1.2351	0.2	0.1
8	1.03	0.74	0.06	0.02
9	1.04	0.74	0.06	0.02
10	0.1966	0.065	0.045	0.03
11	0.3744	0.1238	0.06	0.035
12	1.468	1.155	0.06	0.035
13	0.5416	0.7129	0.12	0.08
14	0.591	0.526	0.06	0.01
15	07463	0.545	0.06	0.02
16	1.289	1.721	0.06	0.02
17	0.732	0.574	0.09	0.04
18	0.164	0.1565	0.09	0.04
19	1.5042	1.3554	0.09	0.04
20	0.4095	0.4784	0.09	0.04
21	0.7089	0.9373	0.09	0.04
22	0.4512	0.3083	0.09	0.05
23	0.898	0.7091	0.42	0.2
24	0.896	0.7011	0.42	0.2
25	0.203	0.1034	0.06	0.025
26	0.2842	0.1447	0.06	0.025
27	1.059	0.9337	0.06	0.02
28	0.8042	0.7006	0.12	0.07
29	0.5275	0.2585	0.2	0.6
30	0.9744	0.963	0.15	0.07
31	0.3105	0.3619	0.21	0.1
32	0.341	0.5302	0.06	0.04

Substantion voltage-12.66Kv.

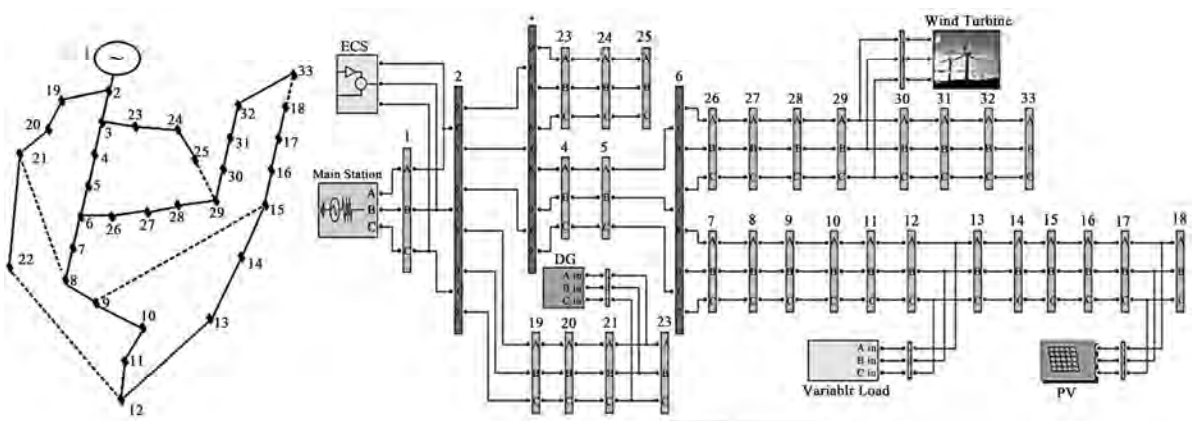

Figure 1. Single line diagram and Matlab/Simulink model representation of the distribution system

$$i_a = \frac{K}{1+sT} v_a \quad , \; i_b = \frac{K}{1+sT} v_a \quad and \quad i_c = \frac{K}{1+sT} v_a$$

In case of PV the factor K is always +ve ($K > 0$).

In case of variable Load, factor K is always -ve ($K < 0$).

In case of ECS, the factor K can be controlled to determine the charging/discharging operation of the ECS as If $K > 0$ represents Discharging operation and if $K < 0$ represents Charging operation.

The elements of the model are further explained as follow:

2.1 DG Model

Synchronous machine per-unit standard (pu), 5000 kW maximum rated power, 60 Hz and 12.66 kV dynamical model has been used. The configuration of the mathematical expression used to model the synchronous generator is shown in **Figure 2**.

Where Pto is the mechanical input to the generator, Pe is the electrical output of the generator, δ is the phase difference angle, H is the inertia constant and D is the damping coefficient. The Matlab/Simulink block diagram of the synchronous generator together with the governing system is shown in **Figure 3**. Where Pm is the Mechanical power at the machine's shaft and Vf is the field voltage.

2.2. WTG model

In the literature, several studies have been reported regarding wind turbines and wind power driven generators [18]. The model proposed in this paper is a squirrel cage induction generator based of the wind speed versus wind turbine output power characteristics. The power extracted from wind is given by the following Equation

$$P_{WT} = \frac{\rho . A}{2} V_{wind}^{3} \tag{1}$$

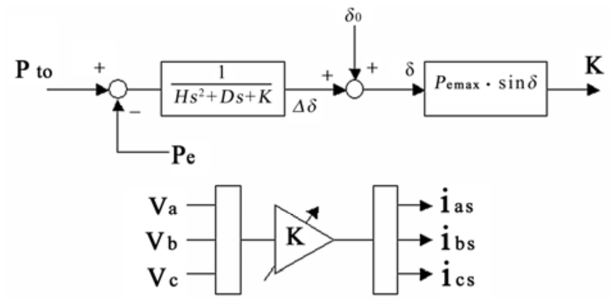

Figure 2. Mathematical model of the synchronous generator

where; ρ : Air density, kg /m^3 A: Turbine swept area, m^2 and V_{wind} : Wind speed, m/s.

Mathematical relation for mechanical power extraction form the WTG can be expressed as follows [19,20].

$$P_m = C_p(\lambda, \beta).P_{WT} \tag{2}$$

where; λ : Tip speed ratio, β : Blade pitch angle, Degree. $C_p(\lambda,\beta)$: Performance coefficient of the turbine.

The coefficient of performance is not constant, but varies with tip speed ratio; λ. A generic equation is used to model C_p as shown in the following equation:

$$C_p(\lambda, \beta) = c_1(\beta)\lambda^2 + c_2(\beta)\lambda^3 + c_3(\beta)\lambda^4 \tag{3}$$

This equation, based on the wind turbine characteristics and the coefficients c_1, c_2 and c_3 are determined according to Simulink model of the wind turbine which has been modified as phasor type induction generator. The tip speed ratio can be obtained from the following equation:

$$\lambda = \frac{R.\omega}{V_{wind}} \tag{4}$$

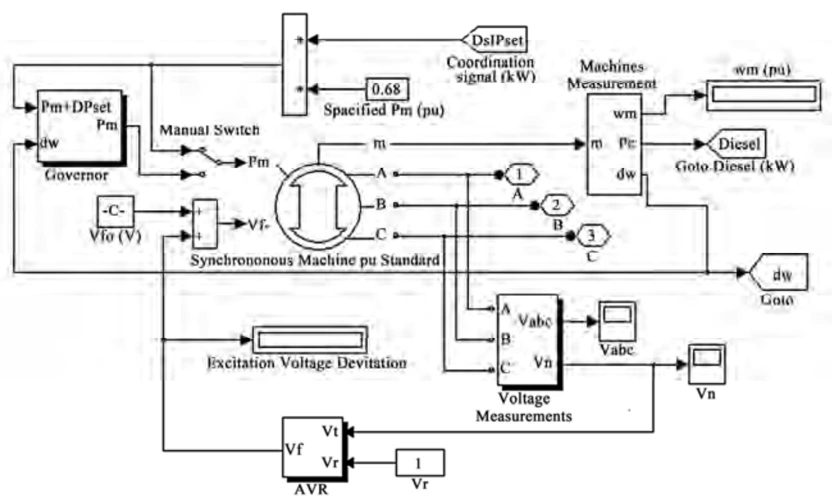

Figure 3. Matlab block diagram of the DG connections

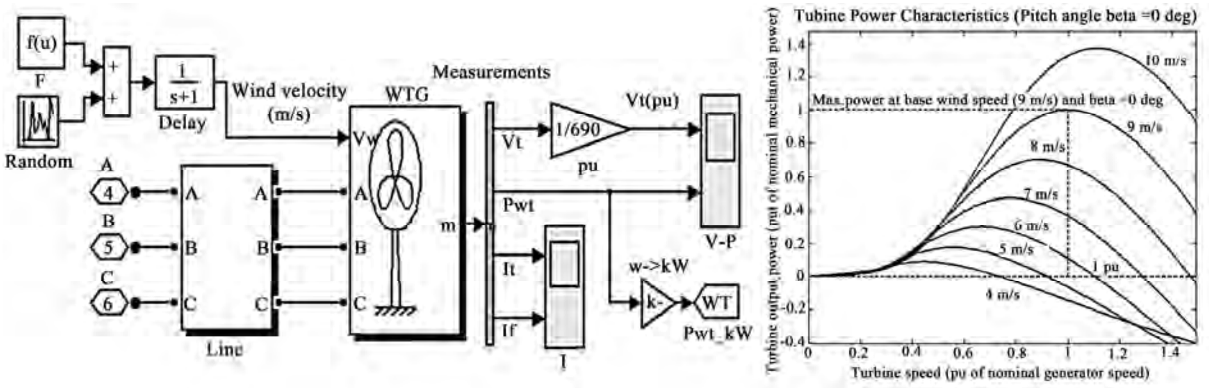

Figure 4. Matlab/Simulink representation of connecting the wind turbine model (to the left) and power characteristics of the WTG (to the right)

where, R is radius of the wind turbine and ω is the wind turbine rotation speed. The electrical power generated by the WTG was defined as follows

$$P_e = \eta_m \cdot \eta_g \cdot p_m \tag{5}$$

where; η_m: Mechanical efficiency. η_g: Generator efficiency.

For this paper, three phase instantaneous dynamical model has been constructed. **Figure 4** illustrates the Simulink block diagram of connecting the wind turbine to the system. It also shows the power characteristics of the wind turbine generator. The power characteristics diagram indicates that the model is an induction fixed speed wind generator based on Equations (1) to (5).

2.3 PV System Model

To represent the fluctuations caused by PV technology and according to the way the network has been constructed, a simplified mathematical model based on transfer function has been used, also for the sake of simplicity, the PV model has been made considering the AC side of the PV model. Meanwhile, random variations to model the insolation have been considered with suitable gains and time delay, using Matlab/Simulink. Three phase voltages taken from the line data transferred to the three phase currents injected to the network. Then the power is calculated by multiplying voltage and current as shown in **Figure 5**.

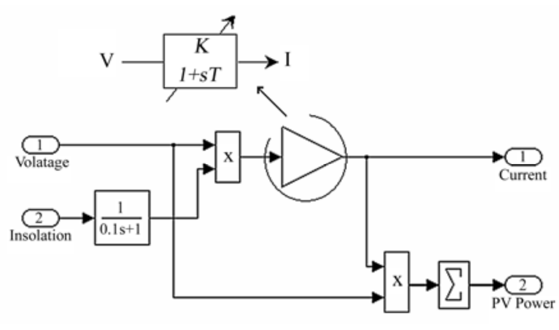

Figure 5. Mathmatical expression of PV model

2.4 ECS Model

Energy Capacitor System (ECS) consists of capacitors and power electronics. It is used as an energy storage system. The capacitor part of the ECS is a group of electric double layer capacitors of increased energy density. The AC side of the three-phase instantaneous model is considered in this paper. Similar model of the PV system has been considered with controlled factor K. Charging and discharging operation of the ECS is utilized for LFO control. **Figure 6** shows the charging and discharging operation concept with the limitations of having fully charged or fully discharged conditions. Keeping thecharging/discharging operation in the specified range vitally depends on the DG support and using the suitable controllers. The charging and discharging level of the ECS was specified from 0.5 kWh to 2.5 kWh in this work.

2.5 Variable Load Model

Although the fluctuations in power caused by the PV system and by the WTG are enough to cause the perturbations required to check the ECS efficiency, a variable load has been considered to make the system more realistic. The same model explained earlier in Section 2 has been used as simplified model of current injection with negative factor K. Ramp changes in the load have been considered during the simulation as shown in **Figure 7**. However, random, periodical and step changes in the variable load have been also checked giving the same result but, ramp changes in the variable load could be more realistic according to the time scale used in this paper. Also, ramp changes in the load are more severe to check the efficiency of the saving device (ECS) and the success of the control scheme in coordinating between the diesel Generator and the ECS.

3. Working Criteria

As the system is connected to infinite bus and because of the renewable energy sources that scattered around, the big concern is about keeping the power delivered from

Copyright © 2010 SciRes.

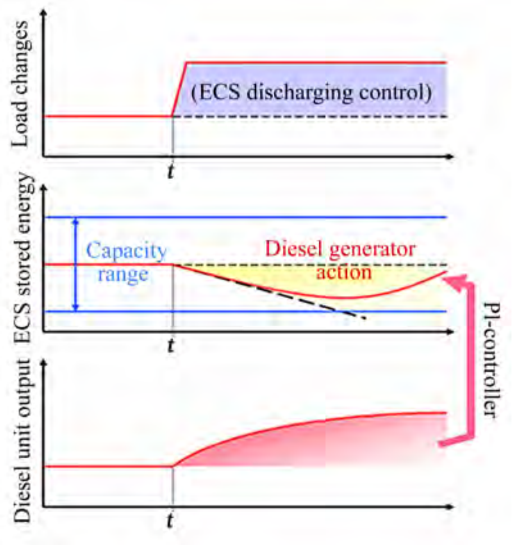

Figure 6. ECS charging/discharging operation concept

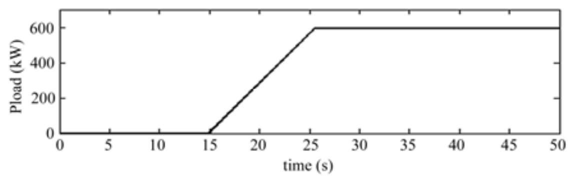

Figure 7. Ramp variable load

the upper system as much as regulated as possible. It should be regulated, to satisfy the consumer's demand of good quality of power and to overcome the consequences of power fluctuations. Thus LFO is considered as follow:

3.1 Load Following Operation

With utilizing ECS, multi-agents based LFO of two levels, global and local, are performed to keep the real power supplied from the upper system regulated. The multi-agents system is a computer network consists of several personal computers called agents, are responsible about sending and receiving data among each others to perform the control strategy and provide the coordination scheme between elements of the system, namely the ECS and the DG. Those agents are divided into three parts:

- **Monitoring agent** has the mission of measuring the data required from one part of the system and supply it through the computer network to the supervisor agent.
- **Supervisor agent** plays the mission of coordination among the controllable devices in the system, it is obviously provided with the suitable algorithm and control strategy in order to send the required data to the control agent.
- **Control agent** has the mission of applying the control signal via sending it to the desired equipment which is the DG in this case. DG will act according to the control value to support the ECS which is small in size but fast in charging and discharging.

Figure 8 shows the utilization of multi-agents and computer network, where the data files X and Y prepared at the monitoring agent which is PC1. Hard drives F and G of PC2 and PC3 receive data from PC1 respectively (PC2 is the supervisor agent and PC3 is the control agent). After that, PC2 inputs the data X received from PC1 and prepare the data file Z to be sent to PC3. PC3 reads the data file Z and prepare the control action.

A small scale computer network (LAN) has been constructed at the laboratory to evaluate MAS utilization. In addition, analogue simulations have been performed with real time simulator which is available at Kyushu Power Company-Japan.

Analogue to digital convertor **A/D** and digital to analogue converter **D/A** including Digital signal processing board **DSP** are used to perform the multi-agent based control action. **Figure 9** shows a part of the analogue simulation process.

3.2 Global Control

Global control or upper level control is performed when

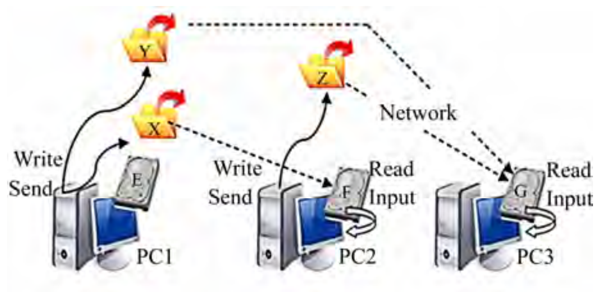

Figure 8. Multi-agents and computer network utilization

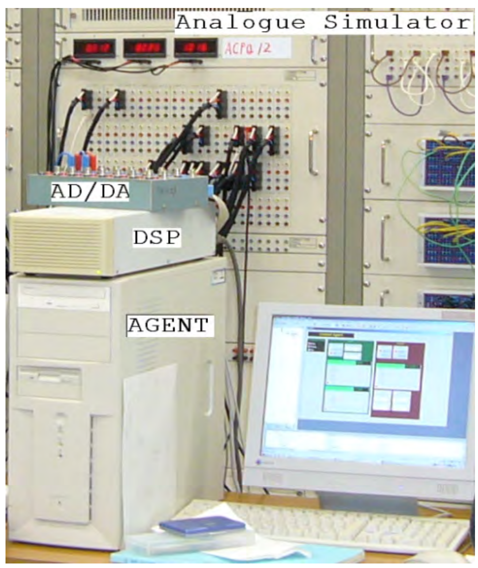

Figure 9. Analogue simulator interfacing process

computer network is available and able to communicate between the ECS and the DG whom are controllable devices. These two devices can be efficiently coordinate to overcome the fluctuations in power caused by the WTG and the PV system. In case of the global control the DG receives the required signal from the ECS through the agents to absorb the fluctuations. The ECS itself has unique characteristics and can compensate any lack in power or absorb any higher generation, through the fast charging and discharging operation. However, the limited size of the ECS causes a constraint which be avoided by getting the support of the DG. As the ECS and the DG are not at the same location, MAS has been utilized.

3.3 Local Control

This case happens when the computer network fails down due to any reason, in other words, the DG and the ECS system are not coordinated during this period of time. The performance of the energy capacitor system is clearly degraded and the DG cannot perform the LFO itself. Another technique has been used in this situation by modifying the target power to a certain accepted value to improve the performance of the ECS. The local information in the location of the ECS has been implemented. That is called the lower or local control.

4. Results and Discussion

Based on trial and error methodology, the parameters of the PI controllers have been tuned until the optimum values obtained. **Table 2** exposes the tuned parameters according different strategies.

Figures 10-12 illustrate the results according to those strategies. In a comparison between the three graphs, from **Figure 10** the ECS is not in service and no control action is performed which results in a very fluctuated and distorted power delivery from the upper system. Next graph, **Figure 11** illustrates the global control condition where both the DG and the ECS are coordinated with each others, which results in a high level of regulated real power. The last graph **Figure 12** shows the local control where the DG is not supporting the ECS due to computer network failure. The power from the upper system has been modified in this case to maintain the saved energy of the ECS in the required specified level. Comparing the

Table 2. Controller tuned parameters for LFO

Strategy	Parameters	On the ECS	On the DG	Coordination controller
Global control parameters	P I Gain	0.25 100 1	6 0.1 0.001	0.0125 0.00005 -
Local control parameters	P I Gain	0.25 1000 0.005	6 0.1 0.001	0.0125 0.00005 -

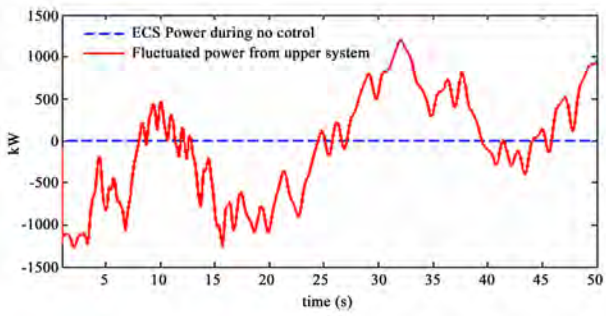

Figure 10. Real power from the ECS and from the system without control

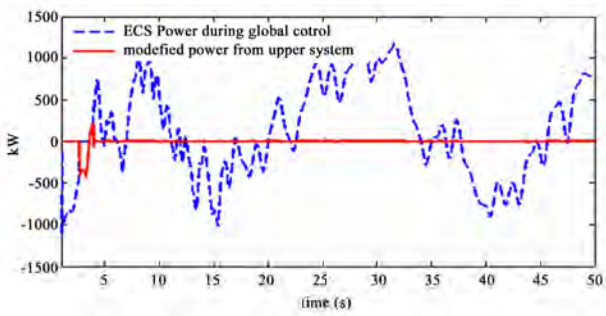

Figure 11. Real power from the ECS and from the system in global control

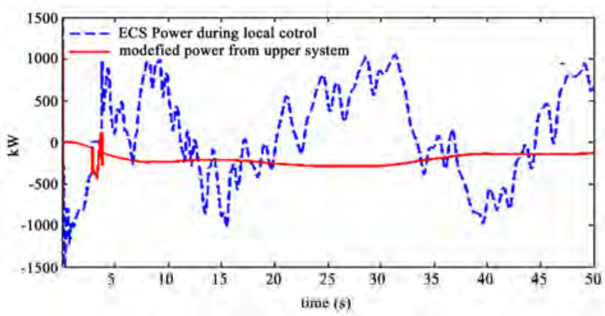

Figure 12. Real power from the ECS and from the system in local control

Figures 10 and **11**, we can understand the efficiency of the ECS. Meanwhile, comparing the **Figures 11** and **12**, we can understand the efficiency of the Multi-agent control scheme.

The evaluation index is expressed in Equation (6) where the averaged power is calculated to investigate the power deviation from the upper system of the described distribution network and to evaluate the LFO scheme for every strategy [21].

$$Index = \frac{\sum |P_{up} \quad P_t|}{N} \tag{6}$$

where P_{up} is the power from the upper system, P_t the target

Copyright © 2010 SciRes.

power, and N is the number of entered data. The obtained indices according to the different control strategy are shown in **Table 3** (The smaller the index, the better the result).

The coordination scheme between the DG and the ECS results in a proper operation of the ECS, in other words to keep the stored Energy of the ECS in a certain desired level, the support from the DG is required. Simulation results shown in **Figure 13** show that the trajectory of the DG output is opposite to the ECS stored energy trajectory. The verification of this result is simply done by checking the index of the upper system power. If the saving energy of the ECS is over or under the desired limit, the index will be very high and the ECS will stop working. As shown in **Figure 12**, in the period from 3 to 4.2 seconds the ECS stopped because of the over saturation in the saved energy due to size limitation of the ECS. By using the suitable controller and suitable coordination scheme, this phenomenon has been eliminated and contentious control action can be achieved.

The coordination scheme between the DG and the ECS results in a proper operation of the ECS, in other words to keep the stored Energy of the ECS in a certain desired level, the support from the DG is required. Simulation results shown in **Figure 13** show that the trajectory of the DG output is opposite to the ECS stored energy trajectory. The verification of this result is simply done by checking the index of the upper system power. If the saving energy of the ECS is over or under the desired limit, the index will be very high and the ECS will stop working. As shown in **Figure 12**, in the period from 3 to 4.2 seconds the ECS stopped because of the over saturation in the saved energy due to size limitation of the ECS. By using the suitable controller and suitable coordination scheme, this phenomenon has been eliminated and contentious control action can be achieved.

Table 3. LFO indices for different control strategy

CONTROL STRATEGY	INDEX
No control	308.438 kW
Global control	6.511 kW
Local control	187.091 kW

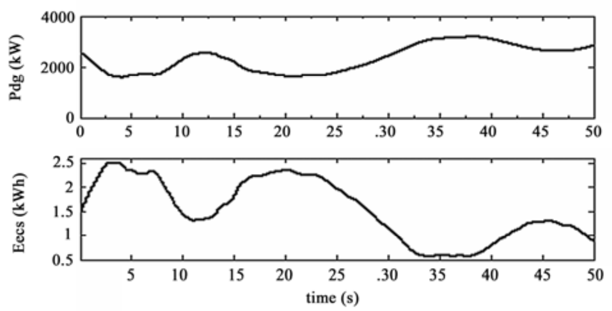

Figure 13. Coordination scheme illustrations

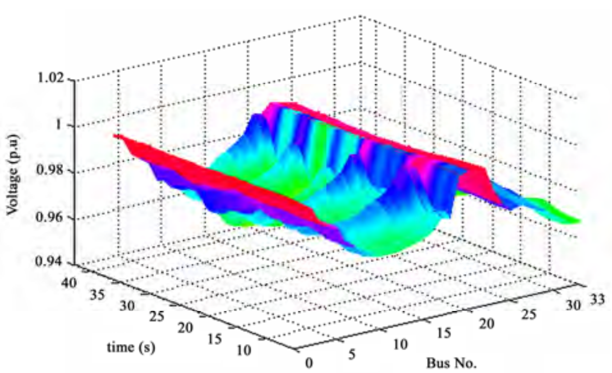

Figure 14. Voltage profile at every node of the system

5. Conclusions

Two main objectives have been achieved from this article. The first one is to show the efficient utilization of the ECS as a new technology in power distribution system. The second one is to show the efficiency of the control scheme and the utilization of MAS. The ECS can absorb all the fluctuations in real power caused by renewable energy sources with size limitations. DG cannot absorb such fluctuations due to technical limitations. The scheme in this article provides coordination between the two devices. Results show an efficient usage of the scheme, an efficient utilization of MAS and applicable implementation of ECS. All of all, with the ECS and the suitable control scheme the consequences of fluctuated power are highly avoided.

REFERENCES

[1] G. Pepermans, J. Driesen, D. Haeseldonckx, R. Belmans and W. Dhaeseleer, "Distributed Generation: Definition, Benefits and Issues," *Energy Policy*, Vol. 33, No. 6, 2005, pp. 787-798.

[2] W. El-Khattam and M. M. A. Salama, "Distributed Generation Technologies, Definitions and Benefits," *Electric Power System Research*, Vol. 71, No. 2, 2004, pp. 119-128.

[3] R. K. Singh and S. K. Goswami, "Optimum Siting and Sizing of Distributed Generations in Radial and Networked Systems," *Electric Power Components and Systems*, Vol. 37, No. 2, 2009, pp. 127-145.

[4] N. Acharia, P. Mahat and N. Mithulananthan, "An Analytical Approach for DG Allocation in Primary Distribution Network," *Electrical Power and Energy Systems*, Vol. 28, No. 6, 2006, pp. 669-678.

[5] C. L. T. Borges and D. M. Falcao, "Optimal Distributed Generation Allocation for Reliability, Losses, and Voltage Improvement," *Electrical Power and Energy Systems*, Vol. 28, No. 6, 2006, pp. 413-420.

[6] J. Morren, S. W. H. De Haan and J. A. Ferreira, "Contribution of DG Units to Primary Frequency Control," *Euro-*

pean Transaction on Electrical Power, Vol. 16, No. 5, 2006, pp. 507-521.

[7] M. Okamura, “A Basic Study on Power Storage Capacitor System,” *IEEJ Transactions on Power and Energy*, in Japanese, Vol. 115, 1995, pp. 504-510.

[8] C. Abbey and G. Joos, “Super Capacitor Energy Storage for Wind Energy Applications,” *IEEE Transactions on Industry Applications*, Vol. 43, No. 3, 2007, pp.769-776.

[9] S. M. Muyeen, S. Shishido, A. Mohd Hasan, R. Takahashi, T. Murata and J. Tamura, “Application of Energy Capacitor System to Wind Power Generation,” *Wind energy*, Vol. 11, No. 4, 2007, pp. 335-350.

[10] T. Kinjo, T. Senjyu, K. Uezato and H. Fujita., “Output Leveling of Wind Power Generation System by EDLC Energy Storage System,” *Electrical Engineering in Japan*, Vol. 154, No. 4, 2006, pp. 34-41.

[11] K. Shinohara, K. Yamamoto, K. Iimori, Y. Yanagita and Y. Gosho, “Performance and Maximum Load Capacity of Uninterruptible Power System Using Double-Layer Capacitor,” *Electrical Engineering in Japan*, Vol. 1541, No. 3, 2005, pp.73-81.

[12] T. Hiyama, K. Tomsovic, E. Anami, S. Yamashiro, M. Yamagishi and M. Shimizu, “Experimental Studies on Fuzzy Logic Stabilization Control for Energy Capacitor System,” *Proceedings of IEEE ISAP Conference*, Budapest, 2001.

[13] E. Baran Mesut and F. W. Felix, “Network Reconfiguration in Distribution System for Loss Reduction and Load Balancing,” *IEEE Transactions on Power Delivery*, Vol. 4, No. 2, 1989, pp. 1401-1407.

[14] C. Joon-Ho and K. Jae-Chul, “Network Reconfiguration at the Power Distribution System with Dispersed Generation for Loss Reduction,” *Power Engineering Society Winter Meeting*, Vol. 4, 2000, pp. 2363-2367.

[15] M. Juan Andrés and G. Antonio José, “A New Heuristic Approach for Distribution Systems Loss Reduction,” *Electric Power Systems Research*, Vol. 78, No. 11, 2008, pp. 1953-1958.

[16] H. M. Khodr, J. Martínez-Crespo, Z. A. Vale and C. Ramos, “Optimal Methodology for Distribution Systems Reconfiguration Based on OPF and Solved by Decomposition Technique,” *European Transactions on Electrical Power*, Research Article, 22 January 2009.

[17] M. F. AlHajri and M. E. El-Hawary, “Improving the Voltage Profiles of Distribution Networks Using Multiple Distribution Generation Sources,” *Conference on Power Engineering*, Vol. 10, No. 12, 2007, pp. 295-299.

[18] H. Li and Z. Chen, “Overview of Different Wind Generator Systems and Their Comparisons,” *IET Renewable Power Generation*, Vol. 2, No. 2, 2008, pp. 123-138.

[19] G. L. Johnson, “Wind Energy Systems,” Prentice-Hall, New Jersey, 1985.

[20] E. Muljadi, C. Wang and M. H. Nehrir, “Parallel Operation of Wind Turbine, Fuel Cell, and DG Sources,” *IEEE Power Engineering Society General Meeting*, Vol. 2, 2004, pp. 1927-1932.

[21] Y. Qudaih and T. Hiyama, “Reconfiguration of Power Distribution System Using Multi Agent and Hierarchical Based Load Following Operation with Energy Capacitor System,” *Proceedings of 8th International Power Engineering Conference*, Singapore, December 2007, pp. 223-227.

Copyright © 2010 SciRes.

J. Electromagnetic Analysis & Applications, 2010, 2: 252-257
doi:10.4236/jemaa.2010.24031 Published Online April 2010 (http://www.SciRP.org/journal/jemaa)

Study on Axial Flux Hysteresis Motors Considering Airgap Variation

Mohammad Modarres, Abolfazl Vahedi, Mohammadreza Ghazanchaei

Electrical Engineering Department Iran University of Science and Technology, Centre of Excellence for Power Systems Automation and Operation, Tehran, Iran.
Email: mohamamdmodarees@ieee.org

Received November 24th, 2009; revised January 12th, 2010; accepted January 18th, 2010.

ABSTRACT

Axial flux hysteresis motor (*AFHM*) *is self-starting synchronous motor that uses the hysteresis characteristics of magnetic materials. It is known that the magnetic characteristics of hysteresis motor could be easily affected by air gap and structure dimensions variation. Air gap length plays an important role in flux distribution in hysteresis ring and influences the output torque, terminal current, efficiency and even optimal value of other structural parameters of AFHM. Regarding this issue, in this study effect of air gap variation on performance characteristics of an axial flux hysteresis motor and effect of air gap length on hysteresis ring thickness and stator winding turns is investigated. Effect of air gap length on electrical circuit model is perused. Finally, simulation of AFHM in order to extract the output values of motor and sensitivity analysis on air gap variation is done using* 3*D-Finite Element Model. Hysteresis loop in the shape of an inclined ellipse is adopted. This study can help designers in design approach of such motors.*

Keywords**:** *Hysteresis Loop, Axial Flux Hysteresis Motor,* 3*D-FEM Model, Complex Permeability, Air Gap Effect*

1. Introduction

The main features of hysteresis motor are Simple construction with conventional three phase stator windings, solid rotor ring and constant self-starting torque during the run-up and synchronization period [1]. These advantages make the hysteresis motor especially suitable for applications, such as compressors, pumps, timing and recording equipment [2]. Hysteresis motors use the hysteresis characteristics of magnetic materials. It is known the magnetic characteristics of the motor could be easily affected by air gap length and structure dimensions variations [3-5]. Regarding this issue, in this study effect of air gap variation on performance characteristics and optimal hysteresis ring thickness and stator coil turns of axial flux hysteresis motors is investigated. Effect of airgap length on electrical circuit model is perused. Meanwhile, the finite element method (FEM) is implemented for accurate simulation. Such simulation is based upon Maxwell's field equations considering the case of a circumferential flux type machine at synchronous speed. A hysteresis loop in the shape of inclined ellipse is adopted. Also, the application of complex permeability concept is implemented in order to model the hysteresis loop. In this study a 3D finite element model is implemented in order to simulate AFHM. This 3D model has high level of accuracy and gives us a better insight of motor performance. All in all, the objective of this paper is to derive the performance characteristics of axial flux hysteresis motor and to perform sensitivity analysis of such motors at synchronous speed based on 3D FEM. Also, this model can be used in the design approach and precise analysis of axial flux hysteresis motors.

2. Structure and Winding Configuration

This type of motors do not have slot on their rotors and the rotor structure is quite simple. Hysteresis ring is made up of semi hard magnetic materials that can conduct flux line circumferentially. The schematic structure diagram of a two pole axial flux hysteresis motor without ring holder is shown in **Figure 1**. As seen in diagram, the upper surface of the stator has tooth and slots. This stator has a unique three-phase winding that lead to small resistance and the rotor of such motors is generally designed as a disc type motor. The rotor is made up of two parts. Firstly, hysteresis ring which is the basic element for the torque providing that is made of semi hard magnetic material. Secondly, the hysteresis ring holder; which almost is made of the nonmagnetic material such as aluminum and its alloys. This part of motor does not have any effect on steady state operation mode of motor and only is a copulative between the rotor and the motor

Copyright © 2010 SciRes.

shaft. These parts of motor are shown separately in **Figure 2**.

The winding diagram and terminal connection mode of the 2-pole stator windings is shown in **Figure 3**.

Figure 1. The schematic structure diagram of an axial flux hysteresis motor without ring holder

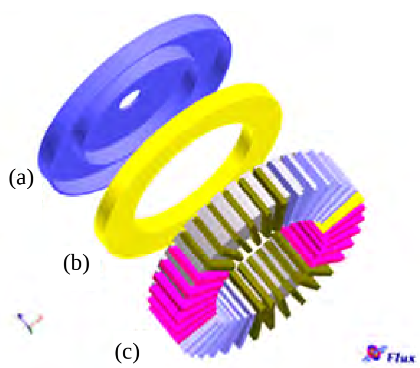

Figure 2. Different parts of axial flux hysteresis motor. (1) Holder; (2) Hysteresis ring; (3) Stator and winding

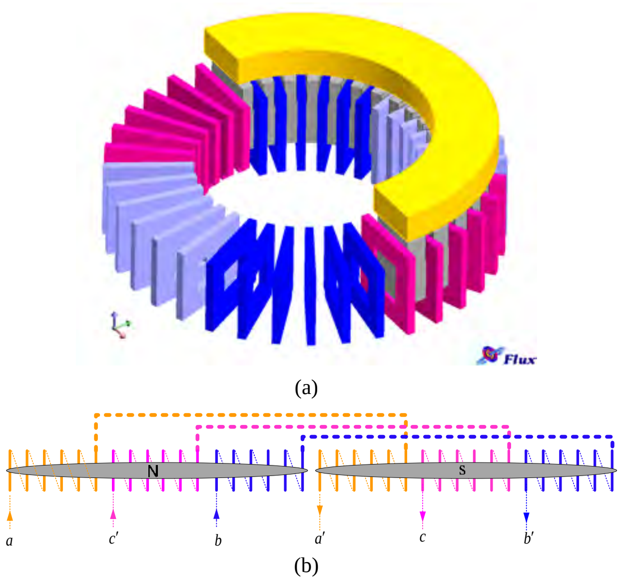

Figure 3. (a) Winding diagram; (b) Stator terminal connection of 2-pole hysteresis motor

3. Air Gap Effect on Electrical Circuit

Figure 4 shows the equivalent electrical circuit of axial flux hysteresis motor [4].

It is proved that air gap length has effect on stator leakage reactance and magnetizing reactance. Equations that show the effect of air-gap on those terms are as bellow [4]:

1-Stator leakage reactance is component of three terms:

$$X_s = X_{slot} + X_{belt} + X_{end} \tag{1}$$

where X_{slot} is the slot reactance, and X_{end} is the ending reactance.

X_{belt} is the belt or differential leakage reactance and its value can be determined by the following equation and an iterative method [4]:

$$X_{belt} = 0.4646 K_b m K_m K_x \times 10^{-9} \tag{2}$$

In order to specify X_{belt}, firstly the values of K_m coefficients should be calculated [4].

$$k_m = \frac{0.001 A_g}{(g_e . P \frac{F_{Ytg}}{F_g})} \tag{3}$$

where, A_g is the air gap area of one pole and g_e is the effective air gap length.

2-Magnetizing reactance [4]:

$$X_M = \omega . \left(\frac{L_g . L_o}{L_g + L_o} \right) \tag{4}$$

In this equation L_g is air gap inductance that depends on effective air gap length [4].

$$L_g = \frac{m\pi}{2P^2} . \frac{N_{Ph}^2 . L . r_g}{g_e} \tag{5}$$

So, variation of air gap length has effect on two terms of equivalent electrical circuit and this effect can influence output characteristics of motor. In next parts, the simulation approach of AFHM is presented in order to investigate the air-gap variation effect.

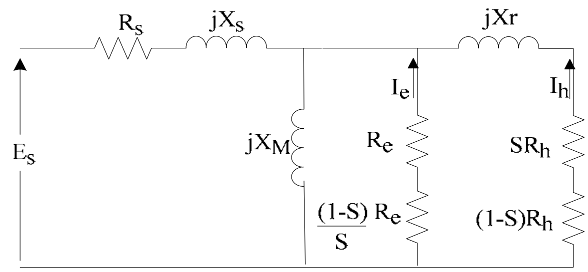

Figure 4. Equivalent electrical circuit of three phase axial flux hysteresis motor

Copyright © 2010 SciRes.

4. Hysteresis Loop Approximation

In this study, a complex permeability is used to predict the hysteresis loop in the inclined ellipse shape. There is some papers that deal with complex permeability and its theory [6-8]. The complex permeability is a useful tool for dealing with magnetic effect. In this study, a complex permeability is used to predict the hysteresis loop in the inclined ellipse. Shape **Figure 5** helps us to exploit the real and imaginary parts of complex permeability ($\mu_r^{'}$ and $\mu_r^{''}$) as a function of H_{max}, H_C and B_{max} [9].

$$\mu_r = \frac{\mu}{\mu_0} = \frac{B_{max}/H_{max}}{\mu_0} \tag{6}$$

$$\gamma = \sin^{-1}\left(H_C/H_{max}\right) \tag{7}$$

$$\mu_r^{'} = \mu_r.\cos(\gamma) \tag{8}$$

$$\mu_r^{''} = \mu_r.\sin(-\gamma) \tag{9}$$

where γ is hysteresis lag angle between flux density and magnetic field intensity, μ_r is the relative permeability, $\mu_r^{'}$ and $\mu_r^{''}$ are the real and imaginary part of complex permeability.

As known, for a hysteresis material there is different hysteresis loop. In order to choose an accurate loop regarding to magnetic circuit that hysteresis material is in, an iteration method is used that is illustrated with a flow chart in **Figure 6**. In the first iteration, a random hysteresis ring is selected. So, all the hysteresis ring elements have the arbitrary permeability. From the FEA, the maximum flux density for the circumferential direction in the hysteresis ring region can be obtained. Now, the maximum flux density obtained from FEA is checked with previous value and this procedure continues until the convergence criterion is satisfied. If the analysis is completed, torque of motor can be evaluated. It is so important to select an accurate hysteresis loop since the output torque of the motor is proportional to the area of hysteresis loop [10,11] regarding Equation (5).

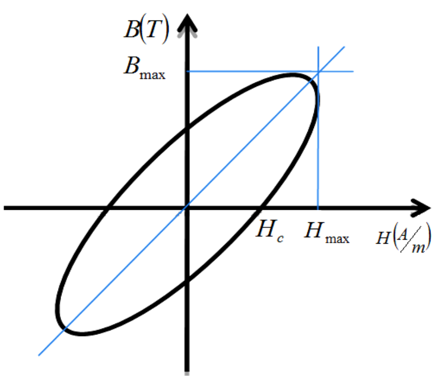

Figure 5. Inclined hysteresis loop approximation

$$T = \frac{1}{2\pi} p V_r E_h \tag{10}$$

where, p is number of pole pairs, V_r is the hysteresis ring volume and E_h is the area of hysteresis loop.

It is seen that that this procedure is so effective and hysteresis loop modeling with complex permeability has close agreement with real motor tests.

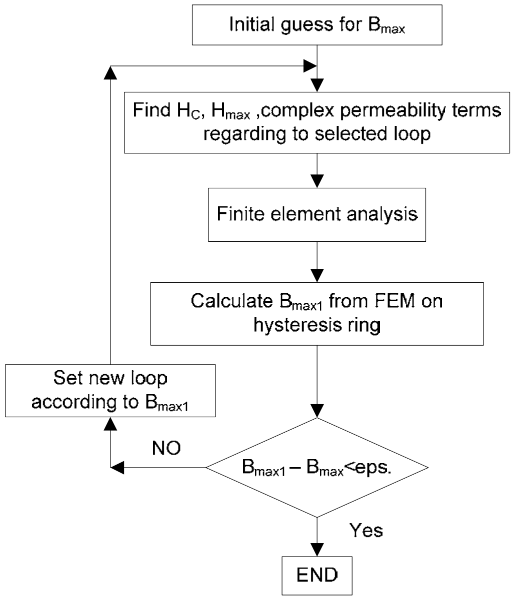

Figure 6. Flow chart for accurate hysteresis selection

5. FEM Model

As mentioned before, a 3D finite element model is implemented in order to simulate of proposed motor [12]. This 3D model has high level of accuracy and gives us a better insight of motor performance. Finite element method is based on Maxwell's equations. The electromagnetic field inside the machine is given by:

$$curlE = -\partial B/\partial t \tag{11}$$

$$curlH = J + \partial D/\partial t \tag{12}$$

$$divB = 0 \tag{13}$$

$$divD = \rho \tag{14}$$

In order to have high level of accuracy the automatic mash diagram is not used and a mesh diagram is designed manually. In this simulation node congestion is higher around the air gap and hysteresis ring. Hexagonal element in stator and trigonal prism element is used in rotor in order to constitute the mesh diagram. The total number of nodes is about 130000 that lead to high level of accuracy. Meanwhile, for boundary conditions, the homogenous Dirichlet condition is adopted on the infi-

Copyright © 2010 SciRes.

nite box that encompasses the motor.

This simulation is based on circuit coupled model that the phase voltage is the input quantity. **Figure 7** shows the circuit coupled model that is used in this study. In this model for each phase two coil winding is considered. One of this coils send the current in motor and another returns current from midpoint of winding in star connection. Coil winding connection in each phase is exactly as the same that is illustrated in **Figure 3(b)**. Meanwhile, in this model voltage source is assumed as the input source.

6. Simulation Results and Discussion

Based on the above respects, finite element simulation for the axial flux hysteresis motor has been done. The simulation research has been made for a 2 poles prototype AFHM. The parameter of the prototype axial flux hysteresis motor and the output quantities of motor for 2 mm air gap is given in **Table 1**.

It must be noted that half of the motor is analyzed because of the magnetic symmetry of the motor. As seen in **Figure 8** nodes congestion becomes higher near the air gap and hysteresis ring in order to accurate simulation.

Figure 9 shows the distribution of flux in motor.

As said before, flux lines are circumferentially through the hysteresis ring.

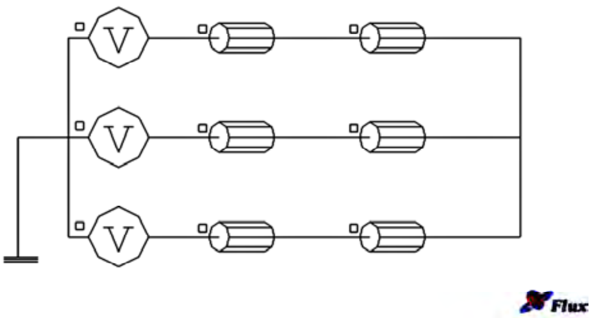

Figure 7. Circuit coupled model used in simulation

Table 1. Motor characteristics

Quantity	Value	Quantity	Value
Rated power(hp)	0.27	Outer diameter of stator(mm)	108
voltage(V)	150	Inner diameter of stator(mm)	75
Rated phase current(A)	3.2	Stator stack height(mm)	14
Frequency(Hz)	300	Stator Tooth height(mm)	10
Phase connection	Y	Number of slots	36
Pole pairs	1	Number of turns per coil	35
Air gap length(mm)	2	Fill factor	0.48
rotor outer diameter(mm)	112	Phase resistance at 300Hz(Ω)	2
Thickness of rotor ring(mm)	9	Br(T)	0.48

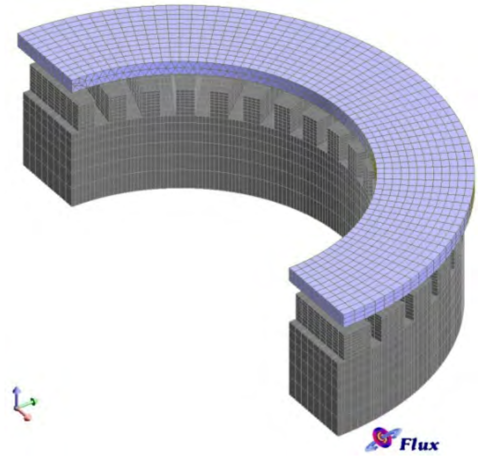

Figure 8. Mesh congestion is higher near air gap and hysteresis ring

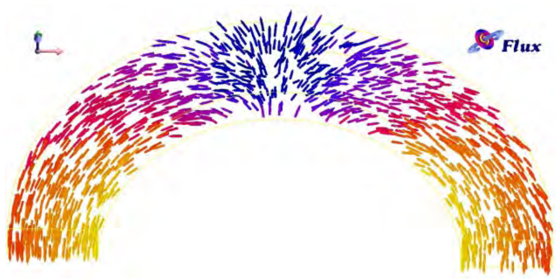

Figure 9. Distribution of the circumferential flux

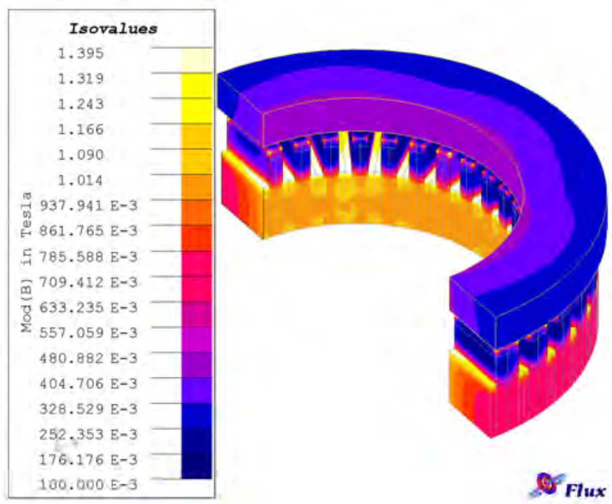

Figure 10. Isovalues diagram of flux density of axial flux hysteresis motor

Figure 10 shows the isovalues diagram of flux density in motor.

Since now based on FEM model the simulation of motor for real dimensions is done and the output characteristics of motor is extracted. Now by change the air gap from 0.6 mm to 4 mm the variation of output quantities is

Copyright © 2010 SciRes.

investigated.

Figure 11 demonstrates variations of the input current of the machine versus air gap length of motor.

From Equations (3) and (5) it is obvious that air gap reduction leads to higher value of X_{belt} and X_M. So, impedance has increased and input current has a less value.

The maximum flux density in rotor ring for various air gap is illustrated in **Figure 12**.

Figure 13 demonstrates variations of the torque of the machine versus air gap length of motor.

As the air gap length reduced, distribution of flux density in air gap has higher value and this effect leads to higher flux density in hysteresis ring. So, the output torque increases.

Figure 14 demonstrates variations of the power factor of the machine versus air gap length of motor.

From this diagram it is found that the relative of real part of impedance to imaginary part is increased by lower air gap length. The magnetizing current is decreased by lower values of airgap and so the imaginary part of current is decreased, too.

Figure 15 demonstrates variations of efficiency of the machine versus air gap length of motor.

By reduce in air gap length input power is reduced by lower level of input current and the output torque is increased, so it is obvious that the efficiency will be increased.

Figure 16 demonstrates variations of the hysteresis ring thickness versus air gap length of motor under constant load.

According to **Figure 12** it can be extracted that the lower air gap length lead to higher maximum flux density on hysteresis ring and higher flux density lead to bigger hysteresis loop. So area of hysteresis loop increases with lower air gap length. Meantime, Equation (10) shows for constant load torque the bigger hysteresis loop area lead to smaller hysteresis ring volume. Thus, when the air gap length is decreased, the thickness of hysteresis ring is decreased, too. Though, simulation shows that for air gaps bigger than 3.2 mm, thicker hysteresis ring cannot produce base torque and the hysteresis ring is in saturated zone.

Figure 17 demonstrates variations of the stator winding turns versus air gap length of motor under constant load.

According to **Figure 11** it can be extracted that the lower air gap length lead to lower terminal current and lower terminal current lead to lower ampere-turn. So, for

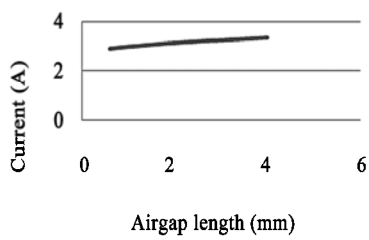

Figure 11. Terminal current variation versus air gap length

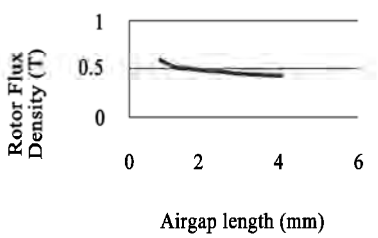

Figure 12. Maximum flux density in rotor versus air gap length

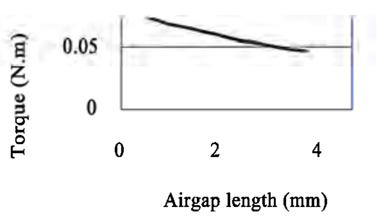

Figure 13. Output torque variation versus air gap length

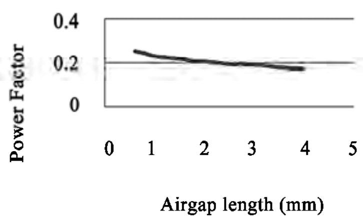

Figure 14. Power factor variation versus air gap length

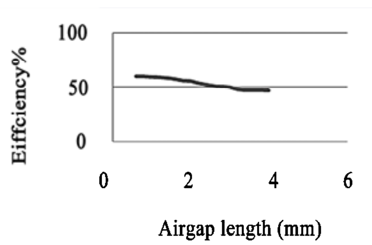

Figure 15. Efficiency variation versus air gap length

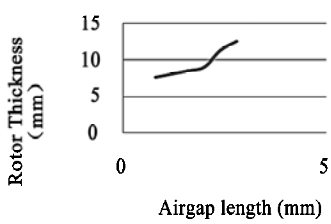

Figure 16. Hysteresis ring thickness versus air gap length

Copyright © 2010 SciRes.

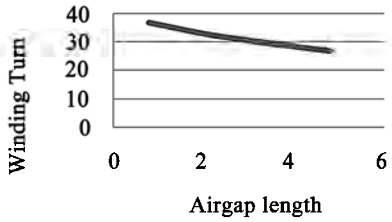

Figure 17. Stator winding turns versus air gap length

constant load number of stator turns must be increased to produce same ampere-turns.

7. Conclusions

In this paper, for an accurate analysis of the hysteresis motor and to perform the sensitivity analysis for axial flux hysteresis motor a finite element analysis model is used. A hysteresis loop in an inclined ellipse shape is adopted to approximate the hysteresis loop. Therefore, the method can consider the rotational hysteresis effects which the scalar hysteresis model cannot deal with. The simulation based on real dimensions of a typical motor is done. Effect of air gap variation on output quantities of such motors, and optimal thickness of hysteresis ring and stator winding turns under constant load is investigated. Furthermore all simulation results show that smaller air gap (g) how much increases machine efficiency, Power factor, maximum flux density, torque and stator winding turns and reduces the terminal current and hysteresis ring thickness for constant load. So by considering the mechanical constrains, the air gap is assumed minimum possible value.

REFERENCES

[1] M. Azizur Rahman, “Analytical Models for Polyphase Hysteresis Motor,” *Rotating Machinery Committee of the IEEE Power Engineering Society*, December 10, 1970.

[2] M. Azizur Rahman and R. F. Qin, “Starting and Synchronization of Permanent Magnet Hysteresis Motors,” *IEEE Transactions on Industry Applications*, Vol. 32, No. 5, September/October 1996.

[3] K. R. Rajagopal, “Design of a Compact Hysteresis Motor Used in a Gyroscope,” *IEEE Transactions on Magnetic*, Vol. 39, No. 5, September 2003.

[4] A. Darabi, H. Lesani, T. Ghanbari1 and A. Akhavanhejazi, “Modeling and Optimum Design of Disk-Type Hysteresis Motors,” *Proceeding of International Conference on Electrical Machines and Systems*, 8-11 October 2007, Seoul, Korea.

[5] A. Sedagati and A. Vahedi, “Effect of Parameters Design on the Characteristics of Hysteresis Motor,” *IEEE Conference*, *Electrical Machines and Systems*, Vol. 1, 9-11 November 2003, pp. 246-249.

[6] F. A. A. Zaher, “An Analytical Solution for the Field of a Hysteresis Motor Based on Complex Permeability,” *IEEE Transaction on Energy Conversion*, Vol. 5, No. 1, March 1990.

[7] M. Modarres, A. Vahedi and M. R. Ghazanchaei, “New Topology of a Slotted Disk Type Hysteresis Motor,” *Proceedings of International Conference on Coil Winding*, *Insulations & Electrical Manufacturing* (*CWIEME*), Mumbai, India, November 2009.

[8] T. Horii, N. Yuge and G. Wakui, “Analysis of a Hysteresis Motor on Asynchronous Speed Using Complex Permeability,” *IEEE Translation Journal on Magnetics in Japan*, Vol. 9, No. 2, March/April 1994.

[9] M. Getzlaff, “Fundamental of Magnetism,” Springer-Verlag, Berlin, 2008.

[10] H. K. Kim, S. K. Hong and H. K. Jung, “Analysis of Hysteresis Motor Using Finite Element Method and Magnetization-Dependent Model,” IEEE Transactions on Magnetic, Vol. 36, No. 4, July 2000.

[11] S. K. Hong, H. K. Kim, H. S. Kim and H. K. Jung, “Torque Calculation of Hysteresis Motor Using Vector Hysteresis Model,” IEEE Transactions on Magnetic, Vol. 36, No. 4, July 2000.

[12] CEDRAT Group, “Flux3D User’s Guide,” Version 10.3, France, 2009.

J. Electromagnetic Analysis & Applications, 2010, 2: 258-263
doi:10.4236/jemaa.2010.24032 Published Online April 2010 (http://www.SciRP.org/journal/jemaa)

Developing a 3D-FEM Model for Electromagnetic Analysis of an Axial Flux Permanent Magnet Machine

Seyyed Mehdi Mirimani, Abolfazl Vahedi

Department of Electrical Engineering, Centre of Excellence for Power Systems Automation and Operation, Iran University of Science & Technology, Tehran, Iran.
Email: mehdimirimani@gmail.com, avahedi@iust.ac.ir

Received December 13th, 2009; revised January 27th, 2010; accepted February 4th, 2010.

ABSTRACT

Recently, many optimal designs for axial flux permanent magnet (AFPM) motors were performed based on finite- element (FE) analysis. Most of the models are based on reduction of 3D problem to 2D problem which is not accurate for design aspects. This paper describes an accurate electromagnetic analysis of a surface mounted, 28 pole AFPM with concentrated stator winding. The AFPM is modeled with three-dimensional finite-element method. This model includes all geometrical and physical characteristics of the machine components. Using this accurate modeling makes it possible to obtain demanded signals for a very high precision analysis. Magnetic flux density, back-EMF, magnetic axial force and cogging torque of the motor are simulated using FLUX-3D V10.3.2. Meanwhile, the model is parametric and can be used for design process and sensitivity analysis.

Keywords: *Axial Flux Permanent Magnet (AFPM) Motor, Three-Dimensional Finite-Element Method (3D-FEM), Cogging Torque*

1. Introduction

Axial Flux Permanent Magnet Machines (AFPMM) firstly appeared in technical literatures in the mid of 70s and their fields of application spread widely. AFPM machines are increasingly used in various applications due to their high efficiency, compact construction and high torque at low speed [1-3]. AFPM unique topologies allow designers to design multi pole machines. Thus, it can be directly coupled to the low-speed turbines, such as wind and hydro turbines [4]. Their robustness and compactness make high-speed axial-flux machines suitable for distributed generating application [5]. It is also a suitable candidate for electric vehicle (EV) and traction motors [6].

Modeling of electrical machines is very important because of its usage in study of machines behavior and optimization process. Modeling methods of electrical machines can be categorized into analytical modeling and numerical modeling. Analytical modeling has the profit of rapidity but, the accuracy of this modeling is not enough for optimization in design process. Instead, Numerical modeling is very accurate method but this method is time consuming. Numerical modeling is used in applications Such as design and optimization of electrical devices that accurate modeling is needed. In such applications, accuracy is very important and duration of simulation has less importance. Numerical method is based on discretization of calculation domain to finite elements and solving Maxwell equations in these elements. Finite-element method can be categorized into two-dimensional (2D) and three-dimensional (3D) method. 3D form is more time consuming but it has higher accuracy than 2D modeling. Many literates have demonstrated that AFPM Machines are intrinsically 3-D machines and accurately analyzing the behavior of these machines needs 3D-FEM modeling [7]. Many of the literatures model an AFPM based on reduction of the 3D problem to a 2D problem. These models are not accurate for design process and sensitivity analysis [1,8,9].

In this paper, a surface mounted axial flux permanent magnet (AFPM) motor with concentrated coils is modeled using 3-dimensional finite element method. Magnetic flux density of airgap, back-EMF, axial forces between rotor and stator and cogging torque are calculated.

Copyright © 2010 SciRes.

This accurate model can be used for design process and sensitivity analysis.

2. Motor Specification

Figure 1 shows a three-phase, 210-V, 2200-W, 1285-rpm, Δ-connected AFPM machine that was modeled. It consists of a stator with 24 slots and 12 single layer concentrated coils with fractional winding. Fractional slot windings allow a large number of poles to be designed without increasing the number of slots by putting less than one slot per phase under each rotor pole. This procedure results also into a more compact winding design, allowing for less copper losses due to shorter end connections. The concentrated winding allows a large number of pole pairs to be designed even in a small machine [10]. Coils with a same color in the model belong to one phase. The rotor disc consists of 28 magnets of alternating polarity. The machine parameters are given in **Table 1** [7].

3. Finite Element Simulation

Many literates have demonstrated that accurate analysis of AFPM behaviors is not an easy task because these types of machines are intrinsically 3-D machines [7,8]. Three dimensional finite-element method (FEM) allows a precise analysis of magnetic devices taking into account geometric details and magnetic nonlinearity. So, it is an appropriate method for analyzing AFPMs. By using this accurate modeling it is possible to obtain demanded signals for a very high precision analysis. Finite element method is based on Maxwell's equations. The electromagnetic field of the machine is given by:

$$
\begin{aligned}
curlE &= \partial B / \partial t \\
curlH &= J + \partial D / \partial t \\
divB &= 0 \\
divD &= \rho
\end{aligned}
\tag{1}
$$

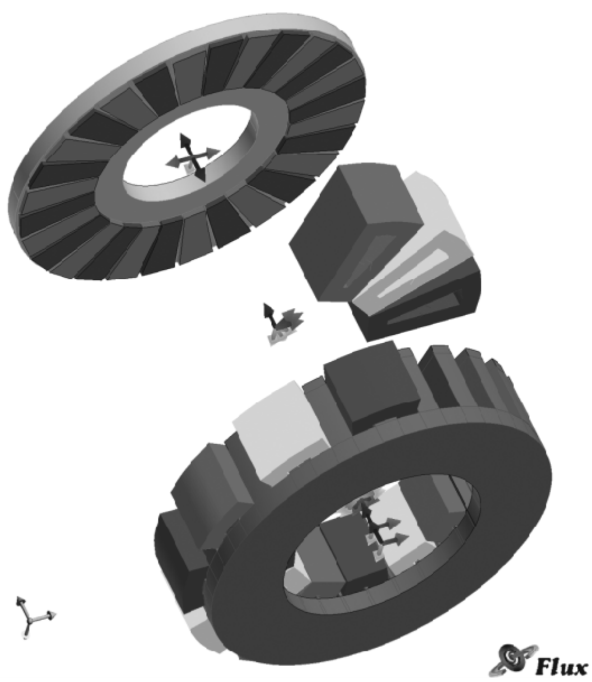

Figure 1. Twenty-eight pole three-phase AFPM

The center of the stator is fixed at the origin of the global coordinate system. The center of the rotor is located at the origin of the local coordinate system, which rotate around the center of the global coordinate system, *i.e.* the center of the stator, by a constant step angle. Investigation of AFPM model was made with the assumptions of nonlinear materials. In order to have high level of precision, the mesh diagram is designed manually. **Figure 2** shows mesh diagram of the proposed motor and as it shows, density of meshes increases near the air-gap in order to a precise simulation. Whole nodes number is 460,000 in this simulation. This amount of nodes is very high and will warrant the accuracy of simulation. **Figure 3** demonstrates the flux diagram of motor. It shows that maximum flux density in hotspots is 2.147 T. Three-dimensional finite-element analysis (3D-FEA) software FLUX2D/3D by CEDRAT is used to simulate the motor [9]. **Figure 2** shows The FEM model that was used in this paper.

Table 1. Specifications of the motor

Quantity	Value
Rated power(kW)	2.2
No load voltage(V)	210
Rated phase current(A)	3.5
Frequency(Hz)	300
Speed(rpm)	1285
Phase connection	Δ
Pole pairs	14
Air gap length(mm)	1.2
Rotor diameter(mm)	206
Remanence of magnets(T)	1.24
Thickness of magnets(mm)	3
Outer diameter of stator(mm)	200
Inner diameter of stator(mm)	116
Slot width(mm)	13.6
Slot height(mm)	40
Number of slots	24
Width of stator back iron(mm)	10.5
Width of rotor back iron(mm)	10
Wire diameter(mm)	1.5
Number of turns per coil	130
Phase resistance at 300Hz(Ω)	2.5

Copyright © 2010 SciRes.

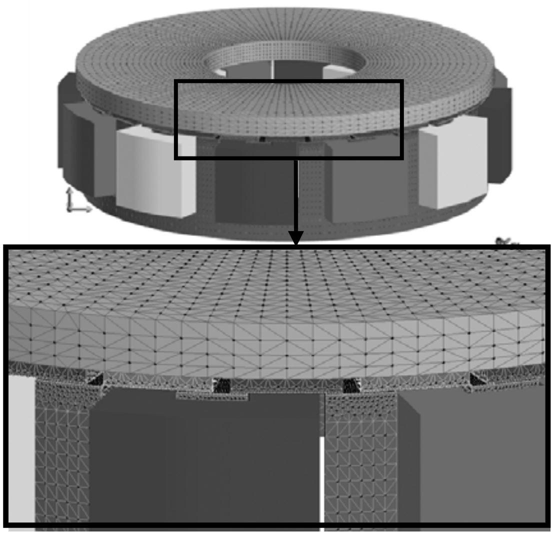

Figure 2. Three-dimensional mesh model

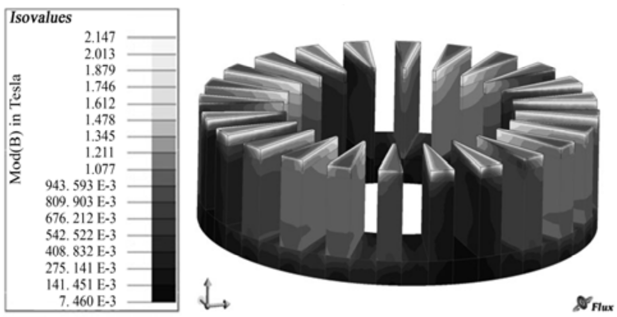

Figure 3. Flux density distribution in the stator

3.1. Calculation of Airgap Flux Density

One of the most important characteristics of the motor is airgap flux density. So, it was simulated under no-load condition to monitor the airgap pattern. **Figure 4** shows the axial component of the no-load air-gap flux density due to permanent magnets in the middle of airgap plane. Moreover, the z-component of the no-load air-gap flux density was computed over a circumference in the plane. **Figure 5** reports the waveform.

3.2. Axial Force between Rotor and Stator

In axial flux permanent magnet machines, there is an axial force between rotor magnets and stator teeth. **Figure 6** represents the schematic of this axial force. **Figure 7** shows that the period of this force fluctuation is equal to the angular distance between two identical permanent magnets. It means that after this angular displacement, a N pole replaces by another coming one and the situation of permanent magnets toward the stator teeth becomes similar to the previous position. The force fluctuations will repeat a same manner in other periods. The period is obtained as follows:

$$\varphi = \frac{360}{\left(p/2\right)} \tag{2}$$

where p is number of machine poles. **Figure 8** shows the total magnetic force fluctuates of the motor in one period. This trend will repeat in other periods. Its mean value is 2152 N. **Figure 9** shows frequency spectrum of the axial force.

3.3. Calculation of Back-EMF

In this case, the back EMF is sinusoidal due to the windings layout. **Figure 10** shows the Back-EMF of the motor at no-load and its RMS value is 209.996 V. The

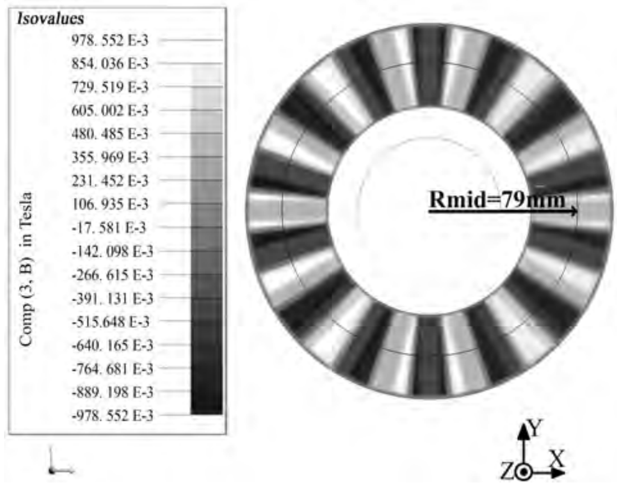

Figure 4. Axial component of the no-load air-gap flux density

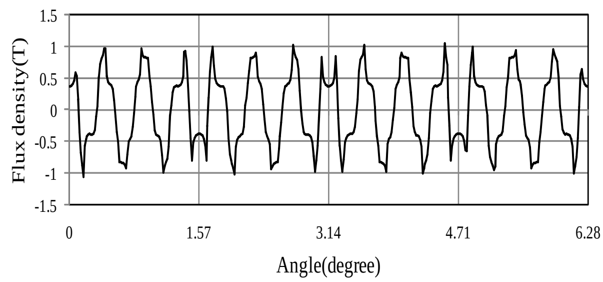

Figure 5. Z-component of the no-load air-gap flux density over a circumference in the middle of air-gap plane (r = 79 mm)

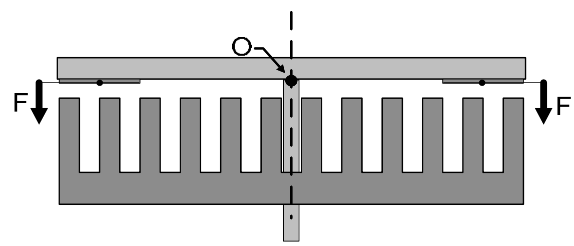

Figure 6. Schematic representation of axial forces in axial flux permanent magnet motor

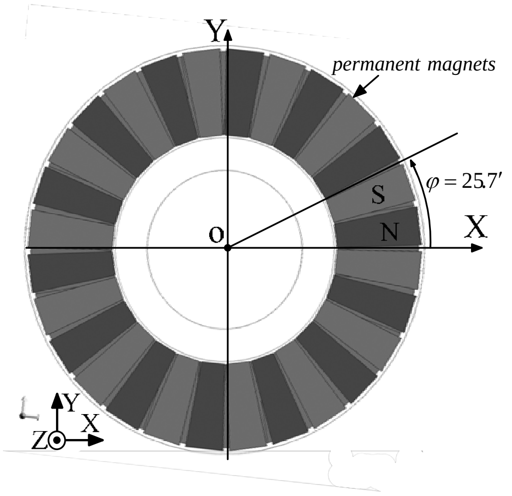

Figure 7. Top view of permanent magnets

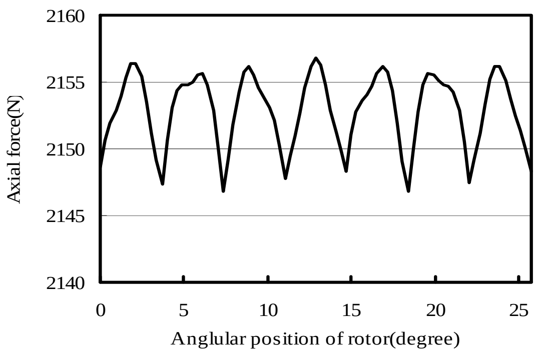

Figure 8. Axial force between rotor and stator

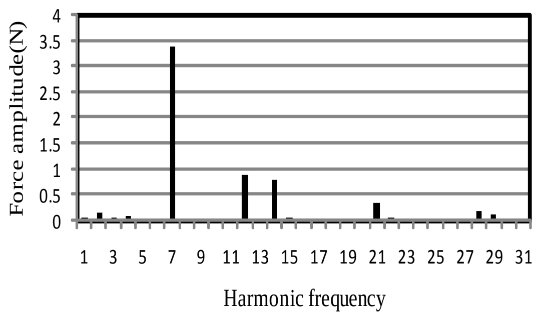

Figure 9. Frequency spectrum of the Axial force between rotor and stator

nominal voltage of motor is 210 V and it can be seen that the simulated voltage has a good agreement with the nominal one. **Figure 11** illustrates frequency spectrum of the back-EMF. It shows that the superior harmonics in the spectrum is the first harmonic with amplitude of 289.08 V and then the fifth harmonic with amplitude of 3.02 V. Existence of harmonics is dependent on non-linearity of core and concentration of coils.

From the amplitude of back-EMF, the permanent magnet fundamental flux is calculated:

$$\varphi_{PM} = \frac{\sqrt{2} \times E_0}{2 \times \pi \times N \times f} = 0.0121\,Wb \qquad (3)$$

N is the number of turns per coil, $\mathbf{E_0}$ is the RMS value of back-EMF and **f** is the frequency.

3.3. Calculation of Cogging Torque

The vibration and acoustic noise of machines is a very important factor. The research for vibration of PM machines which is a kind of new efficient machines is more and more attended. High torque density and efficiency of axial flux permanent magnet machines make them an ideal choice in many high performance applications. However, cogging torque in these machines has undesirable effects of torque ripple, noise and vibration. This torque is proportional to the PM flux and the reluctance variation, and is independent of the load current. In PM machines, cogging torque arises from the magnet's tendency to align itself with the minimum reluctance path given by the relative position between rotor and stator. This is an inherent characteristic of AFPMs. It was calculated and shown in **Figure 12**. A closer inspection of

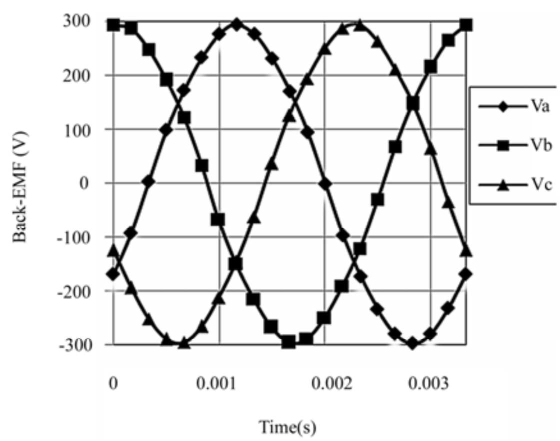

Figure 10. Back-EMF of the motor

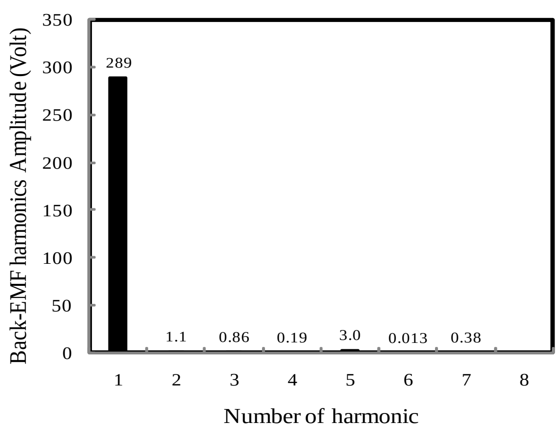

Figure 11. Frequency spectrum of the Back-EMF

Figure 12 shows a low frequency modulation of the torque ripple. As cogging torque is minimized through successful optimization, the relative proportion of the low-frequency component increases and becomes noticeable. However, for machines with very low amount of cogging torque, the low frequency component can add a noticeable ratio of ripple to overall cogging amplitude [11]. The number of periods of the cogging torque per rotor revolution is:

$$N_1 = LCM(N_p, N_s) \quad (4)$$

where N_s is the number of slots and N_p is the number of poles. N_l = 168 is the least common multiple of N_s = 24 and N_p = 28. It means that the cogging torque period is 2.14 degrees. In **Figure 12**, 14 cycles occur over an angular displacement of about 30 degree, yielding the requisite 168 cycles in 2π radians. The modulation harmonic was discussed in [11]. By definition:

$$N_c = GCF(N_p, N_s) \quad (5)$$

$$N_m = LCM(N_p, N_c) \quad (6)$$

N_m is the number of periods of the modulation frequency per rotor revolution. N_m = 28 and it means that we have 28 periods of modulation frequency in 2π radians. So, the modulation harmonic period is 12.857 degree that is six times of the period of main harmonic.

Figure 13 shows the harmonics of cogging torque computed via three-dimensional FEM analysis. It shows that there are two superior harmonics in the spectrum. First harmonic belongs to modulation frequency and sixth belongs to the main frequency of cogging torque that repeats 6 times in the period of modulation frequency.

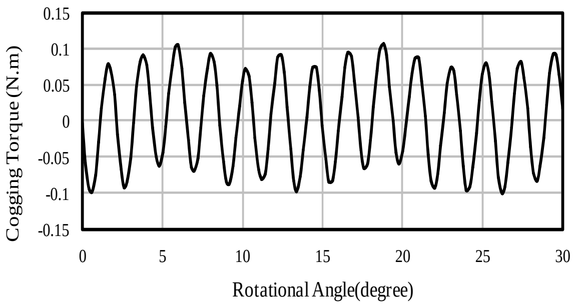

Figure 12. Cogging torque waveform of the motor

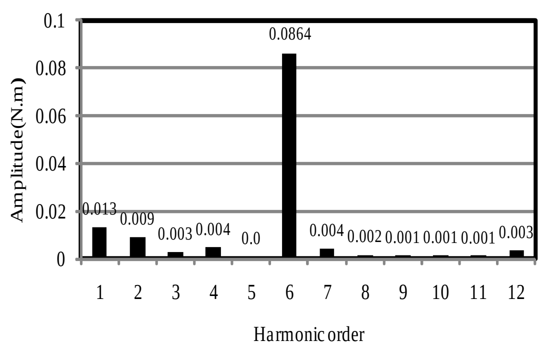

Figure 13. Frequency spectrum of the cogging torque

5. Conclusions

The paper addresses electromagnetic characteristics of an axial flux permanent magnet machine. A three- dimensional finite element analysis model is presented for accurate analysis of the Axial Flux Permanent Magnet motor. This model is parametric one and can be used for design process and sensitivity analysis of AFPM machine. Air-gap flux density, back-EMF, axial forces and cogging torque was calculated using this model and it is shown that the simulation results have a good agreement with the motor's characteristics and nominal values.

6. Acknowledgments

The authors would like to thank Dr. Fabrizio Marignetti of University of Cassino (Italy) for his helps and advices.

REFERENCES

[1] N. Chaker, I. B. Salah, S. Tounsi and R. Neji, "Design of Axial-Flux Motor for Traction Application," *Journal of Electromagnetic Analysis and Applications*, Vol. 1, No. 2, June 2009, pp. 73-83.

[2] F. Caricchi, F. Crescimbini, F. Mezzetti and E. Santini, "Multistage Axial Flux PM Machine for Wheel Direct Drive," *IEEE Transactions on Industry Applications*, Vol. 32, No. 4, 1996, pp. 882-887.

[3] A. B. Letelier, D. A. González, J. A. Tapia, R. Wallace and M. A. Valenzuela, "Cogging Torque Reduction in an Axial Flux PM Machine via Stator Slot Displacement and Skewing," *IEEE Transactions on Industrial Applications*, Vol. 43, No. 3, May 2007, pp. 685-693.

[4] Y. Chen, P. Pillay and A. Khan. "PM Wind Generator Comparison of Different Topologies," *Conference Record of IEEE 39th Inustrial Applications Annual Meeting*, Vol. 3, October 2004, pp. 1405-1412.

[5] S. M. Hosseini, M. Agha-Mirsalim, and M. Mirzaei, "Design, Prototyping and Analysis of Low Cost Axial-Flux Coreless Permanent-Magnet Generator," *IEEE Transactions on Magnetics*, Vol. 44, 2008, pp. 75-80.

[6] Y.-P. Yang and D. S. Chuang, "Optimal Design and Control of a Wheel Motor for Electric Passenger Cars," *IEEE Transactions on Magetics*, Vol. **43**, 2007, 51-61.

[7] F. Marignetti, V. Delli Colli and Y. Coia, "Design of Axial Flux PM Synchronous Machines Through 3-D Coupled Electromagnetic Thermal and Fluid-Dynamical Finite-Element Analysis," *IEEE Transactions on Industrial Electronics*, Vol. 55, No. 10, October 2008, pp. 3591-3601.

[8] P. R. Upadhyay and K. R. Rajagopal, "FE Analysis and Computer-Aided Design of a Sandwiched Axial-Flux

Permanent Magnet Brushless DC Motor," *IEEE Transaction on Magnetics*, Vol. 42, No. 10, October 2006, pp. 3401-3403.

[9] Y.-P. Yang, J.-P. Wang, S.-W. Wu and Y.-P. Luh, "Design and Control of Axial-Flux Brushless DC Wheel Motors for Electric Vehicles—Part II: Optimal Current Waveforms and Performance Test," *IEEE Transaction on Magnetics*, Vol. 40, No. 4, July 2004, pp. 1883-1891.

[10] F. Marignetti, G. Tomassi, P. Cancelliere, V. Delli Colli, R. D. Stefano and M. Scarano. "Electromagnetic and Mechanical Design of a Fractional-slot-windings Axial-flux PM Synchronous Machine with Soft Magnetic Compound Stator," *IEEE Industry Applications Conference*, 2006, pp. 62-69.

[11] D. R. McIntosh, "Identification and Analysis of Low-Frequency Cogging Torque Component in Permanent Magnet Machines," *Proceedings of the COMSOL Conference, Boston*, 1 January 2008.

J. Electromagnetic Analysis & Applications, 2010, 2: 264-269
doi: 10.4236/jemaa.2010.24033 Published Online April 2010 (http://www.SciRP.org/journal/jemaa)

Guided Modes in a Four-Layer Slab Waveguide with Dispersive Left-Handed Material

Lufa Shen[1,2], Zihua Wang[3]

[1]Centre for Optical and Electromagnetic Research, Zhejiang University, Hangzhou, China; [2]Science College, Huzhou Teachers College, Huzhou, China; [3]Key Laboratory of Specialty Fiber Optics and Optical Access Networks, Shanghai University, Shanghai, China.
Email: shenlufa0410@sina.com

Received December 15th, 2009; revised January 23rd, 2010; accepted February 4th, 2010.

ABSTRACT

A four-layer slab waveguide including left-handed material is investigated numerically in this paper. Considering left-handed material dispersion, we find eight TE guided modes as frequency from 4 *GHz to* 6 *GHz. The fundamental mode can exist, and its dispersion curves are insensitive to the waveguide thickness. Besides, the total power fluxes of TE guided modes are analyzed and corresponding new properties are found, such as: positive and negative total power fluxes coexist; at maximum value of frequency, we find zero total power flux, etc. Our results may be of benefit to the optical waveguide technology.*

Keywords**:** *Slab Waveguide, Left-Handed Material, Dispersive Properties, Total Power Fluxes*

1. Introduction

Since Smith *et al.* [1] made firstly the left-handed material (LHM) with negative permittivity and negative permeability in microwaves, it has attracted much attention due to their novel electromagnetic properties. Now, negative refraction has been successfully realized in THz waves, and optical waves [2,3]. Many scholars [4-6] have analyzed symmetric slab waveguide containing LHM. Typical properties of these waveguides including the absence of the fundamental mode, backward propagating waves with negative power flux have been found. The LHM asymmetric slab waveguides and the slab waveguides with LHM cover or substrate have also been investigated [7-9]. Besides, the five-layer slab waveguides with LHM have been investigated and several new dispersion properties have been discovered [10-12]. J. Zhang etc. [13] have studied a four-layer slab waveguide with LHM core by using a graphical method. We know that the graphical method can only determine whether or not the mode exists. Furthermore, most above researches are neglecting LHM dispersion. This is not the practical case.

In this paper, the four-layer slab waveguide with LHM in one layer and right-handed materials (RHMs) in the other layers is investigated. The material dispersion of LHM has been considered. Through Maxwell's equations, by using a transfer matrix method, two dispersion equations for the *TE* guided modes are obtained. Solving these equations, we plot some dispersion curves. Compared these curves, some dispersion properties of *TE* guided modes are obtained. Besides, power fluxes of *TE* guided modes are calculated in the waveguide and the corresponding curves are plotted, respectively. From these curves we find some new power flux properties.

2. Dispersion Equations and Total Power Flux

2.1 Dispersion Equations

A four-layer slab waveguide including LHM is shown in **Figure 1**. Medium 1 is the LHM, *i.e.* its dielectric permittivity (ε_1), magnetic permeability (μ_1) and refractive index (n_1) are all negative. However, the cover (medium 0) and the substrates (media 2 and 3) are different conventional materials, thus, their dielectric permittivity (ε_0, ε_2 and ε_3), magnetic permeability (μ_0, μ_2 and μ_3) and refractive index (n_0, n_2 and n_3) are all positive. The thicknesses of media 1, 2 is h_1 and h_2, respectively. Besides, we assume that media 0 and 3 extend to infinity. For simplicity, the time-and z-factor $\exp[i(\omega t-\beta z)]$ that multiplies all the field components is neglected from all equations. Where ω and β denote angular frequency and longitudinal propagation constant. Usually, a slab waveguide can support *TE* and *TM* modes. In this paper,

Copyright © 2010 SciRes.

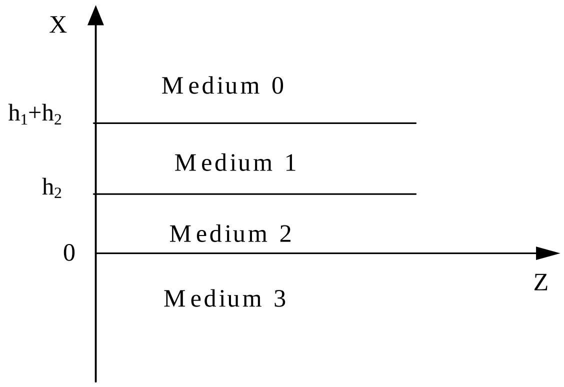

Figure 1. The geometry for a four-layer slab waveguide including left-handed material

we study *TE* guided modes. For *TM* modes, they will be investigated in other papers. By using Maxwell's equations, the only electric field E_y for TE modes satisfies the following equation:

$$\frac{\partial^2 E_y}{\partial x^2} + (k_0{}^2 n_i{}^2 - \beta^2)E_y = 0 \tag{1}$$

where $k_0 = \frac{2\pi}{\lambda}$, λ is the wavelength in vacuum, n_i denotes refractive indexes in media i with i = 0, 1, 2 and 3, respectively. For different β, there exist two cases as follows:

Case 1 $k_0 n_3 < \beta < k_0 n_2$

In this case, guided mode fields decay in media 0 and 3, and oscillate in media 1 and 2. We call these modes as the first guided modes and note them TE_m^{I}. From Equation (1), their electric fields in the slab waveguide are as follows:

$$E_{y0} = A\cos\varphi_{10}\exp[-q_0(x - h_1 - h_2)], x \ge h_1 + h_2 \tag{2}$$

$$E_{y1} = A\cos[k_1 x - k_1(h_1 + h_2) + \varphi_{10}], h_2 \le x \le h_1 + h_2 \tag{3}$$

$$E_{y2} = AB\cos(k_2 x - \varphi_{23}), 0 \le x \le h_2 \tag{4}$$

$$E_{y3} = AB\cos\varphi_{23}\exp(q_3 x), x \le 0 \tag{5}$$

where A is an undetermined constant, and

$$\kappa_1 = \sqrt{\varepsilon_1\mu_1 k_0{}^2 - \beta^2}\,,\quad \kappa_2 = \sqrt{\varepsilon_2\mu_2 k_0{}^2 - \beta^2}$$

$$q_0 = \sqrt{\beta^2 - \varepsilon_0\mu_0 k_0{}^2}\,,\quad q_3 = \sqrt{\beta^2 - \varepsilon_3\mu_3 k_0{}^2}$$

$$\varphi_{10} = \arctan(\frac{\mu_1 q_0}{\mu_0 k_1})\,,\quad \varphi_{23} = \arctan(\frac{\mu_2 q_3}{\mu_3 k_2})\,,$$

$$B = \frac{\cos(k_1 h_1 - \varphi_{10})}{\cos(k_2 h_2 - \varphi_{23})}.$$

With continuous conditions of the transverse electromagnetic fields and by using the transfer matrix method, a dispersion equation for TE_m^{I} mode is obtained as follows:

$$\begin{bmatrix} -p_0 & 1 \end{bmatrix} M_1 M_2 \begin{bmatrix} 1 \\ -p_3 \end{bmatrix} = 0 \tag{6}$$

where
$$M_1 = \begin{bmatrix} \cos(k_1 h_1) & \frac{\mu_1}{k_1}\sin(k_1 h_1) \\ -\frac{k_1}{\mu_1}\sin(k_1 h_1) & \cos(k_1 h_1) \end{bmatrix},$$

$$M_2 = \begin{bmatrix} \cos(k_2 h_2) & \frac{\mu_2}{k_2}\sin(k_2 h_2) \\ -\frac{k_2}{\mu_2}\sin(k_2 h_2) & \cos(k_2 h_2) \end{bmatrix}$$

After some algebraic manipulation, Equation (6) can be rewritten as:

$$k_1 h_1 = m\pi + \arctan(\frac{\mu_1 q_0}{\mu_0 k_1}) + \arctan(\frac{\mu_1 q_2}{\mu_2 k_1}) \tag{7}$$

where m = 0, 1, 2, 3, … ,

$$q_2 = k_2 \tan\left[\arctan(\frac{\mu_2 q_3}{\mu_3 k_2}) - k_2 h_2\right]$$

Case 2 $k_0 n_2 < \beta < k_0 |n_1|$

Under this condition, mode fields are oscillating in medium 1 while decay in the other media. We define these modes as the second guided modes and note them TE_m^{II}. Let $\kappa_2 = i\sqrt{\beta^2 - n_2{}^2 k_0{}^2} = i\alpha_2$, the transfer matrix M_2 is rewritten as:

$$M_2{}' = \begin{bmatrix} \cosh(\alpha_2 h_2) & -\frac{\mu_2}{\alpha_2}\sinh(\alpha_2 h_2) \\ -\frac{\alpha_2}{\mu_2}\sinh(\alpha_2 h_2) & \cosh(\alpha_2 h_2) \end{bmatrix}$$

Substituting $M_2{}'$ into Equation (6), we obtain a dispersion equation for TE_m^{II} modes

$$k_1 h_1 = m\pi + \arctan(\frac{\mu_1 q_0}{\mu_0 k_1}) + \arctan(\frac{\mu_1 q'_2}{\mu_2 k_1}) \tag{8}$$

where $q_2{}' = \alpha_2 \tanh\left[\operatorname{arctanh}(\frac{\mu_2 p_3}{\mu_3 \alpha_2}) + \alpha_2 h_2\right]$, and m = 0, 1, 2, 3, …

Although the forms of two dispersion Equations (7) and (8) are similar, they have different physical properties. For *TM* modes, their dispersive equations are similar with that of the corresponding *TE* modes. But, their magnetic permeability in the equations is replaced by dielectric permittivity.

Copyright © 2010 SciRes.

2.2 The Total Power Flux (TPF)

Power fluxes inside the slab waveguide are calculated by an integral of Poynting vector. For *TE* guided modes, their power flux (P_i) in each layer can be obtained through a following equation.

$$P_i = \frac{\beta}{\omega}\int \frac{1}{\mu_i}\left|E_{yi}\right|^2 dx \qquad (i = 0,1,2,3) \tag{9}$$

Substituting Equations (2)-(5) into Equation (9), after some algebraic manipulation, we have the power fluxes inside the waveguide as follows:

$$P_0 = \frac{\beta A^2\cos^2\varphi_{10}}{4q_0\mu_0\omega} \tag{10}$$

$$P_1 = \frac{\beta A^2}{4\mu_1\omega}\left[h_1 + \frac{1}{k_1}\sin(k_1h_1)\cos(k_1h_1 - 2\varphi_{10})\right] \tag{11}$$

$$P_2 = \frac{\beta A^2B^2}{4\mu_2\omega}\left[h_2 + \frac{1}{k_2}\sin(k_2h_2)\cos(k_2h_2 - 2\varphi_{23})\right] \tag{12}$$

$$P_3 = \frac{\beta A^2B^2\cos^2\varphi_{23}}{4q_3\mu_3\omega} \tag{13}$$

where P_0, P_1, P_2, P_3 denote power fluxes of the first TE guided modes in media 0, 1, 2 and 3. Similarly, for the second TE guided modes, their power fluxes are obtained by substituting $\kappa_2 = i\sqrt{\beta^2 - n_2{}^2k_0{}^2} = i\alpha_2$ into Equation (4). The exact results can be obtained easily.

The total power flux (TPF) is defined as follows [8]

$$P = \frac{P_0 + P_1 + P_2 + P_3}{|P_0| + |P_1| + |P_2| + |P_3|} \tag{14}$$

We know that power fluxes propagate forward along the conventional media and they are all positive, *i.e.* P_0, P_2 and $P_3 > 0$. However, in the LHM medium, wave vector is opposite with Ponyting vector, thus, the corresponding power flux is negative, namely, $P_1 < 0$. From a mathematical point of view, in terms of Equation (14), there should exist three cases: 1) $P > 0$, it means $P_0 + P_2 + P_3 > |P_1|$ and is a case for the forward wave; 2) $P < 0$, it implies $P_0 + P_2 + P_3 < |P_1|$ and is a case for the backward wave; 3) $P = 0$, it means $P_0 + P_2 + P_3 = |P_1|$ and electromagnetic waves are stopped and all energy is stored in the waveguide.

3. Numerical Results

3.1 The Dispersive Properties of the *TE* Guided Modes

Material dispersion should be considered because it is one of essential properties of LHM [9]. In this paper, we employ an experimental model [8] with dielectric permittivity and magnetic permeability being dependent on frequency as:

$$\varepsilon_1(\omega) = 1 - \frac{\omega_P^2}{\omega^2} \qquad \mu_1(\omega) = 1 - \frac{F\omega^2}{\omega^2 - \omega_0^2}$$

where F = 0.56, $\frac{\omega_0}{2\pi} = 4$ GHz, $\frac{\omega_P}{2\pi} = 10$ GHz. As frequency increases from 4 GHz to 6 GHz, its dielectric permittivity and magnetic permeability become negative simultaneously. For simplicity, we assume that waveguide thickness of media 2 is fixed and equals to 1 cm. For other media, their permittivity is $\varepsilon_0 = 1$, $\varepsilon_3 = 2.25$, $\varepsilon_2 = 3.0$, and permeability $\mu_0 = \mu_2 = \mu_3 = 1.0$, respectively. Using Equations (7) and (8), we plot some dispersive curves (the effective-refractive-index verse frequency) and discuss them as follows.

3.1.1 The TE_0 Guided Modes

As m = 0, two guided modes (TE_0^{I} and TE_0^{II} modes) coexist and their dispersion curves are shown in **Figure 2**. It is a unique property of the waveguides considering left-handed material dispersion. If neglecting material dispersion, we find the absence of the fundamental mode [6]. For TE_0^{I} mode, as h_1 = h_2 = 1 cm, its effective-refractive-index decreases as frequency increases from 4.56 to 4.88 GHz. As h_2 fixed and h_1 modified (from 0.1 cm to 10 cm), the curves coexist in two frequency regions from 4.735 to 4.88 GHz and 4.835 to 4.88 GHz, respectively. Especially, as frequency is between 4.843 to 4.88 GHz, their dispersion curves are almost overlap. For TE_0^{II} mode, as h_1 = h_2 =1 cm, its effective-refractive-index decreases with frequency increasing from 4.14 GHz to 4.735 GHz. The bandwidth is 0.595 GHz. On the contrary, if h_2 is fixed, and h_1 changes, the curves almost overlap with each other. Besides, two types of fundamental modes have a common property, that is, their group velocity v_g ($v_g = \frac{d\omega}{d\beta}$) are both negative. Negative group velocity implies energy propagates backward and reveals the special property in the LHM slab waveguide.

3.1.2 The Higher Order *TE* Guided Modes

1) As m = 1, both TE_1^{I} and TE_1^{II} modes coexist and their dispersion curves are plotted in **Figure 3**, respectively. For TE_1^{I} mode, its effective-refractive-indexes increase as frequency changing from 4.33 GHz to 4.48 GHz. So, it has positive group velocity. TE_1^{II} mode exists as frequency from 4.14 GHz to 4.60 GHz. The bandwidth is 0.46 GHz. As frequency between 4.49 and 4.60 GHz, its effective-refractive-index has two different values

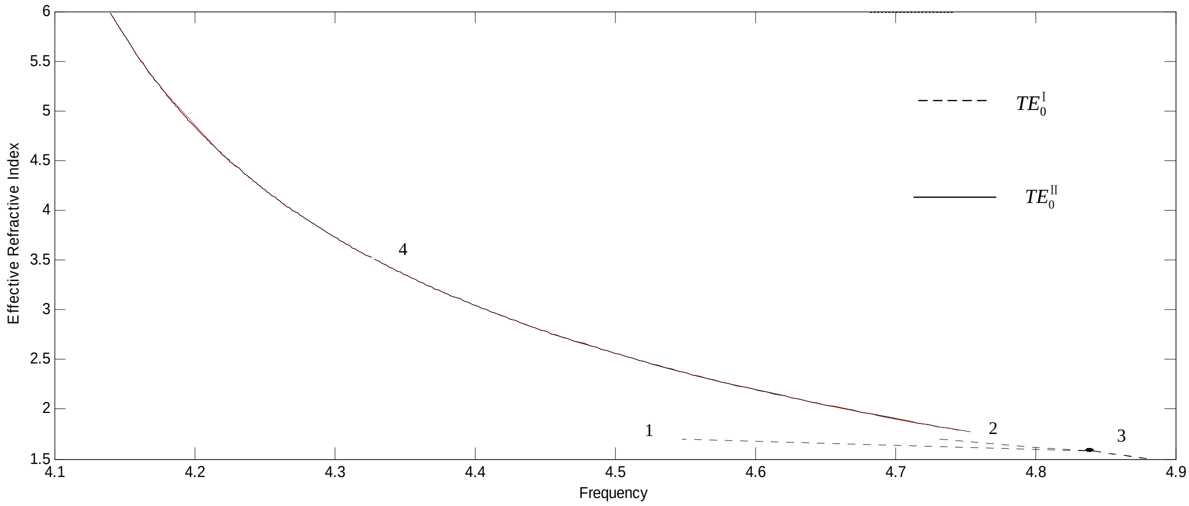

Figure 2. The dispersion curves of the fundamental *TE* guided modes, the effective-refractive-index is a function of frequency. For TE_0^{I} mode, the curves 1, 2, 3 correspond to h_1 = 0.1 cm, 1 cm, 10 cm. For TE_0^{II} mode, only one curve 4 for h_1 = 0.1 cm, 1 cm, 10 cm

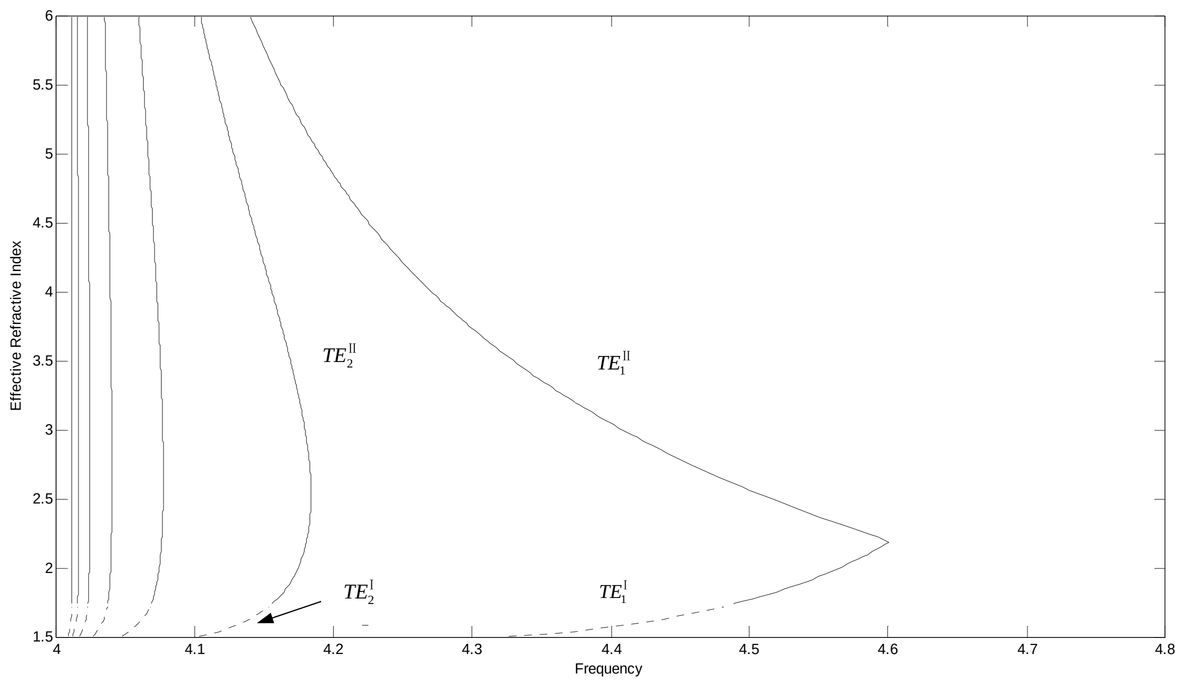

Figure 3. Dispersion curves for higher order *TE* guided modes, the effective-refractive-index is a function with frequency. The curves are arranged along horizontal-axis with *m* = 7, 6, 5, 4, 3, 2, 1, respectively. The dashed curves stand for TE_m^{I} modes, and solid curves correspond to TE_m^{II} modes

corresponding to the same frequency *i.e.* double-mode degeneracy. This is because the dispersion equation has two different solutions at the same frequency. This property can be found in other LHM slab waveguides [4,6]. Besides, its positive and negative group velocities coexist.

2) As *m* increases from 2 to 7, there exist six *TE* guided modes and their dispersion curves are plotted in **Figure 3**. For the same *m*, two types of *TE* guided modes exist and their curves keep continuous. As *m* increases, their curves shift to left and their cutoff frequencies be-

come less. This is different from that of omitting materials dispersion [6]. For the first type TE_m^{I} modes, their group velocities are positive. However, for the second type of TE_m^{II} modes, their double-mode degeneracy appears and their positive and negative group velocities coexist.

3.2 The Total Power Flux (TPF) of *TE* Guided Modes

Employing Equations (10)-(14) and dispersion Equations (7) and (8), we choose the same parameters as Subsection 2.1. The curves of the TPF versus frequency for *TE* guided modes are plotted in **Figures 4 and 5**, respectively. The results are as follows:

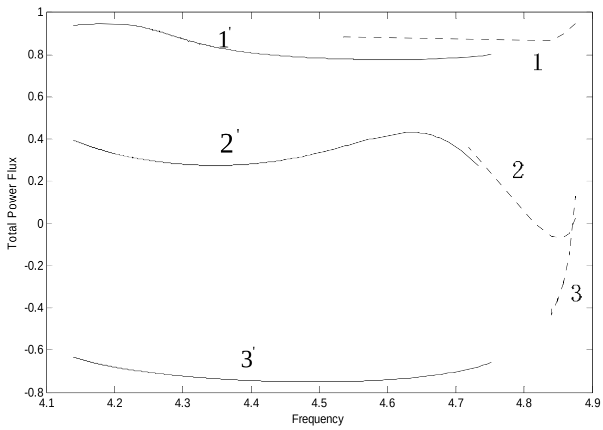

Figure 4. The total power flux of the fundamental *TE* mode for different slab thicknesses. The parameters are the same as Figure 2. The dashed curves stand for TE_0^{I} modes, the solid curves correspond to TE_0^{II} modes

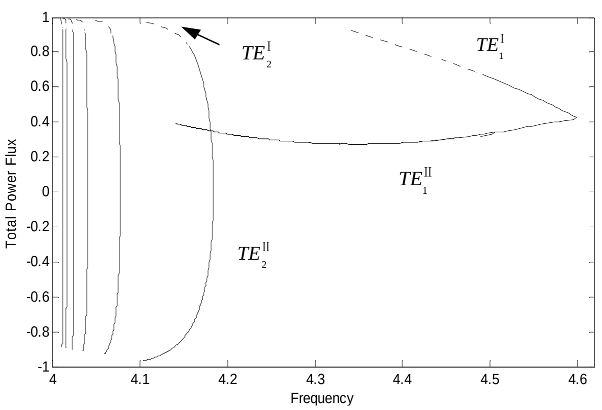

Figure 5. The total power flux of the higher-order *TE* guided modes. The curves are arranged along horizontal-axis with *m* = 7, 6, 5, 4, 3, 2, 1, respectively. The dashed curves stand for TE_m^{I} modes, the solid curves correspond to TE_m^{II} modes

3.2.1 The Properties of the TPF of the TE_0 Guided Modes

For TE_0^{I} and TE_0^{II} modes, their TPF curves are shown in **Figure 4**, respectively. As h_2 (1 cm) is fixed and, (1, 1'), (2, 2') and (3, 3') curves represent h_1 = 0.1 cm, 1 cm and 10 cm, respectively. Clearly, they have a common property that their TPF becomes small with h_1 increased. This is because their power fluxes in the LHM medium increases with h_1, and they are negative. This makes TPF small and even negative with the increase of h_1. For TE_0^{I} mode, as $h_1 < h_2$, its TPF changes with frequency in a smaller range. However, as $h_1 = h_2$ and $h_1 > h_2$, its TPF changes with frequencies in a bigger range. Furthermore, the TPF is positive, negative, and zero at different frequencies. Zero TPF implies that electromagnetic waves are stopped in the waveguide. This property may have some potential applications in the optical waveguide technology. For TE_0^{II} modes, as frequency increases, TPF changes in a small region. For both $h_1 < h_2$ and $h_1 = h_2$, TPF is positive; for $h_1 > h_2$, TPF is negative, and zero TPF doesn't occur.

3.2.2 The Properties of the TPF for Higher Order *TE* Guided Modes

1) As m = 1, for TE_1^{I} and TE_1^{II} modes, their curves of TPF are plotted in **Figure 5**. From these curves, we find that the TPF of the former is bigger than that of the latter and they are both positive. For TE_1^{I} mode, its TPF decreases with the frequency. But, for TE_1^{II} mode, its TPF increases with frequency, then, two different TPF values exist at the same frequency. It results from double-mode degeneracy.

2) For TE_m^{I} and TE_m^{II} modes with m from 2 to 7, their TPF curves are plotted along the anti- horizontal-axis in **Figure 5**. The former is always bigger than the latter. For TE_m^{I} modes, their TPF decreases as frequency increases. But, they are all positive. For TE_m^{II} modes, at the same frequency, positive and negative TPF coexist. It means that two modes propagate along opposite directions. At maximum frequency, zero TPF can be found for each mode.

4. Conclusions

A four-layer slab waveguide with LHM in layer 1 and RHMs in other layers has been studied numerically. The dispersion equations of two types of the *TE* guided modes are obtained and dispersion curves are plotted. Compare these curves, we find some dispersion properties of *TE* modes, such as: two types of the fundamental modes exist, moreover, in some frequency regions, they are insensitive to the waveguide thickness. Besides, the total power flux for *TE* guided modes is calculated and its corresponding curves are plotted. Through these curves, we find some new properties, such as: positive and negative total power fluxes coexist. At maximum frequency, we find zero total power flux. This property may find some potential applications in the optical waveguide technology.

5. Acknowledgments

This work is supported by key project of the National Science Foundation of China (60937003) and STCSM (08DZ2231100).

REFERENCES

[1] D. R. Smith, W. J. Padilla, D. C. Vier, *et al.*, "Composite Medium with Simultaneously Negative permeability and Permittivity," *Physical Review Letters*, Vol. 84, No. 18, 2000, pp. 4184-4187.

[2] A. Berrier, M. Mulot, M. Swillo, *et al.*, "Negative Refraction at Infrared Wavelengths in a Two-Dimensional Photonic Crystal," *Physical Review Letters*, Vol. 93, No. 7, August 2004.

[3] C. M. Soukoulis, S. Linden and M. Wegener, "Negative Refractive Index at Optical Wavelengths," *Science*, Vol. **315,** No. 5808, January 2007, pp. 47-49.

[4] I. V. Shadrivov, A. A. Sukhorukov and Y. S. Kivshar, "Guided Modes in Negative Refractive Index Waveguides," *Physical Review E*, Vol. 67, June 2003.

[5] B. I. Wu, T. M. Grzegorczyk, Y. Zhang and J. A. Kong, "Guided modes with Imaginary Transverse Wave Number in a Slab Waveguide with Negative Permittivity and Permeability," *Journal of Applied Physics*, Vol. 93, No. 11, June 2003, pp. 9386-9388

[6] Z. H. Wang, Z. Y. Xiao and W. Y. Luo, "Surface Modes in Left-Handed Material Slab Waveguides," *Journal of Optics A*: *Pure and Appli Optics*, Vol. 11, No. 1, 2009, pp. 1-5

[7] Z. Y. Xiao and Z. H. Wang, "Dispersion Characteristics of Asymmetric Double-Negative Material Slab Waveguides," *Journal of Optical Society of America B*, Vol. 23, No. 9, 2006, pp. 1757-1760.

[8] Y. He, Z. Cao and Q. Shen, "Guided Optical Modes in Asymmetric Left-Handed Waveguides," *Optics Communications*, Vol. 245, No. 1, 2005, pp. 125-135.

[9] V. G. Veselago, "Electrodynamics of Substances with Simultaneously Negative Electrical and Magnetic Properties," *Soviet Physics Uspekhi*, Vol. 10, No. 4, 1968, pp. 509-517.

[10] Y. He, J. Zhang and C. F. Li, "Guided Modes in a Symmetric Five-Layer Left-Handed Waveguide," *Journal of Optical Society of America B*, Vol. 25, No. 2, 2008, pp. 2081-2091.

[11] L. F. Shen and Z. H. Wang, S. P. Li, "Propagation Properties for Five-Layer Symmetric Slab Waveguides Including Left-Handed Materials," *Optoelectronics Letters*, Vol. 4, No. 3, May 2008, pp. 165-167.

[12] L. F. Shen and Z. H. Wang, "Coupling Characteristics between Five-Layer Slab Wave-Guides Including Left-Handed Materials," *Optoelectronics Letters*, Vol. 4, No. 6, November 2008, pp. 419-421.

[13] J. Zhang, Y. He, C. F. Li and F. M. Zhang, "Guided Modes in a Four-layer Slab Waveguide with the LHM Core," *Acta Optica Sinica*, Vol. 29, No. 10, 2009, pp. 2673-2680.

Copyright © 2010 SciRes.

J. Electromagnetic Analysis & Applications, **2010, 2: 270-275**
doi:10.4236/jemaa.2010.24034 Published Online April 2010 (http://www.SciRP.org/journal/jemaa)

Computation and Analysis of Propellant and Levitation Forces of a Maglev System Using FEM Coupled to External Circuit Model

Shiyou Yang, Lin Yang, Qiang Zhou

College of Electrical Engineering, Zhejiang University, Hangzhou, China.
Email: shiyouyang@yahoo.com

Received December 31st, 2009; revised February 12th, 2010; accepted February 15th, 2010.

ABSTRACT

This paper studies the propellant and levitation forces of a prototype maglev system where the propellant forces are provided by a linear motor system. For this purpose, the mathematical model and method using finite element method coupled to external circuit model is developed. The details of the propellant and levitation forces for a prototype maglev system under different operating conditions are investigated, and some directions are given for practical engineering applications.

Keywords**:** *Maglev System, Propellant Force, Levitation Force, Numerical Computation, Finite Element Method*

1. Introduction

Due to the exclusive salient advantage of non-contact surfaces, an ever-increasing effort has been dedicated to the application of the magnetic levitation technology in engineering disciplines such as maglev trains [1], maglev carriers [2], maglev bearings [3], maglev vibration isolators [4], and so on. One of the key problems in the use of maglev technologies is the accurate and efficient determination of the propellant and levitation forces. Strictly speaking, the electromagnetic field of a maglev system is a complex three dimensional one involving movement components. To predict precisely the transient electromagnetic phenomena of this kind of problems, the complications such as the saturation of iron materials and the relative movement of the moving components must be taken into account properly. Moreover, in a maglev system, the electromagnetic phenomena are jointly generated by the propellant, the levitation and the guiding systems. Thus, one needs to consider all of these issues in the numerical simulations. In addition, the use of power electronic devices in the front end of the linear synchronous motor makes the situation even more serious since a voltage source must also be modeled. Therefore, one needs to resort to the numerical techniques of electromagnetic field computations.

Generally speaking, to address the aforementioned issues of the electromagnetic problem of a maglev system, it is essential to use three dimensional finite element methods [5]. However, the heavy computational burden for the implementation of 3D finite element method is numerically unaffordable for most application cases. In this point of view, the 2D time stepping finite element method [6] is proposed to couple to external circuit model to study the transient performances of a maglev system with the goal of developing an efficient and accurate numerical tool for the computations of the propellant and levitation forces of a maglev system.

2. Mathematical Models and Methods

2.1 Finite Element Model

The transient electromagnetic fields in the propellant and levitation systems are determined using 2D time-stepping finite element method. To determine the field distribution at each time step in a Maglev system, the 2D transverse section spanning one pole pitch of the linear synchronous motor is studied. As shown in **Figure 1**, the solution domain is comprised of the stator winding, the stator core, of the linear motor; the rotor core, and the winding of the levitation magnet/the rotor. With the displacement current being neglected, the field is governed by

$$\frac{\partial}{\partial x}(\nu\frac{\partial A(x,y,t)}{\partial x})+\frac{\partial}{\partial y}(\nu\frac{\partial A(x,y,t)}{\partial y})=-J+\sigma\frac{dA(x,y,t)}{dt} \quad (1)$$
$$A|_{\overline{ab}}=A|_{\overline{gh}}=A_0=0$$

where, ν is the reluctivity, σ is the conductivity, J is the

Copyright © 2010 SciRes.

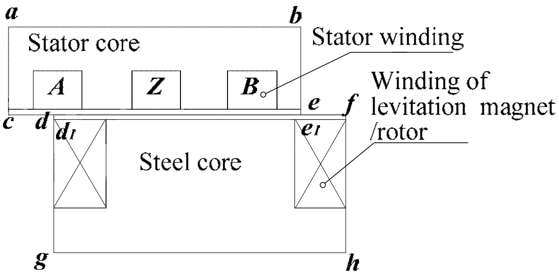

Figure 1. The Schematic diagram of the studied model

source current density, $A(x,y,t)$ is the magnetic vector potential.

For a moving conductor with a velocity v, the induced electric density is

$$\frac{dA}{dt} = \frac{\partial A}{\partial t} - v \times B \tag{2}$$

Using the Galerkin approach to discretize (1), one obtains

$$[S]\{A\} = [C]\{I\} - [T]\frac{d}{dt}\{A\} \tag{3}$$

where,

$$[S] = \sum_{e=1}^{e_0}[\overline{S}]_e = \sum_{e=1}^{e_0} \nu_e \iint_{D_e} ([\frac{\partial N}{\partial x}]_e^T[\frac{\partial N}{\partial x}] + [\frac{\partial N}{\partial y}]_e^T[\frac{\partial N}{\partial y}])dxdy\ ,$$

$$[T] = \sum_{e=1}^{e_0}[\overline{T}]_e = \sum_{e=1}^{e_0} \sigma \iint_{D_e} [N]_e^T[N]dxdy\ ,$$

$$[C] = \sum_{e=1}^{e_0}[\overline{C}]_e = \sum_{e=1}^{e_0} \frac{N_1}{S_b a} \iint_{D_e} [N]_e^T\, dxdy\ .$$

where, a is the number of the parallel branches of the winding, N_1 is the number of total serial turns in one coil, S_b is the slot area, $[N]_e$ is the shape function of the finite element method.

2.2 External Circuit Models

In general, the source current density in (1) is unknown. Thus, the external electric circuit model is coupled to the finite element formulation in this paper to consider the voltage source. Moreover, the end effect of the propellant and levitation systems is also modeled in this circuit formulation. **Figure 2** depicts schematically the equivalent circuit model of the winding of one phase. Mathematically, the external circuit model, including the electromotive force e, the leakage inductance L_e, and resistance R of the windings, is

$$\{u\} = \{e\} - [R]\{I\} - [L]\frac{d}{dt}\{I\} \tag{4}$$

where, $[u] = [-u_f \quad u_a \quad u_b \quad u_c \quad u_d]^T$, $[I] = [i_f \quad i_a \quad i_b \quad i_c \quad i_d]^T$, $[R] = \text{diag}\,[r_f \quad r_a \quad r_b \quad r_c \quad r_d]$, $[L_e] = \text{diag}\,[L_{\sigma f} \quad L_{\sigma a} \quad L_{\sigma b} \quad L_{\sigma c} \quad L_{\sigma d}]$ is the leakage inductance considering the end effect of the machine and levitation magnet, subscript f denotes the winding of the levitation system/the rotor of the linear motor.

To express e in terms of $A(x,y,t)$, one has

$$e = -2pL_{ef}[C]\frac{d}{dt}[A] \tag{5}$$

where L_{ef} is the effective length of the core of the propellant and levitation systems.

2.3 Coupling of Finite Element and External Circuit Models

Integrating (3) and (5) as a whole, one reads

$$\begin{bmatrix} S & -C \\ 0 & R \end{bmatrix}\begin{Bmatrix} A \\ I \end{Bmatrix} = \begin{bmatrix} T & 0 \\ -2PL_{ef} & L \end{bmatrix}\begin{Bmatrix} \frac{dA}{dt} \\ \frac{dI}{dt} \end{Bmatrix} = \begin{Bmatrix} 0 \\ u \end{Bmatrix} \tag{6}$$

2.4 Temporal Discretization

Applying Crank-Nicolson algorithm to (6) with respect to the time variable, one obtains the following equation set of the time-stepping finite element coupled to external circuit model

$$\begin{bmatrix} S^{n+1} + \frac{2T^{n+1}}{\Delta t} & -C \\ \frac{4pL_{ef}C^T}{\Delta t} & R + \frac{2L}{\Delta t} \end{bmatrix}\begin{Bmatrix} A \\ -I \end{Bmatrix}^{n+1} = \begin{bmatrix} -S^n + \frac{2T^n}{\Delta t} & C \\ \frac{4pL_{ef}C^T}{\Delta t} & -R + \frac{2L}{\Delta t} \end{bmatrix}\begin{Bmatrix} A \\ I \end{Bmatrix}^n + \begin{Bmatrix} 0 \\ u \end{Bmatrix} \tag{7}$$

Rearranging (7) into a symmetric form, one has

$$\begin{bmatrix} S^{n+1} + \frac{2T^{n+1}}{h} & C \\ C^T & -\frac{hR}{4pl_{ef}} - \frac{L}{2pl_{ef}} \end{bmatrix}\begin{Bmatrix} A \\ -I \end{Bmatrix}^{n+1} = \begin{bmatrix} -S^n + \frac{2T^n}{h} & C \\ C^T & -\frac{hR}{4pl_{ef}} + \frac{L}{2pl_{ef}} \end{bmatrix}\begin{Bmatrix} A \\ I \end{Bmatrix}^n + \begin{Bmatrix} 0 \\ -\frac{h\overline{U}}{4pl_{ef}} \end{Bmatrix} \tag{8}$$

where, $\overline{U} = u^n + u^{n+1}$, h is the size of the time step.

2.5 Treatment of the Relative Movement of Different Components in a Maglev System

To consider the relative movement of a maglev system, the moving boundary is used [7] in this paper. The moving

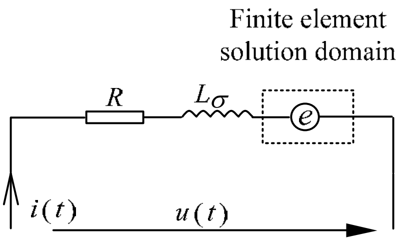

Figure 2. The equivalent circuit of one phase winding

boundaries are the boundaries connecting the stator and rotor meshes of the propellant system, and will vary with the movement. The nodes in the stator side and their counterparts in the rotor side satisfy either periodic or semi-periodic boundary conditions. For example, for a specific relative position of the stator and rotor as depicted in **Figure 1**, the moving boundary conditions are

$$\begin{aligned} A|_{\overline{cd}} &= -A|_{\overline{ef}} \\ A|_{\overline{de}} &= A|_{\overline{d_1e_1}} \end{aligned} \tag{9}$$

2.6 Numerical Computation of the Propellant and Levitation Forces

Once the electromagnetic field is determined in each time step, the corresponding propellant and levitation forces of the maglev system in that time instant can be determined from

$$\begin{aligned} \vec{f} &= \\ &\oint_S \begin{bmatrix} B_xH_x-\frac{1}{2}BH & B_xH_y & B_xH_z \\ B_yH_x & B_yH_y-\frac{1}{2}BH & B_yH_z \\ B_zH_x & B_zH_y & B_zH_z-\frac{1}{2}BH \end{bmatrix} \begin{Bmatrix} n_x \\ n_y \\ n_z \end{Bmatrix} ds \\ &= \oint_S \{[\nu_0(B_x^2-\frac{1}{2}B^2)n_x+\nu_0B_xB_yn_y+\nu_0B_xB_zn_z]\vec{e}_x \\ &+[\nu_0(B_y^2-\frac{1}{2}B^2)n_y+\nu_0B_xB_yn_x+\nu_0B_yB_zn_z]\vec{e}_y \\ &+[\nu_0(B_z^2-\frac{1}{2}B^2)n_z+\nu_0B_xB_zn_x+\nu_0B_yB_zn_y]\vec{e}_z\}ds \end{aligned} \tag{10}$$

In the case study, f_x is the propellant force, and f_z the levitation force.

3. Numerical Results

To predict the transient performances of a maglev system, the computer codes using the proposed models and methods are developed by the authors. The codes are programmed in Fortran language.

3.1 Validation

To validate the proposed mathematical model and method as well as the computer codes, they are firstly used to compute the no-load propellant and levitation forces of a prototype Maglev train in Shanghai commercial Maglev Line. The mesh of total 4784 nodes and 9197 elements as shown in **Figure 3** is used in this case study. The differences between the computed levitation and propellant forces and the exact ones for both forces are less than 5%. Obviously, this case study has positively confirmed the robustness and feasibility of the proposed model and method for solving the electromagnetic fields of a Maglev system problem.

3.2 The Study of Propellant and Levitation Forces of a Prototype Maglev System

After the accuracy and feasibility of the proposed model and method are confirmed, the transient performances of the propellant and levitation forces of a prototype Maglev system under different operating conditions are studied. Firstly, the effect of the torque angle of the linear motor on the propellant and levitation forces is investigated. As shown in **Figure 4**, the torque angle is defined as the angle

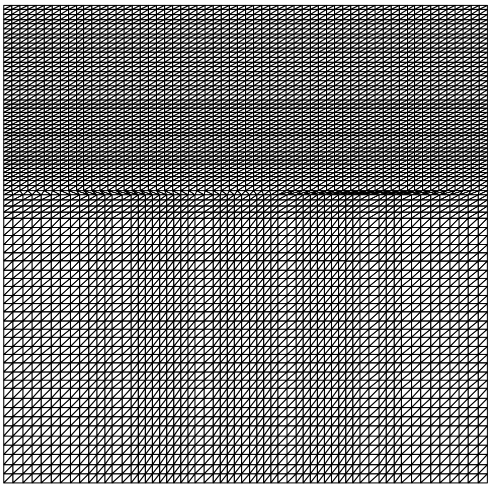

Figure 3. The meshes of one pole pitch region used for validations

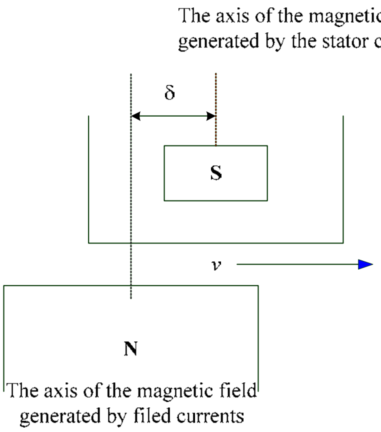

Figure 4. The schematic diagram of the torque angle

in electrical degrees between the axes of the magnetic fields generated by the stator winding (windings *A*, *Z*, *B* in **Figure 1**) and by the rotor winding. The value of this angle will determine the initial relative position of the stator and rotor, *i.e.*, the periodic and semi-periodic boundary conditions of Equation (9). **Figures 5-7** show the computed transient propellant and levitation forces in cases of different torque angles, and **Figure 8** depicts the relationship of the averaged propellant and levitation forces with torque angles. It is should be pointed out that the forces as given in these figures are normalized to their rated values. From these numerical results, it is obviously that

1) The torque angle of the linear motor has a significant effect on both the propellant and levitation forces;

2) The averaged propellant and levitation forces will change periodically with the torque angle.

Therefore, the running state of a Maglev system can be controlled by changing the torque angle of the linear motor.

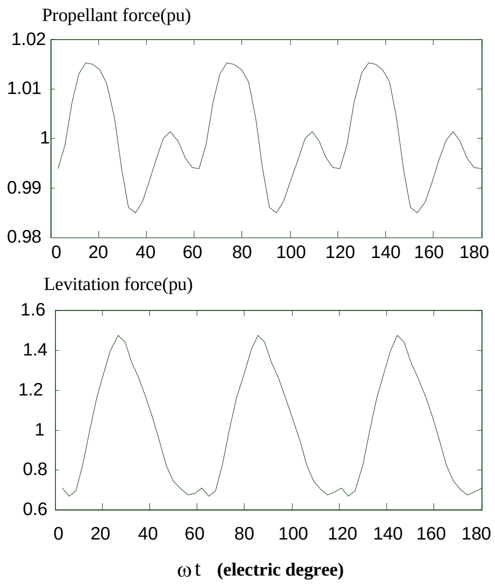

Figure 5. The transient propellant and levitation forces at δ = 0°

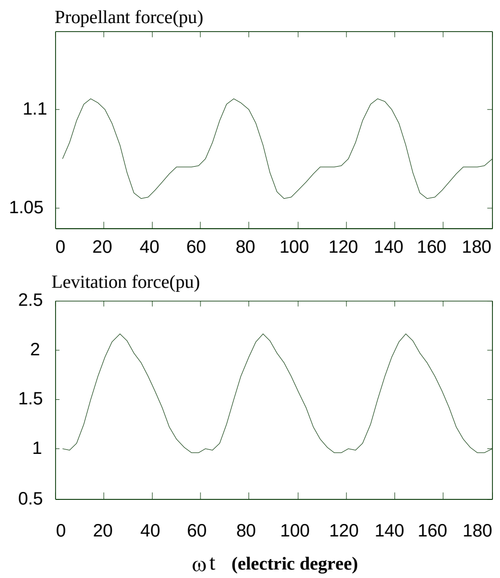

Figure 6 The transient propellant and levitation forces at δ = 20°

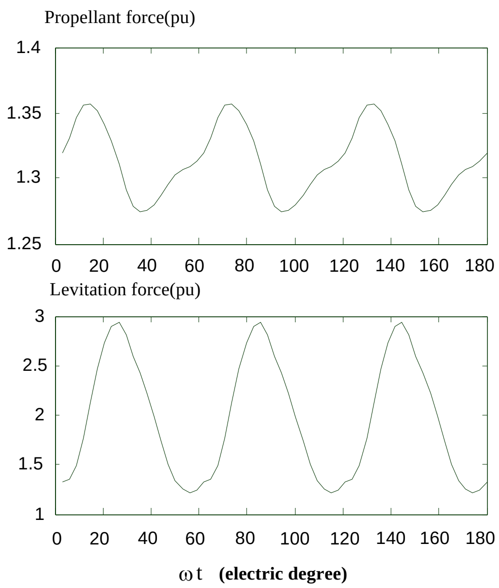

Figure 7. The transient propellant and levitation forces at δ = 60°

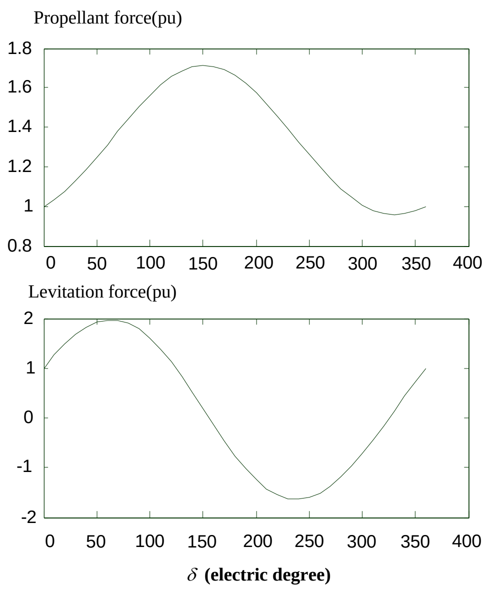

Figure 8. The averaged propellant and levitation forces under different power angle

Copyright © 2010 SciRes.

Since the front end of the linear motor is generally a steady electronic device, typical a PWM source for high precise motion control, the high frequency harmonics are unavoidable in engineering applications of a Maglev system. In this regard, the effects of harmonics on the propellant and levitation forces are then studied using the proposed numerical model and method. In the computer simulation, the harmonic voltages are formulated as

$$V_h = 0.1V_f \cos[5(2\pi f_f t)] \tag{11}$$

where V_f and f_f are, respectively, the amplitude and frequency of the fundamental voltage of the source.

In the numerical implementation, the torque angle of the linear motor is set to different values. **Figures 9** and **10** depict, respectively for torque angle δ = 0° and δ = 10°, the differences of the transient propellant and levitation forces of the prototype maglev system between the normal operating condition and the aggregation of harmonic voltages and currents. From these numerical results, it is clear that:

1) The averaged values of the differences of the transient propellant and levitation forces for one period will approach zero, this means that the harmonics of the sources have almost no effect on the steady state performances of the Maglev system;

2) In view of the transient propellant and levitation forces, the aggregation of harmonic voltages and currents will result in that the forces oscillate around their rated values, resulting in degradation in the transient performances of the Maglev system;

3) Relatively, the effect of a small harmonics on the levitation forces can be neglected compared to that on the propellant forces.

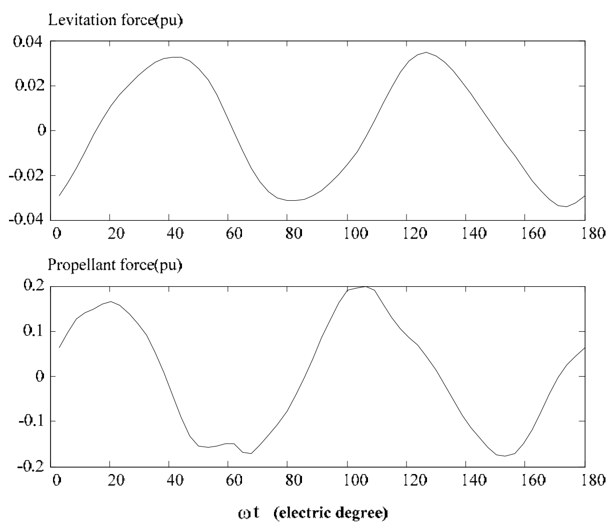

Figure 9. The differences of the transient propellant and levitation forces between the normal operating condition and the aggregation of harmonic voltages and currents at δ = 0°

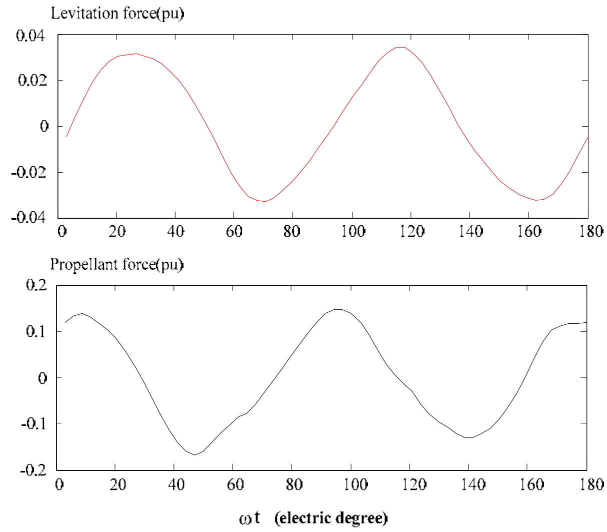

Figure 10. The differences of the transient propellant and levitation forces between the normal operating condition and the aggregation of harmonic voltages and currents at δ=10°

4. Conclusions

A model and method for computing the transient propellant and levitation forces of a Maglev system, with relative error being smaller than 5%, is proposed based on time stepping finite element method coupling to external circuit models. In addition to having the advantages to consider complications such as the relative movement of different components of the linear electrical machines, the saturation of iron materials, the proposed model and method can also take into account the interaction of an external voltage source which is very common with the increasing use of power electronics devices in the front end of general electromagnetic devices. Based on the computer simulation of this case study, for a maglev system, it is concluded that:

1) The torque angle of the linear motor has a significant effect on both the propellant and levitation forces;

2) The averaged propellant and levitation forces will change periodically with the torque angle;

3) The addition of small harmonics in the sources has almost no effect on the steady performances;

4) However, the aggregation of small harmonic voltages and currents in the sources will result in degradation in the transient performances.

5. Acknowledgements

This work is supported by the Science and Technology Department of Zhejiang Province under Grant No. 2008C31021.

Copyright © 2010 SciRes.

REFERENCES

[1] Y. G. Guo, W. Xu, J. G. Zhu, H. Y. Lu and Y. Wang, "Design and Analysis of a Linear Induction Motor for a Prototype HTS Maglev Transportation System," *Proceedings of* 2009 *IEEE International Conference on Applied Superconductivity and Electromagnetic Devices*, Chengdu, 25-27 September 2009, pp. 81-84.

[2] M. Morishita, T. Azukizawa, S. Kanda, N. Tamura and T. Yokoyama, "A New MAGLEV System for Magnetically Levitated Carrier System," *IEEE Transactions on Vehicular Technology*, Vol. 38, No. 4, November 1989, pp. 230-236.

[3] Y.-M. Choi, M. G. Lee, D.-G. Gweon and J. Jeong, "A New Magnetic Bearing Using Halbach Magnet Arrays for a Magnetic Levitation Stage," *Review of Scientific Instruments*, Vol. 80, No. 4, April 2009.

[4] K. Watanabe, S. Hara, Y. Kanemiteu, T. Haga, K. Yano, T. Mizuno and R. Katamura, "Combination of H^{∞} and PI Control for an Electromagnetically Levitated Vibration Isolation System," *Proceedings of the* 35th *Conference on Decision and Control*, Kobe, 11-13 December 1996, pp. 1223-1228.

[5] M. Rizzo, A. Savini and J. Turowski, "3-D Finite Element Analysis of a Linear Reluctance Motor by Using Difference Scalar Potential, *IEEE Transactions on Magnetics*, Vol. 32, No. 3, May 1996, pp. 1533-1536.

[6] L. Y. Xu and W. N. Fu, "Evaluation of Third Harmonic Component Effects in Five-Phase Synchronous Reluctance Motor Drive Using Time Stepping Finite Element Method," *Proceedings of Industry Applications Conference*, Rome, Vol. 1, 8-12 October 2000, pp. 531-538.

[7] R. Y. Tang, Y. Hu, Z. H. Lu, S. Y. Yang and L. J. Maio, "Computation of Transient Electromagnetic Torque in a Turbogenerator under the Cases of Different Sudden Short Circuits," *IEEE Transactions on Magnctics*, Vol. 26, No. 2, March 1990, pp. 1042-1045.

Copyright © 2010 SciRes.

J. Electromagnetic Analysis & Applications, **2010, 2: 276-281**
doi:10.4236/jemaa.2010.24035 Published Online April 2010 (http://www.SciRP.org/journal/jemaa)

Investigation of Electric Fields Inside & Outside a Magnetized Cold Plasma Sphere

Yingle Li[1], Jin Li[2], Mingjun Wang[1], Qunfeng Dong[1]

[1]Institute of Radio Wave Propagation & Scattering, Xianyang Normal University, Xian Yang, China; [2]School of Science, Xidian University, Xian, China.
Email: liyinglexidian@yahoo.com.cn

Received January 8th, 2010; revised February 17th, 2010; accepted February 20th, 2010.

ABSTRACT

The analytical expressions of electric fields inside and outside a magnetized cold plasma sphere are presented by reforming the spherical electromagnetic parameter based on the scales transformation of electromagnetic theory. The obtained results are in good agreement with that in literatures. The angle between the direction of inside field and that of outside field is derived. In S wave band, numerical calculations of effects induced on the inner field by parameters are established. Simulations show that the angle between incident field and the outside magnetic field influences the inner field remarkably. The inner field will decrease as the electron density increasing, however, this density has a great affect on the inner field's direction. The magnitude of the inner field is proportional to the incident wave's frequency.

Keywords: *Magnetized Cold Plasma, Scales Transformation, Electric Field*

1. Introduction

The investigations both for electromagnetic (EM) scattering features and their applications of spherical target have been of a great interest. The electric fields inside and outside a single isotropic dielectric sphere have been researched [1-4]. The scattering features of an isotropic dielectric sphere and a conducting sphere, which are irradiated by an EM wave propagating in the z-direction and polarizing in the x-direction, have been studied [5,6]. By using method of rotating coordinate system, the scattering properties of spherical targets that are irradiated by a wave from an arbitrary direction is studied [6]. In [7-10], the EM scattering features for an isotropic dielectric ellipsoidal target and the power to seize radiation for a coated sphere in the Gaussian beam were separately investigated by the well-known Mie theory. In a word, the subjects of electromagnetic scattering and their applications of an isotropic dielectric sphere have been discussed in detail. However the scattering features for the magnetized cold plasma have not been fully understood in theory. There may be two main reasons for this, the first is the lack of analytical expression of electric field inside the magnetized cold plasma being irradiated by a wave from an arbitrary direction, the second is that some wave equations and functions derived in the isotropic space are now invalid in the anisotropic space. Many particles are practically anisotropic and much smaller than the wave length in size, such as raindrops, sand-dust storm particulates, fog droplets, etc. Therefore the problems relative to electromagnetic field may be approximately considered as an electrostatic one [3]. If the inside electric field is known, the absorption cross section and the scattering cross section of the anisotropic sphere will be obtained accurately [11], so knowing the inside field existing the target is of great importance. In the present paper, the expression of the electric field inside a magnetized cold plasma spherical target is presented first based on the scale transformation theory of the electromagnetic field by reforming the anisotropic electromagnetic parameters into an isotropic one. Then the angle between the field inside the magnetized plasma sphere and that outside the sphere is calculated. Finally the influences induced by the fundamental parameters such as electric density, outside magnetic filed and the azimuth angle on the inner field are simulated. The method used has the features of briefness in computation and distinctness in physical significance.

2. Electric Fields inside and outside a Magnetized Cold Plasma Sphere

2.1 Foundation of Potential Differential Equation

Assume a magnetized cold plasma sphere to have radius

Copyright © 2010 SciRes.

R_0 and its centre to be located at the origin of the primary coordinate system Σ. The outside magnetic field B_0 is in z-axis. The dielectric constant tensor of this plasma is given as

$$\boldsymbol{\varepsilon} = \varepsilon_0 \begin{bmatrix} \varepsilon & -j\varepsilon_p & 0 \\ j\varepsilon_p & \varepsilon & 0 \\ 0 & 0 & \varepsilon_1 \end{bmatrix} \tag{1}$$

where

$$\varepsilon_p = \frac{\dfrac{ne^3 B_0}{m^2\omega^3\varepsilon_0}}{1-\dfrac{e^2B_0^2}{m^2\omega^2}}, \quad \varepsilon_1 = 1-\frac{ne^2}{m\omega^2\varepsilon_0}, \quad \varepsilon = \frac{\dfrac{ne^2}{m\omega^2\varepsilon_0}}{1-\dfrac{e^2B_0^2}{m^2\omega^2}}$$

n is electron density and ω the frequency of incident wave. When the frequency is low, Raleigh criterion $\lambda >> R_0$ is valid, it is so approximately think that the magnetized cold plasma sphere locates in the electrostatic field [1,3]. The plasma has not electric charge in whole. According to $\nabla\cdot\mathbf{D}=0$, $\mathbf{E}=-\nabla u$ and considering that the differential of potential u is not relative to the differential order for x and y, the potential differential equation is obtained in the primary coordinate system as

$$\varepsilon\frac{\partial^2 u}{\partial x^2}+\varepsilon\frac{\partial^2 u}{\partial y^2}+\varepsilon_1\frac{\partial^2 u}{\partial z^2}=0 \tag{2}$$

Now, a scale coordinate system Σ' is introduced as a new coordinate system. The coordinates of this system are indicated with x', y' and z'. The relation of coordinates between the two systems is written as

$$x'=\frac{x}{\sqrt{\varepsilon}}, y'=\frac{y}{\sqrt{\varepsilon}}, z'=\frac{z}{\sqrt{\varepsilon_1}}$$

The differential equation of the potential in the scale coordinate system is derived by substituting the above expressions into Equation (2) and using the condition $u = u'$ [12,13] at any spatial point, Equation (2) may be expressed as

$$\frac{\partial^2 u'}{\partial x'^2}+\frac{\partial^2 u'}{\partial y'^2}+\frac{\partial^2 u'}{\partial z'^2}=0 \tag{3}$$

The condition $u = u'$ is understandable, for the potential is defined as the work done by the electric field to move a unit charge from one point to the reference point, namely W/q, so both the numerator and the denominator are scale invariants. Equation (3) shows that a magnetized cold plasma sphere in the primary coordinate system is transformed into an isotropic sphere in the scale coordinate system. This manipulation may greatly simplify the electromagnetic scattering problems.

2.2 Expressions of Electric Fields outside and inside a Magnetized Cold Plasma Sphere

The solution of Equation (3) can be obtained by using the method of separation of variables as follows:

$$\begin{aligned} u'(R',\theta',\phi') &= \sum_{m,n} a_{m,n} R'^n P_n^m(\cos\theta')\cos m\phi' \\ &+ \sum_{m,n} c_{m,n} R'^n P_n^m(\cos\theta')\sin m\phi' \end{aligned} \tag{4}$$

Equation (4) is a general solution in the scale coordinate system. The parameters in the two coordinate systems are related, their relationships [12,13] are

$$R' = Rq, \qquad q=\left(\frac{\sin^2\theta}{\varepsilon}++\frac{\cos^2\theta}{\varepsilon_1}\right)^{1/2}$$

$$\sin\theta' = \frac{\sin\theta g}{q}, g = 1/\sqrt{\varepsilon}, \cos\theta' = \frac{\cos\theta/\sqrt{\varepsilon_1}}{q}$$

$$\sin\phi' = \sin\phi, \cos\phi' = \cos\phi, u(R,\theta,\phi) = u'(R',\theta',\phi')$$

In Equation (4), the term that may produce a finite potential in the sphere centre is considered. It is concluded that the expression of potential in the primary coordinate system can be obtained only by substituting the relations above into Equation (4). By utilizing the relation between ***D*** and ***E*** and the relation between the vectors in right angle system and spherical system, we may also obtain the expression of the dielectric constant tensor in spherical coordinate system as

$$\boldsymbol{\varepsilon} = \varepsilon_0 \begin{bmatrix} \varepsilon_{11} & \varepsilon_{12} & \varepsilon_{13} \\ \varepsilon_{21} & \varepsilon_{22} & \varepsilon_{23} \\ \varepsilon_{31} & \varepsilon_{32} & \varepsilon_{33} \end{bmatrix} \tag{5}$$

where

$$\begin{aligned} &\varepsilon_{11} = \varepsilon + (\varepsilon_1-\varepsilon)cos^2\theta \\ &\varepsilon_{12} = -(\varepsilon_1-\varepsilon)cos\theta\, sin\theta \\ &\varepsilon_{13} = -j\varepsilon_p\, sin\theta \\ &\varepsilon_{22} = \varepsilon_1 - (\varepsilon_1-\varepsilon)cos^2\theta \\ &\varepsilon_{23} = -j\varepsilon_p\, cos\theta, \varepsilon_{33} = \varepsilon \\ &\varepsilon_{12} = \varepsilon_{21}, \varepsilon_{13} = -\varepsilon_{31}, \varepsilon_{32} = -\varepsilon_{23} \end{aligned}$$

We suppose that E_0 is the magnitude of incident electric field, and that θ_0 and φ_0 are its directional parameters in the primary coordinate system. As shown in **Figure 1**, since the outside electric potential is not symmetrical, we can write the potential as [2]

$$\begin{aligned} u_1(R,\theta,\varphi) &= \sum_{m,n}\left(e_{m,n}R^n + \frac{f_{m,n}}{R^{n+1}}\right)P_n^m(\cos\theta)\cos m\varphi \\ &+ \sum_{m,n}\left(g_{m,n}R^n + \frac{h_{m,n}}{R^{n+1}}\right)P_n^m(\cos\theta)\sin m\varphi \end{aligned} \tag{6}$$

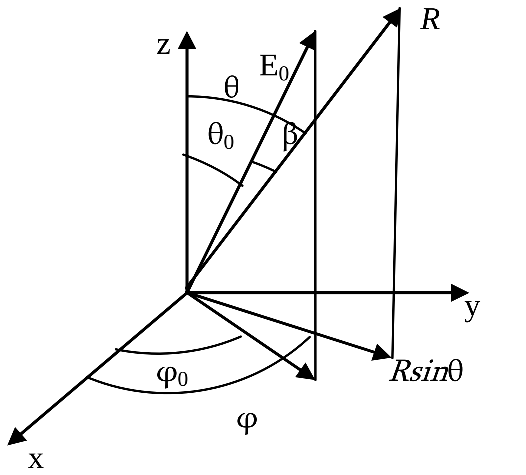

Figure 1. Relation between the observing point and the outside electric field E_0

When $R \to \infty$, the electric potential near to

$$u_1 \to -RE_0 \cos\beta$$
$$\cos\beta = -RE_0\left[\sin\theta\sin\theta_0\cos(\varphi-\varphi_0)+\cos\theta\cos\theta_0\right]$$

Comparing the coefficients of the above expression with those in Equation (6) yields

$$u_1(R,\theta,\varphi) = AR\cos\theta + BR\sin\theta\cos\varphi + DR\sin\theta\sin\varphi + \sum_{m,n}\frac{f_{m,n}}{R^{n+1}}P_n^m(\cos\theta)\cos m\varphi + \sum_{m,n}\frac{h_{m,n}}{R^{n+1}}P_n^m(\cos\theta)\sin m\varphi$$

where $A = e_{01} = -E_0\cos\theta_0, B = e_{11} = -E_0\sin\theta_0\cos\varphi_0$

$D = g_{1,1} = -E_0\sin\theta_0\sin\varphi_0$

$e_{m,n} = 0 \quad m \neq 0,1 \quad n \neq 1, \qquad g_{m,n} = 0$

$m \neq 1 \quad n \neq 1$

Equations (4) and (6) are the electric potentials inside and outside the magnetized cold plasma sphere respectively. On the surface of the sphere, the electric potential inside the sphere is equal to that outside the sphere and the electric displacement $\boldsymbol{D}_0$ is continuous in the normal direction, namely

$$u\big|_{R=R_0} = u_1\big|_{R=R_0}$$

$$\varepsilon_0\left(\varepsilon_{11}\frac{\partial u}{\partial R}+\varepsilon_{12}\frac{1}{R}\frac{\partial u}{\partial\theta}+\varepsilon_{13}\frac{1}{R\sin\theta}\frac{\partial u}{\partial\phi}\right)\Bigg|_{R=R_0} = \varepsilon_0\frac{\partial u_1}{\partial R}\Bigg|_{R=R_0} \qquad (7)$$

Inserting Equations (4)-(6) into the above conditions yields

$$\left.\begin{aligned} a_{m,n} &= 0 \\ c_{m,n} &= 0 \\ f_{m,n} &= 0 \\ h_{m,n} &= 0 \end{aligned}\right\} \quad \sqrt{n} \geq 2,\ m = 0,1,\ldots,n$$

There are three types of trigonometric functions in the above expressions, namely

$$\cos\theta \qquad \sin\theta\cos\varphi \qquad \sin\theta\sin\varphi$$

Comparing their coefficients, we may obtain the following matrix equation

$$\mathbf{PX} = \mathbf{Y} \qquad (8)$$

where

$$\mathrm{P} = \begin{bmatrix} \frac{R_0}{\sqrt{\varepsilon_1}} & -R_0^{-2} & 0 & 0 & 0 & 0 \\ \sqrt{\varepsilon_1} & 2R_0^{-3} & 0 & 0 & 0 & 0 \\ 0 & 0 & \sqrt{\varepsilon} & -\frac{j\varepsilon_p}{\sqrt{\varepsilon}} & \frac{2}{R_0^3} & 0 \\ 0 & 0 & \frac{j\varepsilon_p}{\sqrt{\varepsilon}} & \sqrt{\varepsilon} & 0 & \frac{2}{R_0^3} \\ 0 & 0 & \frac{R_0}{\sqrt{\varepsilon}} & 0 & -R_0^{-2} & 0 \\ 0 & 0 & 0 & \frac{R_0}{\sqrt{\varepsilon}} & 0 & -R_0^{-2} \end{bmatrix}$$

$$\mathrm{X} = \left[a_{0,1}\ f_{0,1}\ a_{1,1}\ c_{1,1}\ f_{1,1}\ h_{1,1}\right]^T$$

$$\mathrm{Y} = \left[AR_0\ A\ B\ D\ BR_0\ DR_0\right]^T$$

The solution of Equation (8) is easy derived as

$$\mathbf{X} = \mathbf{P}^{-1}\mathbf{Y} \qquad (9)$$

Namely

$$\begin{bmatrix} a_{0,1} \\ f_{0,1} \\ a_{1,1} \\ c_{1,1} \\ f_{1,1} \\ h_{1,1} \end{bmatrix} = \begin{bmatrix} \frac{3A\sqrt{\varepsilon_1}}{2+\varepsilon_1} \\ \frac{AR_0^3(1-\varepsilon_1)}{2+\varepsilon_1} \\ \frac{3\sqrt{\varepsilon}\left(2B+B\varepsilon+jD\varepsilon_p\right)}{\varepsilon^2+4\varepsilon-\varepsilon_p^2+4} \\ \frac{3\sqrt{\varepsilon}\left(2D+D\varepsilon-jB\varepsilon_p\right)}{\varepsilon^2+4\varepsilon-\varepsilon_p^2+4} \\ -\frac{R_0^3\left(B\varepsilon^2+B\varepsilon-2B-B\varepsilon_p^2-3jD\varepsilon_p\right)}{\varepsilon^2+4\varepsilon-\varepsilon_p^2+4} \\ -\frac{R_0^3\left(D\varepsilon^2+D\varepsilon-2D-D\varepsilon_p^2+3jB\varepsilon_p\right)}{\varepsilon^2+4\varepsilon-\varepsilon_p^2+4} \end{bmatrix}$$

Copyright © 2010 SciRes.

We thus obtain the solution of electric potential inside and outside a magnetized cold plasma sphere as

$$u(R,\theta,\varphi)=\frac{3A}{2+\varepsilon_1}Rcos\theta+\frac{3\left(2B+B\varepsilon+jD\varepsilon_p\right)}{\varepsilon^2+4\varepsilon-\varepsilon_p^2+4}Rcos\varphi sin\theta+\frac{3\left(2D+D\varepsilon-jB\varepsilon_p\right)}{\varepsilon^2+4\varepsilon-\varepsilon_p^2+4}Rsin\varphi sin\theta \tag{10}$$

$$\begin{aligned}u_1(R,\theta,\varphi)&=ARcos\theta+BRsin\theta cos\varphi+DRsin\theta sin\varphi\\&+\frac{AR_0^3}{R^2}\frac{1-\varepsilon_1}{2+\varepsilon_1}cos\theta\\&-\frac{R_0^3\left(B\varepsilon^2+B\varepsilon-2B-B\varepsilon_p^2-3jD\varepsilon_p\right)}{\varepsilon^2+4\varepsilon-\varepsilon_p^2+4}sin\theta cos\varphi\\&-\frac{R_0^3\left(D\varepsilon^2+D\varepsilon-2D-D\varepsilon_p^2+3jB\varepsilon_p\right)}{\varepsilon^2+4\varepsilon-\varepsilon_p^2+4}sin\theta sin\varphi\end{aligned} \tag{11}$$

2.3 Discussions

From Equation (6) it follows that when $\theta_0 = \varphi_0 = 0$, the incident electric field $\boldsymbol{E}_0$ is in the z-direction, $B = D = 0$, and $A = -E_0$. If we suppose that $\varepsilon_1=\varepsilon_2=\varepsilon_3=\frac{\varepsilon}{\varepsilon_0},\varepsilon_p=0$, now the problem of the electric field in a magnetized cold plasma medium has been changed into a question in the isotropic medium. Equations (10) and (11) are transformed, respectively, into the following expressions:

$$u(R,\theta,\varphi)=\frac{-3E_0\varepsilon_0}{2\varepsilon_0+\varepsilon}R\cos\theta$$

$$u_1(R,\theta,\varphi)=-E_0R\cos\theta+\frac{-E_0R_0^3}{R^2}\frac{\varepsilon_0-\varepsilon}{2\varepsilon_0+\varepsilon}\cos\theta$$

From [3,4,14], we obtain the solutions of an isotropic dielectric sphere in electric field E_0. These solutions may be given as

$$V(R,\theta,\varphi)=\frac{-3E_0\varepsilon_0}{2\varepsilon_0+\varepsilon}R\cos\theta$$

$$V_1(R,\theta,\varphi)=-E_0Rcos\theta+\frac{-E_0R_0^3}{R^2}\frac{\varepsilon_0-\varepsilon}{2\varepsilon_0+\varepsilon}cos\theta$$

It can be seen that the results are consistent entirely with those in the literature. The correctness of the obtained results is therefore tested. Let α and β be the angles between E_0 and the x-axis and between E_0 and the y-axis, respectively, then it will be easily proved that $\cos\alpha=\sin\theta\cos\varphi,\cos\beta=\sin\theta\sin\varphi$. So the second term and the third term in Equation (10) are the potential produced by the polarizing electrical dipole moment respectively in x-direction and in y-direction. In the scattering of small particles, for example, Raleigh scattering, the electric field inside the target is of great importance. So we must discuss the distribution of the inside electric field in detail. The electric field is obtained by making a gradient from Equation (10) and utilizing the transformation between a vector respectively in the spherical coordinate system and the right angle coordinate system as follows:

$$\mathbf{E}=-\frac{3\left(2D+D\varepsilon-jB\varepsilon_p\right)}{\varepsilon^2+4\varepsilon-\varepsilon_p^2+4}\hat{y}-\frac{3\left(2B+B\varepsilon+jD\varepsilon_p\right)}{\varepsilon^2+4\varepsilon-\varepsilon_p^2+4}\hat{x}-\frac{3A}{2+\varepsilon_1}\hat{z} \tag{12}$$

Equation (12) demonstrates that the electric field inside a magnetized cold plasma sphere is a uniform field which is a complex function of the incident azimuth angle, outside magnetic field, the electric density and the frequency etc. This field makes an angle δ with respect to the incident field E_0. This cosine function for this angle is easily derived by taking the scalar product of vectors as follows:

$$\cos\delta=\frac{\frac{3D\left(2D+D\varepsilon-jB\varepsilon_p\right)}{\varepsilon^2+4\varepsilon-\varepsilon_p^2+4}+\frac{3B\left(2B+B\varepsilon+jD\varepsilon_p\right)}{\varepsilon^2+4\varepsilon-\varepsilon_p^2+4}+\frac{3A^2}{2+\varepsilon_1}}{\left[\left(\frac{3\left(2D+D\varepsilon-jB\varepsilon_p\right)}{\varepsilon^2+4\varepsilon-\varepsilon_p^2+4}\right)^2+\left(\frac{3\left(2B+B\varepsilon+jD\varepsilon_p\right)}{\varepsilon^2+4\varepsilon-\varepsilon_p^2+4}\right)^2+\left(\frac{3A}{2+\varepsilon_1}\right)^2\right]^{\frac{1}{2}}} \tag{13}$$

where $A=-E_0\cos\theta_0, B=-E_0\sin\theta_0\cos\phi_0, D=-E_0\sin\theta_0\sin\phi_0$

It is a function of the azimuth angle. The displacement D is easy obtained from Equations (1) and (12), it is not presented here in detail. Followings are partial numerical results:

According to the literature [15], the parameters used in simulations are f = 3 GHz, n = 4.5 × 10^{17} m^{-3}. It is con-

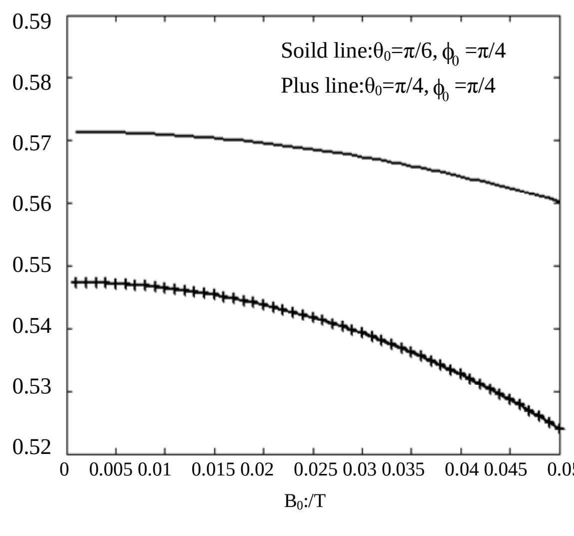

Figure 2. Electric field changes with outside magnetic field

cluded from **Figure 2** that the inner field will decrease when the outside magnetic field increase. The angle θ_0 between the outside electric field and the outside magnetic field has a great effect on the field inside the plasma and further simulations show that angle φ_0 has not affect on the inner field. This is because that the anisotropic property in plasma is caused by the outside magnetized field, the components of outside electric field are relative to the angle θ_0 and angle φ_0 has a good symmetry to outside magnetic field, so the inner field does not varying with angle φ_0. In **Figure 3**, the azimuth angles are $\pi/4$, $\pi/3$. It is demonstrated that the inner electric field decrease as the electron density increasing. This is caused by the reason that when the electron density increases, the electrical conductivity is also strong, so the shield of electric field is enhanced. It is also can be seen from **Figure 4** that the inner field is proportional to the operating frequency. This is due to the reason that the variety of electric charges inside plasma not agreement with that of outside electric field and the shielding effect is thus debased. **Figure 5** had conducted the change of angle δ versus the frequency. The solid line and dotted line are nearly superposed in which the density n = 4.5 × 10^{17} m^{-3} and outside magnetic fields B_0 are respectively 0.004T and 0.005T. Another density of n = 8 × 10^{17} m^{-3} is used in the second dotted line. It obviously demonstrates that the outside magnetic field has not a great influence on the angle and however the electron density has a great effect on it. The angle is proportional to the frequency. It is well known that in isotropic medium, the angle δ is zero, so in the time varying electromagnetic field, the electric charges, negative and positive, in the cold plasma can not agreement with outside field as the frequency being augment which causes the angle's accretion.

3. Conclusions

In this paper, the electric fields inside and outside a magnetized cold plasma sphere are investigated. We use the scale transformation theory of the electromagnetic field to reconstruct the Laplace equation and then obtain two analytical expressions of the electric potentials inside and outside the magnetized cold plasma sphere in detail. The obtained results are consistent with those in the literature when the dielectric constant tensor becomes that in an isotropic medium. The angle between the total fields inside and outside the magnetized cold plasma sphere is derived. The effects induced by the incident direction, outside magnetic field, frequency etc. on the direction and the magnitude of the inside electric field are simulated. Due to many particles such as sand-dust storm particulates, atomy particles and raindrops are generally anisotropic, so the results obtained can provide

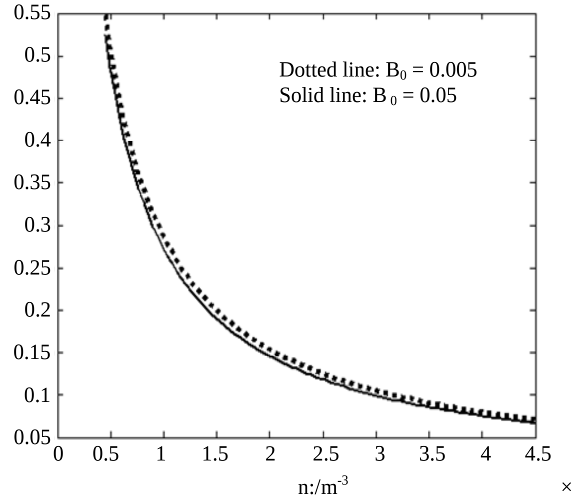

Figure 3. Electric field changes with electron density

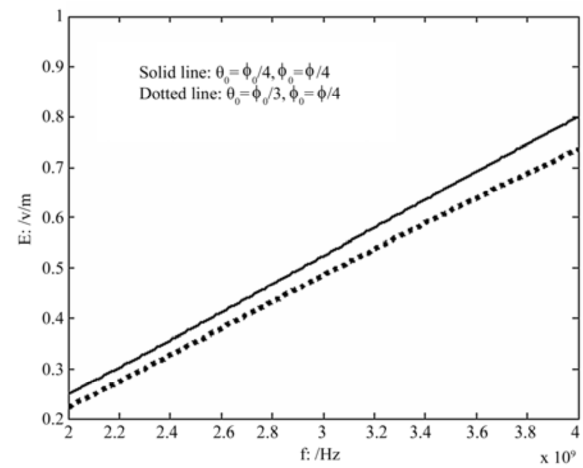

Figure 4. Electric field changes with frequency

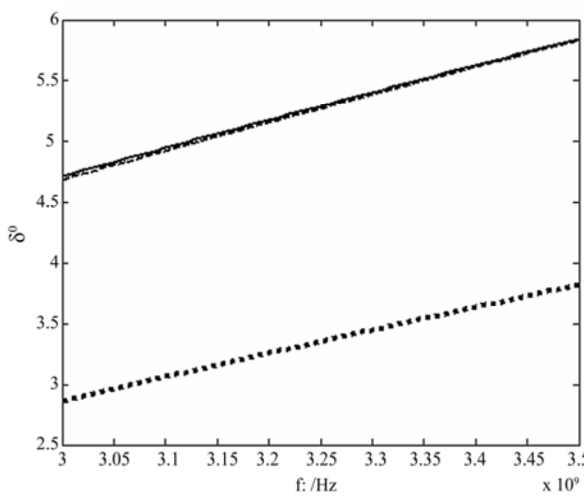

Figure 5. Angle δ changes with frequency

a good theoretical foundation for studying the scattering features of small particles and magnetized cold plasma. How to use the scale transformation theory to study the electromagnetic fields inside and outside a magnetized cold plasma target irradiated by the time-varying electromagnetic wave is our next research subject.

4. Acknowledgments

This project was supported by the National Natural Science Foundation of China (Grant No. 60971079, 60801047), the Natural Science Foundation of Shaanxi Province (Grant No. 2009JM8020) and Natural Science Foundation of Shaanxi Educational Office (Grant No. 09JK800).

REFERENCES

[1] D. K. Cheng "Field and Wave Electromagnetics," Pearson Education Addison-Wesley, Massachusetts, 2006.

[2] J. A. Stratton "Electromagnetic Theory," McGraw-Hill, New York, 1941.

[3] A. Ishimaru, "Wave Propagation and Scattering in Random Medium," Part I, Academic Press, New York, 1978, pp. 27-30.

[4] A. K. Jin, "Electromagnetic Wave Theory," Electronics Industry Press, Beijing, 2003, pp.305-312.

[5] Y. P. Wang and D. Z. Cheng, "Engineer Electrodynamics," Press of Xidian University, Xian, 1985.

[6] Y. L. Li and J. Y. Huang, "The Scattering Fields for a Spherical Target Irradiated by a Plane Electromagnetic Wave in an Arbitrary Direction," *Chinese Physics*, Vol. 15, No. 2, 2006, pp. 281-285.

[7] H. Huang, Y. Fan, B. Wu, F. Kong and J. A. Kong, "Surface Modes at the Interfaces Between Isotropic Media and Uniaxial Plasma," *Progress in Electromagnetics Research*, Vol. 76, 2007, pp. 1-14.

[8] Y. P. Han, Y. G. Du and H. Y. Zhang, "Radiation Trapping Forces Acting on a Two-Layered Spherical Particle in a Gaussian Beam," *Acta Physica Sinica*, Vol. 55, No. 9, 2006, pp. 4557-4560.

[9] L. Bai and Z. S. Wu, "Scattering of Fundamental Gaussian Beam from On-Axis Cluster Spheres," *Acta Physica Sinica*, Vol. 54, No. 5, 2005, pp. 2025-2030.

[10] J. R. Bottiger, Y. L. Fan, B. Stout, J. C. Auger and S. Holler, "Observations and Calculations of Light Scattering from Clusters of Spheres," *Applied Optics*, Vol. 39, No. 36, 2000, pp. 6873-6887.

[11] L. Tsang, J. A. Kong and K. H. Ding, "Scattering of Electromagnetic Waves," John Wiley & Sons, New York, 2000, pp. 9-26.

[12] Y. L. Li and J. Y. Huang, "The Scale-Transformation of Electromagnetic Theory and its Applications," *Chinese Physics*, Vol. 14, No. 4, 2005, pp. 646-656.

[13] Y. L. Li and J. Y. Huang, "Scales Transformation Theory of Electromagnetic Field and its Applications," Press of Xidian University, Xian, 2006.

[14] L. Q. Xu and W. Cao, "Electromagnetic Field and Electromagnetic Theory," Science Press, Beijing, 2006, pp. 88-90.

[15] S. B. Liu, J. J. Mo and N. C. Yuan, "Research on the Absorption of EM-Wave by Inhomogeneous Magnetized Plasmas," *Acta Electronica Sinica*, Vol. 31, No. 3, 2003.

Copyright © 2010 SciRes.

Call for Papers

Journal of Electromagnetic Analysis and Applications (JEMAA)

ISSN: 1942-0730 (Print), 1942-0749 (Online)
www.scirp.org/journal/jemaa

JEMAA is a professional journal in the field of electromagnetic analysis, testing and application. The goal of this journal is to provide an international platform for engineers and academicians all over the world to promote, share, and discuss various new issues and developments in the field of electromagnetic. This journal is edited to encourage deeper understanding and greater effectiveness in theory analysis, testing, numerical calculation and engineering application that relevant electromagnetic fields.

Editors-in-Chief

Prof. James L. Drewniak	Electrical Engineering and Materials Science and Engineering, Missouri-Rolla, USA
Prof. Yuanzhang Sun	School of Electrical Engineering, Wuhan University, China

Subject Coverage

JEMAA publishes four categories of original technical reports: papers, communications, reviews, and discussions. Papers are well-documented final reports of research projects. Communications are shorter and contain noteworthy items of technical interest or ideas required rapid publication. Reviews are synoptic papers on a subject of general interest, with ample literature references, and written for readers with widely varying background. Discussions on published reports, with author rebuttals, form the fourth category of JEMAA publications. Topics of interest include, but are not limited to:

- Electromagnetic Numerical Analysis
- Multiphysics Coupled Problems
- Electromagnetic Inverse Problems
- Electromagnetic Structure Optimization
- Test Electromagnetic Analysis Method
- Workshop Benchmark Problems
- Electromagnetic Devices
- Electromagnetic Compatibility
- Electromagnetic Nondestructive Testing
- Electromagnetic Material Modelling

Notes for Intending Authors

Submitted papers should not be previously published nor be currently under consideration for publication elsewhere. Paper submission will be handled electronically through the website. All papers will be peer reviewed. For more derails about the submissions, please access the website.

Website and E-Mail

http://www.scirp.org/journal/jemaa jemaa@scirp.org

J. Electromagnetic Analysis & Applications, 2010
Published Online April 2010 in SciRes (http://www.SciRP.org/journal/jemaa)

TABLE OF CONTENTS

Volume 2 Number 4 **April 2010**

Copyright©2010 SciRes